A STUDY OF T TAURI STARS WITH MULTIPLE SPECTRAL TYPES AND THEIR SURFACE TEMPERATURES

Matthew James Horrobin

Presented for the Degree of Doctor of Philosophy
The University of Edinburgh
1999

This thesis is dedicated to my parents, for their continuous support.

This thesis is my own composition except where indicated in the text.

February 6, 2000

Acknowledgements

I would first like to thank Mark Casali, my supervisor, for his help throughout the four years of this project. For the unenviable task of proof reading this thesis, and help with bureaucracy, thanks to John Cooke. Thanks also goes to Henry Buckley, Andrew Harrison and Nick Jessop for discussion of many star formation topics. For help with general science thanks to Peter Brand and Andrew Taylor, and for help with science and the consumption of alcohol thanks to Simon Dye, Richard Knox and Ross McClure. I am also indebted to Amy Jones, for keeping me sane during the final months of writing up.

I would also like to mention, in no particular order, the following, for making the IfA such a nice place to study: Elese Archibald, Helen Valentine, James Manners, Louisa Nolan, Ali Higgins, Rob, Kent 'n Pete, Bill Ballinger, Steve Bond and Peter Witchalls.

Contents

List of Figures

List of Tables

Abstract

This thesis describes the results of two spectral studies of T Tauri stars. T Tauri stars are young, low mass, stars which have yet to evolve to the point where Hydrogen fusion occurs in their cores. They are normally found in groups associated with gas clouds in locations called star forming regions. Much work has been done to explain the bizarre spectral features of T Tauri stars, and this has led to the development of a standard model for their structures. Classical T Tauri stars are thought to be surrounded by large discs of accreting material, which slowly adds to the mass of the star. This accretion process results in large U.V. and I.R. fluxes for the stars when compared to their main sequence counterparts. Weak-line T Tauri stars do not display any accretion features and are thought to be more evolved than Classical T Tauri stars. Observations show that both types of T Tauri star have active chromospheres and large cool spots, which are both thought to be a result of strong magnetic fields. This thesis is motivated by two studies, one spectroscopic, one photometric, both of which suggest that some T Tauri stars display photospheric features from regions of different temperatures, or multiple spectral types (MST).

The first spectral study discussed is of near-I.R. data taken with UKIRT. The spectra are of high resolution data from the region around 1.63 μm, and are of T Tauri, giant and dwarf stars of known spectral type. It is shown that a ratio of selected OH to Fe lines gives a good trend with the optically measured T_{eff}, derived from spectral types, for both dwarfs and giants. Whilst some of the T Tauri stars fit this trend, it is found that 4 stars clearly lie above it. This is taken as an indication of cooler regions in the spectra than had previously been detected, an MST effect.

The second spectral study discussed is of optical data taken with the FLAIR system on the UKST. The spectra span the entire optical region observable with this instrument, and are intended to show variation in temperature sensitive features between the blue and red optical regions. Spectra are presented from 2 consecutive nights of observations and previously discovered MST stars are found to show deeper G bands than would be predicted from the TiO bands in the red spectra. It is found that the G band of one object has varied both on a night to night basis and since the previous observations from the mid-1980's. It is also shown that no variation has occurred in the red spectra.

All of the information on MST stars is then compared in order to determine the best physical model for the effect. It is shown that none of the regions in the standard model of Classical T Tauri stars can produce the MTS features. The first model considered that could display MTS features is of binary systems of stars with differing spectral type, but equivalent flux in the optical. It is found that these systems would be too rare to explain all the MTS results. The large cool spots seen on T Tauri stars are also considered as the cause of the MST effect. It is shown that the size of spots required is much greater than the size of observed cool regions. The current theories of solar active regions are discussed, revealing that the dominant photospheric regions are in fact the small, bright faculae. Whilst the spectra of solar faculae are still not fully understood it is found that a faculae+photosphere+cool spot model of T Tauri spectra can produce all the observed MST effects.

Finally, the systematic errors in the H-R diagram introduced by the MST effect are considered. By comparison with research on dwarf stars it is found that the MST effects do not significantly alter the stellar T_{eff} and luminosity. The largest errors are introduced if only a small wavelength region is considered when determining the spectral type of the star. Studies that derive a T_{eff} from an apparent spectral type and ignore the MST effect can both over and underestimate T_{eff}, leading to a possible factor of 2 error in the stellar mass. As T Tauri spectral parameters are also used to derive the overall features of star forming regions, this can lead to the miscalculation of the mass function and ages of these regions.

Chapter 1

Introduction

T Tauri stars are young, low mass stars. Their temperatures are high enough to display typical stellar features (G to M spectral type), but their central conditions are not extreme enough for Hydrogen fusion to occur. They are normally found associated with gas clouds and other young stellar objects (YSOs) in locations called star forming regions. They are the youngest type of YSO in which the surface of the central object can be observed optically, and they are also the final stage of evolution before the main sequence. Observations of these objects provides information for many areas of astronomy, including the universality of the stellar initial mass function, the number of stars in multiple systems and the initial conditions for planet formation.

The observed spectra of T Tauri stars (TTSs) display many unusual features, most of which have been included in the modern model of low mass star formation. This model invokes large discs of infalling material circling the stars, radiating mainly in the infra-red, with the final free-fall accretion process liberating enough potential energy to produce a bright ultra-violet flux. This work concentrates on the spectral features which have no obvious explanation within the current framework, and attempts to discover the physical processes which must be considered to provide a fuller understanding of these objects. (For an overview of low mass star formation and large scale features see Appendix B.)

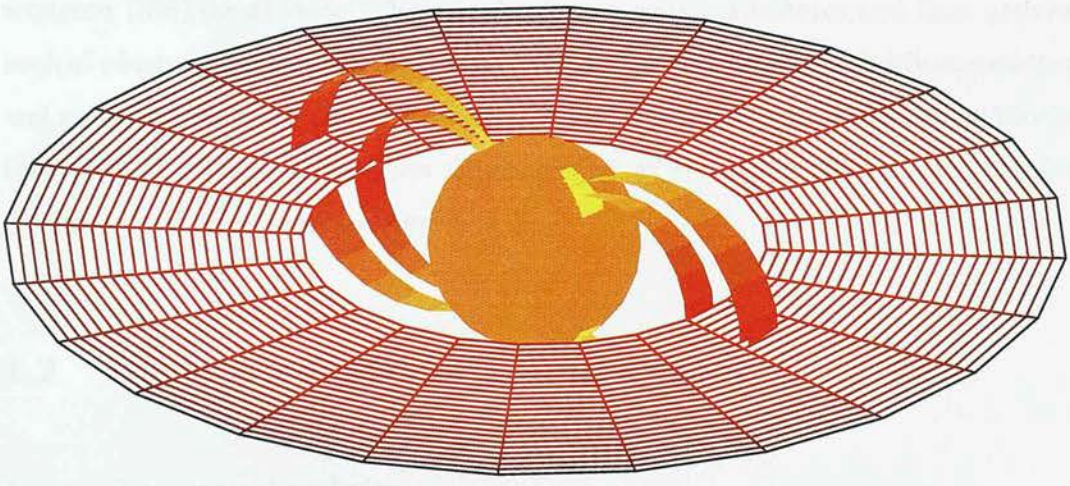

Figure 1.1: A model of a Classical T Tauri star

1.1 General T Tauri features

There are two types of TTS, the Classical (CTTS) and Weak-line (WTTS). Classical T Tauris are the younger of the two and lie at the heart of complex accretion systems. The standard model has them surrounded by a large disc, >100 A.U., which slowly accretes material onto the central star ($<10^7$ $M_\odot$ per year) and is observed by its continuum emission in the infra-red (I.R.). The accreting material is channelled by the star's magnetic field into columns, which allows it to free-fall onto the star. The high velocity impact causes a shock front in the stellar chromosphere, which is observed as a 10,000 K emission region. This region is the origin of both the large hydrogen emission lines (Hα > 5 Å equivalent width), which are used to identify CTTSs, and of an optical and U.V. continuum emission which reduces the depth of all absorption features (veiling). The magnetic field is also seen in large cool spots in the photosphere, and strong flare activity. It is believed that the connection between the star and the disc partly governs the rotation rate of the star, giving a typical rotation period of 8 days (Bodenheimer 1995), although some have periods similar to those of WTTSs (Bouvier et al. 1995). For more discussion and references see Appendix B.

Weak-line T Tauris do not show the strong emission, either in optical or I.R. which

is indicative of accretion. Their photospheres appear to be similar to those of main sequence (MS) dwarf stars. They do show some emission features and flare activity, both of which are a result of active chromospheres. As these stars are slowly contracting, and are no longer constrained by a link to a disc, the typical rotation period is shorter than that of CTTSs, at $\approx$3 days (Bodenheimer et al. 1995). For a more detailed discussion and references, see Appendix B.

1.2 The interpretation of T Tauri spectra

1.2.1 The optical emission

Given all of the features of T Tauri stars, it is near impossible to find a spectral feature that can be regarded as being from a single region of the system. Several authors have attempted to determine methods that separate the excess emission from the photospheric component and allow all TTSs to be compared with each other.

One of the first complete methodologies was described by Hartigan et al (1989). They fitted model spectra to CTTS data, the models were defined as a dwarf photosphere with a smoothly varying continuum on top. High resolution spectra enabled them to avoid strong emission lines. In order to achieve the smooth variation they separated their spectra into 15 Å bins, which meant they were unable to define individual emission lines. Despite this they showed that that the continuum included only an occasional emission line.

A more recent iteration of this technique was applied by Gullbring et al. (1998, GHBC hereafter). This method again assumed that the stellar photosphere could be approximated as a typical dwarf or WTTS spectra. The higher resolution spectra of this study allowed the actual emission spectrum to be calculated.

If the relative veiling, r, is defined as the ratio between the excess flux, F_E, and the photospheric continuum, F_C^*, it is possible to calculate this factor in terms of the main observables, the ratio of line flux to nearby continuum for CTTSs and model photo-

spheres, $\frac{F_l^T}{F_c^T}$ and $\frac{F_l^*}{F_c^*}$ respectively (assuming that F_E is constant across the photospheric line). F_l^T, CTTS line flux, F_c^T, CTTS continuum flux F_l^*, photospheric line flux and F_c^*, photospheric continuum flux.

$F_E = rF_c^*$ and $F^T = F^* + F_E$, therefore:

$$\frac{F_l^T}{F_c^T} = \frac{F_l^* + rF_c^*}{F_c^* + rF_c^*} \tag{1.1}$$

$$\frac{F_l^T}{F_c^T} = \frac{\frac{F_l^*}{F_c^*} + r}{1 + r} \tag{1.2}$$

$$\frac{F_l^T}{F_c^T} - \frac{F_l^*}{F_c^*} = r\left(1 - \frac{F_l^T}{F_c^T}\right) \tag{1.3}$$

$$r = \frac{\frac{F_l^T}{F_c^T} - \frac{F_l^*}{F_c^*}}{1 - \frac{F_l^T}{F_c^T}} \tag{1.4}$$

Using absorption lines that are thought to be free from excess emission lines, it is possible to apply this equation to CTTSs using template photospheres of WTTSs and dwarfs. GHBC used this and reddening corrections to derive the spectrum of the excess as seen in figure 1.2. The main lines that can be seen in this spectrum are the Hydrogen Balmer series, which were originally observed in the discovery of TTSs. There is also strong emission from the Ca II H and K lines as well as many lines from Fe I and Fe II.

The other important measurement, which has enabled some idea of the location of this emission excess to be determined, is the shape of the emission lines. A thorough study of this feature was made made by Edwards et al. (1994), using previously published data and high resolution optical spectra. The typical emission line profile of a CTTS combines a redshifted absorption minimum in the red wing and some evidence of a lower column density outflow, such as blue shifted absorption features in Hα. Models, such as those developed by Muzerolle, Calvet & Hartmann (1998) and previous derivations (Hartmann, Hewett & Calvet, 1994), can explain these gross features with a dipole magnetic field around the star trapping material into free falling accretion columns. These models require the infalling matter to have a mean temperature of at least 6000 K in order to produce the required profiles (Muzerolle et al. 1998). If several line profiles have been observed it is possible to determine the temperature of individual emitting regions, Muzerolle et al. (1998) determine a gas temperature of

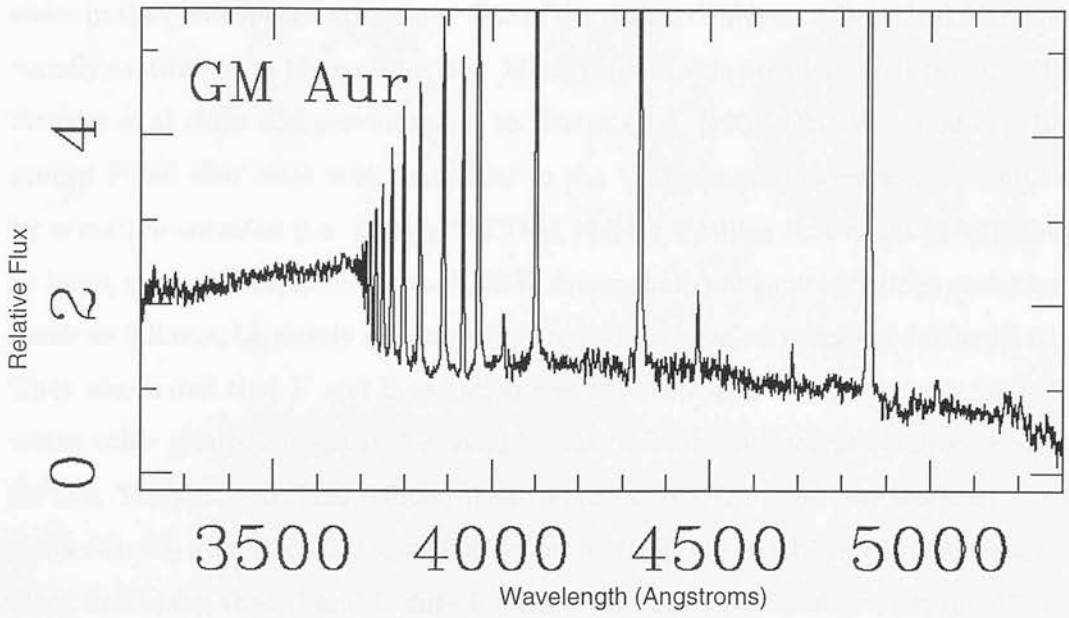

Figure 1.2: An excess emission spectrum from Gullbring et al. (1998)

≈10,000 K for BP Tau. The outflows that are measured in most CTTSs are thought to be stellar winds.

Both the free fall accretion columns and large stellar winds require that CTTSs have large magnetic fields when compared with equivalent dwarfs. Whilst each model has a different lower limit on the strength of this field, most agree that it must be ∼0.1 T. Recent measurements have suggested that fields of several 0.1 T do indeed exist on T Tauri stars (Johns-Krull et al., 1999, Guenther et al., 1999, Basri, Marcy & Valenti 1992).

The models are not yet accepted as being fully-consistent with observations, nor are the observations thought to be unambiguous; for a critique see Safier 1998.

1.2.2 The photospheric component

Given the differences in surface gravity and magnetic fields between TTSs and MS dwarfs, the group of stars they eventually form, it is not surprising to find some differ-

ences in the photospheric spectrum. One of the clearest differences is optical variability, usually attributed to large cool spots. Much work in this area has been performed by Bouvier et al (1997 and previous) and by Herbst et al. (1994, HHGW hereafter). Both groups found that stars with variability in the UBV range that were not dominated by accretion emission (i.e. mostly WTTSs), display features that could be attributed to large, cool, photospheric spots. HHGW found that cool spot variations could be as much as 0.8 m_V, be steady over many years and had period ranges of 0.5 to 18 days. They also noted that U and B variation was not related to this periodicity, and that whilst other groups suggested this could be due to flares, they found no direct evidence for this. Bouvier et al. (1995) found their results for WTTSs to be best matched by cool spots ranging from 500-1500 K with areas in the range 0.5 to 60% of the stellar surface. They also claim that U and B data indicates that hot spots cannot exist on WTTSs, as these would show greater variability than is observed, although their models assume the spectra can be represented as black bodies and therefore ignores the large changes that occur in the spectra over the temperature range considered (4500-9000 K).

The effect of the lower surface gravity on TTSs compared to dwarfs (due to their larger size) is not often considered, as their spectra are far more comparable to dwarfs than giants. Piorno Schiavon, Batalha & Barbury (1995) presented detailed analysis of high resolution spectra to determine the surface gravity of TTSs using line depth ratios (LDRs) which are independent of any flat continuum. They found values of $\log g$ in the range 3.8 to 4.5 for stars that had previously been given lower values. This compares to the typical G-M dwarf value of $\log g = 4.4 - 5$, which increases with decreasing temperature (Gray, 1992). Piorno Schiavon, Batalha & Barbury (1995) note that the differences in surface gravity only produces a 'strong' dependency on lines for T_{eff} <4400 K.

Greene & Lada (1996) surveyed TTSs across several star forming regions in the near-I.R.. They compared the equivalent widths (E.W.) of several lines, which is an equivalent technique to LDRs. This produced results which showed that the surface gravities of the TTSs lay between those of dwarfs and giants, although this technique could be affected by other parameters (such as veiling) so individual gravities could not be determined.

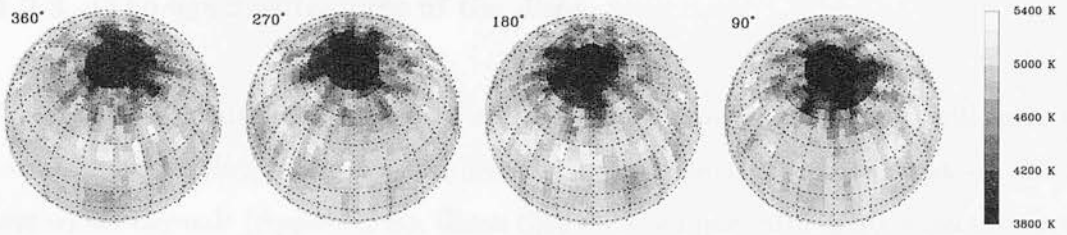

Figure 1.3: A doppler image of V987 Tau from Strassmeier & Rice (1998)

Doppler imaging has been performed on WTTSs by several groups looking for photospheric features (Doppler images of CTTSs are dominated by accretion infall zones). V410 Tau has been observed by Hatzes (1995) and Rice & Strassmeier (1996) and V987 Tau has been observed by Jouncour, Bertout & Bouvier (1994) and Strassmeier & Rice (1998). Rice & Strassmeier find large cool spots on both objects. On V410 Tau these are found at all latitudes and V987 Tau has only one polar spot covering 6% of the surface. They note that whilst polar spots are a common feature of other active stars, such as RS Canum Venaticorum (RS CVn) stars, only 2 WTTSs have been observed with such a spot. They also observe features on both stars that are warmer than the underlying photosphere, V410 Tau has hot features that are 500 K hotter and V987 Tau has features $\sim$100 K hotter (see figure 1.3). Strassmeier & Rice (1998) regard these as being within the limits of the expected photospheric temperature for V987 Tau. The spots seen on V410 Tau were regarded as being real features, their presence in all the lines used for the map construction suggesting they must be of a photospheric origin, rather than resulting from lines which are sensitive to chromospheric activity (Rice & Strassmeier 1996). The images produced by the other two groups show cool spot activity very similar to that of Rice & Strassmeier, but the techniques applied would not show the warmer regions that have been suggested. Hatzes (1995) argued that great care must be taken when using unconstrained reconstruction methods as the number of features which appear hot or cool is dependant on the photospheric temperature selected.

1.2.3 The spectral features of the discs

Standard disc models predict that a accretion disc around a young star will have a temperature varying from ≈2500 K at the star-disc boundary to 150 K at ≈5 A.U. and cooler beyond. (Appendix B). Given that the discs have atmospheres, as they are optically thick and have a vertical temperature structure, it would be expected to see a whole range of features, from cool star like molecular bands in the inner disc, to H_2O ices in the outer regions (Najita et al., 2000). Much of the work on observing these features has yet to be done. For the inner regions any emission will be combined with that of the accretion columns and so requires detailed modelling. For the outer regions, mid-I.R. spectra are required due to their cool temperatures, this needs instruments such as the ISO satellite and MICHELLE on the UKIRT and GEMINI telescopes, data from which is either just starting to be produced, or has not yet been taken.

The observational work that has been done so far is based on I.R. emission lines of either CO (Carr 1995) or H_2O. These lines are thought to have formed in a vertical temperature inversion region in the disc atmosphere, caused by irradiation from the star or the accretion shock front. These emission lines show very clear rotational profiles, with the H_2O lines being narrower than the CO lines, indicating that the cooler (H_2O) regions are further out in the disc, as predicted by theory (Najita et al. 2000).

1.2.4 Extinction effects on the spectra of T Tauris

When extracting the object spectra, or interpreting photometric data from TTSs, it is important to calculate the correct level of interstellar extinction. As TTSs are normally associated with dense dust clouds, the extinction cannot be assumed to be the same as a typical MS star. The extinction is defined as:

$$A_\lambda = -2.5 \log_{10} \frac{I_{\lambda(f)}}{I_{\lambda(i)}} \tag{1.5}$$

Where f is the final intensity (i.e. observed) and i is the initial intensity. A_λ is usually parametrised using two terms and least-squares coefficients fitted to stars of known

extinction. This takes the form:

$$A_\lambda = A_V \left(a(x) + \frac{b(x)}{R_V} \right) \tag{1.6}$$

Where R_V is $A_V/(A_B - A_V)$, the denominator is the extent to which the objects $B-V$ colour exceeds that expected due to extinction. Cardelli, Clayton & Mathis (1989) used photometric data in filters from U to L on stars of known spectral type to determine the terms a and b to be:

Infrared: $0.3\ \mu\text{m}^{-1} \leq x \leq 1.1\ \mu\text{m}^{-1}$. (0.91 to 3.33 μm)

$$a(x) = 0.574x^{1.61} \tag{1.7}$$

$$b(x) = -0.527x^{1.61} \tag{1.8}$$

Optical: $1.1\ \mu\text{m}^{-1} \leq x \leq 3.3\ \mu\text{m}^{-1}$ and $y = (x - 1.82)$. (0.3 to 0.91 μm)

$$\begin{aligned} a(x) = {} & 1 + 0.17699y - 0.50447y^2 - 0.02427y^3 + 0.72085y^4 + 0.01979y^5 \\ & -0.77530y^6 + 0.32999y^7 \end{aligned} \tag{1.9}$$

$$\begin{aligned} b(x) = {} & 1.41338y + 2.28305y^2 + 1.07233y^3 - 5.38434y^4 - 0.62251y^5 \\ & +5.30260y^6 - 2.09002y^7 \end{aligned} \tag{1.10}$$

Vrba, Coyne & Tapia (1993) examined the extinction properties of the ρ Ophiuchus cloud. They used photometric measurements of stars with known spectral types to determine values of R_V within the cloud. After applying several tests to ensure there were no unusual stars (e.g. TTSs) in their sample they found 12 stars which could be used. They found that R_V varied from the interstellar value of 3.1 to ≈ 5.2, with a slight trend of increasing R_V with A_V. The two extreme cases are shown in figure 1.4.

Both the trend with A_V and the shape of the A_λ/A_V curve suggest that some grain coagulation is taking place. As the majority of dust absorption occurs when grain size $\approx$ wavelength, larger grains mean less absorption in the blue, as seen in figure 1.4. The trend with A_V indicates that the grains are larger where they are denser, which is the result predicted from models of turbulent coagulation (Vrba, Coyne & Tapia 1993).

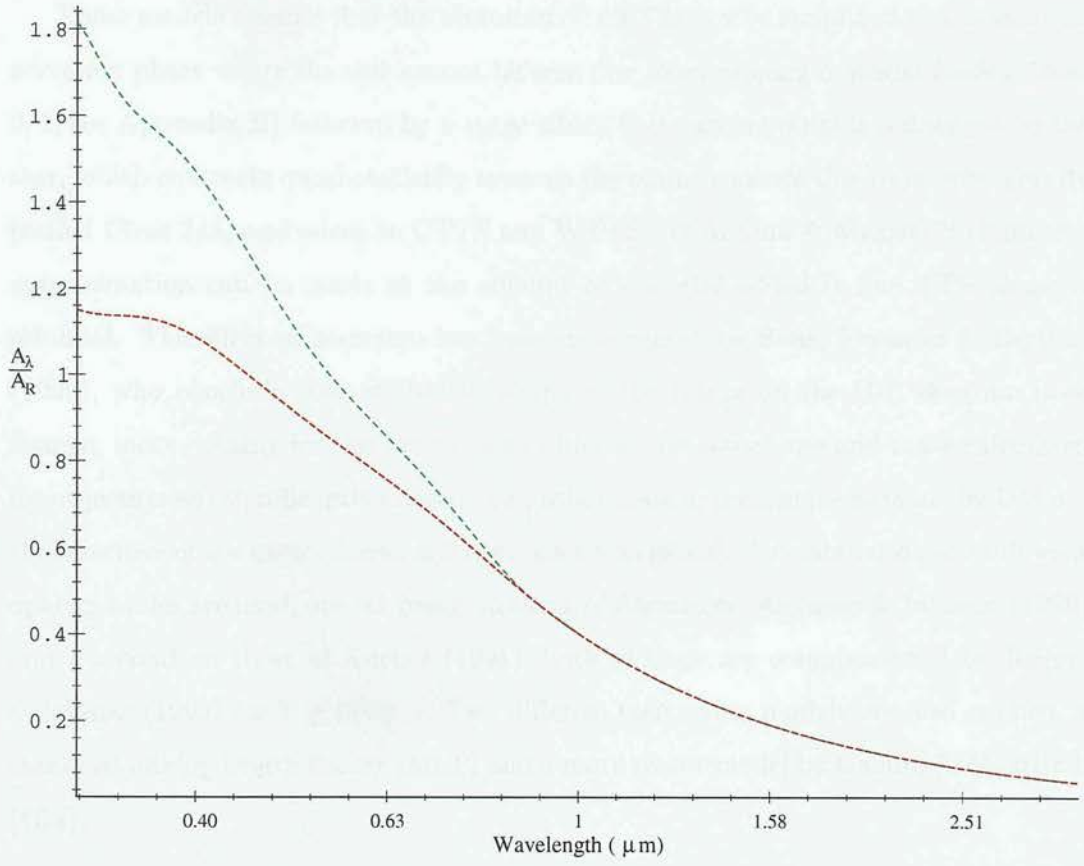

Figure 1.4: The extreme extinction curves for ρ Ophiuchus, the green line has the interstellar value of R_V=3.1 and the red has R_V=5.2. Note the logarithmic wavelength scale.

1.3 The ages of T Tauri stars

It was originally realised that TTSs were young stars due to their association with short lived OB stars (1-5 Myr age for the systems, Herbig 1962), and the presence of Lithium in their spectra (section B.4). Unfortunately neither of these facts gives a clear indication of age, associations only show that the stars have existed for 1-5 Myr, a small fraction of their life span, and Lithium burning requires many complex calculations due to the presence of convective mixing (section B.4). The method of age determination favoured by most authors is by direct comparison with a theoretical H-R diagram (Alcalá et al. 1997, Luhman & Rieke 1998, Ghez et al. 1997a amongst others), normally those of D'Anotona & Mazzitelli (1994, DM).

These models assume that the evolution of a TTSs can be simplified to 2 stages: an accretion phase where the star cannot be seen due to enveloping material (called Class 0/1, see Appendix B) followed by a stage where there are no outside influences on the star, which contracts quasi-statically towards the main sequence due to its own gravity (called Class 2/3, equivalent to CTTS and WTTS). D'Antona & Mazzitelli claim this approximation can be made as the amount of material added in the TTS phase is minimal. The effect of accretion has been investigated by Siess, Forestini & Bertout (1999), who conclude that whilst the shape of the tracks on the H-R diagram does change, most notably for the lowest mass objects, the actual age and mass calculated for objects is not significantly altered. The other main approximations made by DM are the opacities of the atmospheres and the convection model. A combination of 3 different opacity tables are used, one set based on those of Alexander, Augason & Johnson (1989) and a second on those of Kurucz (1991), both of these are complemented by Rogers & Iglesias (1992) for $T \geq 6000$ K. Two different convection models are also applied, a standard mixing length theory (MLT) and a more recent model by Canuto & Mazzitelli (CM).

Most authors compare their data to the "CM Alexander" set, though DM do note that care needs to be taken when interpreting the results of any tests that use these models. The four give slightly differing results and whilst the "CM Alexander" set is based on the most recent physical model it does not necessarily give the best results for all stars considered.

A typical use of these models can be found in Alcalá et al. (1997). This takes data from a previous paper (Alcalá et al 1995) to place a selection of TTSs from the Chamaeleon star forming region on the H-R diagram. T_{eff} is determined from the spectral class of the stars using empirical rules derived for dwarf stars and luminosities were either taken from dereddened SEDs or using a known relationship between the I magnitude and bolometric luminosity. All the stars were assumed to be at the same distance as the cloud itself (150 pc).

These methods of placing stars on the H-R diagram contain many underlying assumptions, even before physical parameters are taken from theoretical evolution tracks.

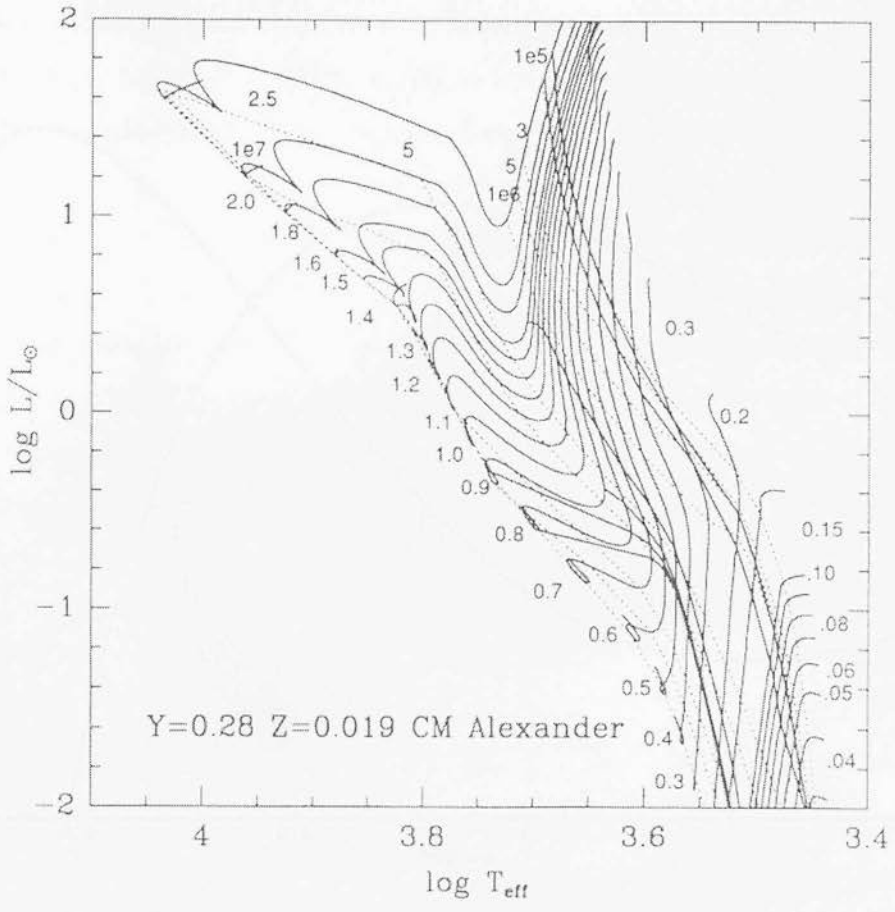

Figure 1.5: A theoretical H-R diagram from D'Antona & Mazzitelli (1994). The figures at the ends of the solid lines refer to the mass of the model on that track, the dotted lines are isochrones, with ages labelled, the two solid lines on the left are the average locus of D burning.

The main assumption is that the underlying spectra are the same as those of dwarf stars of the same temperature. Due to all the other spectral features of T Tauri stars, as covered previously, this process requires careful analysis. The standard method is to use medium to high resolution spectra to select absorption lines that are thought to be free from emission and either compare these directly to dwarf standards or, in cases with large optical veiling, to temperature sensitive LDRs. Several studies that have re-examined the spectral types of previously observed stars have found discrepancies due to differing reduction techniques (e.g. ROXs 29 has been measured in a range from K7 (Cohen & Kuhi 1979) to K4 (Padgett 1996)).

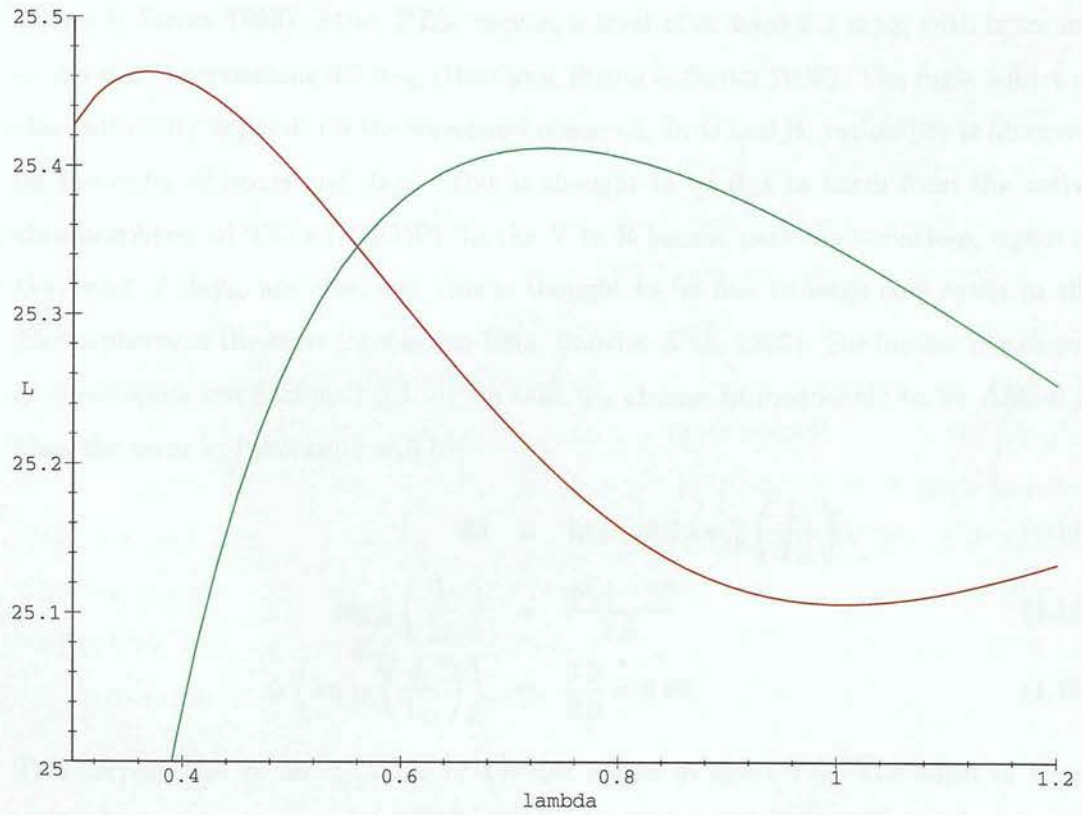

Figure 1.6: A theoretical diagram showing the minimum accretion component for a CTTS. The green line is a 5000 K, 1.4 $R_\odot$ black body, the red line consists of a 10000 K black body covering 7% of the 5000 K body (this represents the optical excess) and a thin accretion disc, accreting at 10^{-7} $M_\odot\,yr^{-1}$.

Determining the luminosity can also introduce systematic errors. The first part of this is to separate stellar and accretion flux. The DM models do not take account of accretion, so any flux, either from the disc or from accretion columns, must be removed from the SED before comparisons can be made. The standard method of separating the components is to chose a photometric band which is thought to be least affected by any disc or star/disc interaction emission. Most authors use the R band to do this (Strom et al., 1990, Hughes et al., 1994), as it can be shown that the effects of accretion are minimised in this region, see figure 1.6.

Whilst there are several systematic errors introduced in making the above assumptions (such as unresolved binaries, incorrect determination of spectral type and incorrect

de-reddening), the main source of error is the intrinsic variability of the star (Hartigan, Strom & Strom 1993). Most TTSs vary at a level of at least 0.1 mag, with more extreme stars approaching 0.5 mag (Hartigan, Strom & Strom 1993). The main source of this variability depends on the waveband observed. In U and B, variability is observed on the order of hours and days. This is thought to be due to flares from the active chromospheres of TTSs (HHGW). In the V to R bands, periodic variations, again of the order of days, are observed, this is thought to be due to large cool spots in the photospheres of the stars (Mekkaden 1999, Bouvier et al., 1995). For further discussion of these spots see Section 1.2.2. If we take the change in magnitude to be $\Delta M \approx 0.2$, then the error in luminosity will be:

$$M = M_{\odot} - 2.5 \log_{10}\left(\frac{L}{L_{\odot}}\right) \tag{1.11}$$

$$\log_{10}\left(\frac{L}{L_{\odot}}\right) = \frac{M_{\odot} - M}{2.5} \tag{1.12}$$

$$\Delta\left(\log_{10}\left(\frac{L}{L_{\odot}}\right)\right) = \frac{0.2}{2.5} = 0.08 \tag{1.13}$$

This corresponds to an error bar of 1.6 tick marks in figure 1.5. The effect of these errors depend on the age of the TTSs. If the star is young it will still be on the vertical Hayashi track, and the error in luminosity could correspond to an age difference of around 5×10^5 years for the higher mass stars. If the stars are older, on the horizontal section of the tracks, then the error in the mass estimate could be as much as 0.5 $M_{\odot}$ (between 2 and 1.5 $M_{\odot}$ around $\log_{10}(T_{eff})$=3.7).

The other source of error in determining the luminosity will be the error in the distances to the stars. It is usual to adopt a single distance for an entire star forming region (Alcalá et al. 1997). As the volumes of these regions are small compared to their distance, the errors introduced are usually negligible, but recently several TTSs have been found at a large distance from the cloud they were thought to belong to (Favata et al. 1997), although the exact nature of these objects has yet to be determined.

With the distinct possibility of misclassifying TTSs when only a small spectral range is considered, and with the range of systematic errors that can be introduced when determining the luminosity, any attempt to determine the age and mass of an individual star by comparison with theoretical evolutionary tracks will have intrinsically

high errors. If the known objects in a cloud are all studied using the same technique, then it is possible to draw conclusions about the nature of that region.

A recent example of this is the study by Luhman & Rieke (1998) of the young cluster L1495E. They found that careful analysis of I.R. spectroscopic data gave a complete sample to a dereddened K=10. Comparison of this data with theoretical H-R diagram tracks produced a mass function (MF). The DM tracks are thought to produce the most reliable results, as the cloud is found to be roughly coeval. The MF produced by Luhman & Rieke (1998) agrees with the standard field initial MF (IMF) down to $\sim 0.3\,M_{\odot}$, where the MF becomes flat in log space. A similar result is found in other star forming regions (ρ Oph and NGC 2024, Comeron et al. 1996, Strom, Kepner & Strom 1995). As these regions represent a wide range of star forming scales, it is possible that this change in the MF represents the actual galactic IMF, although Luhman & Reike (1998) point out the need for improved modelling of low mass stars to ensure the difference is not just a result of the theoretical H-R diagram tracks used.

1.4 T Tauri stars with multiple spectral types.

Despite the detailed picture of T Tauri stars and their environment that has built up from investigation of their spectra, there are still some observations that cannot be fully explained using the normal models.

Bouvier & Appenzellar (1992, BA) found several spectra which they described as 'peculiar'. The main features of these were large changes in spectral type for the range of their observations (4000-7200 Å). This was seen very clearly in three objects (ROXs 3, 21 and 47A), as K4 spectra around the G band (4300 Å), whereas TiO absorption around 6600Å indicated a spectral type of M0 (see figure 1.7). These peculiar spectra were seen in both CTTSs and WTTSs. BA determined that these features must be photospheric, as the spectra did not show any large chromospheric features, such as Ca II H and K emission, observed in very active stars. They determined that there must be at least 2 regions in the system, one $\approx$ M0 region and an $\approx$ K0 region which has a projected size 7% that of the $\approx$ M0 region. They argue that it is most likely that these

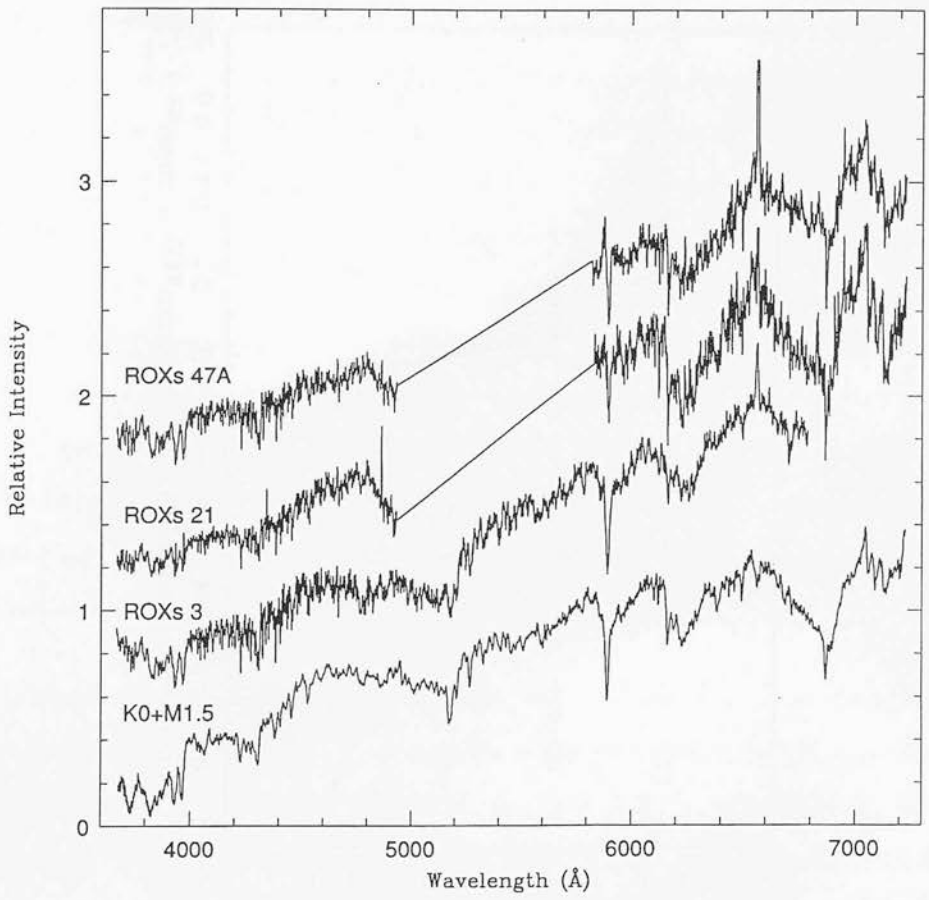

Figure 1.7: BA's peculiar spectra, the spectral type in the blue, is much higher than that in the red, from BA

regions lie on the stellar surface, as a binary system with these parameters would have a large difference in the ages of the stars (to account for the size differences, given the assumed temperatures) and such systems have not been observed.

GHBC also found some peculiar effects in the WTTSs they were using as standards for their study of CTTS emission. They found that using WTTSs as standards gave differing results to dwarf stars of the same temperature, the difference appearing as a large change in the slope of the derived emission spectrum. To discover if this was a common effect they examined the colour properties of WTTSs in Taurus, dereddening the stars using V-R colours to compare them with MS stars. Figure 1.8 shows the results. It is clear that the WTTSs show redder colours with increasing wavelength in a way that is not seen to any degree in the comparable MS star.

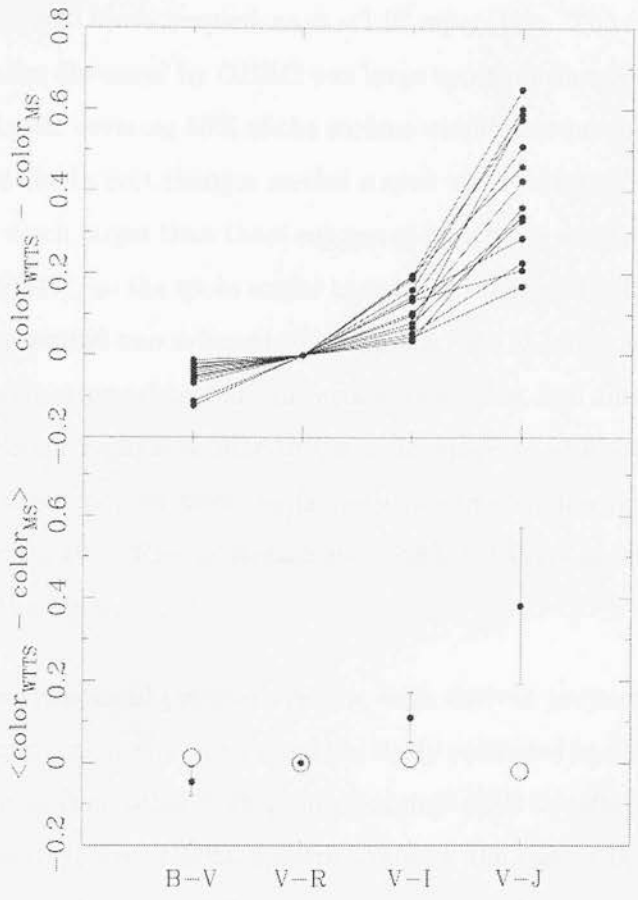

Figure 1.8: The colour anomalies of the WTTSs from Gullbring et al. 1998. The upper diagram shows the data for the WTTSs, the lower shows the mean values for the WTTSs and the data for an M0.5 dwarf star (open circles).

GHBC examined several sources of these anomalies. Errors in the calibration or spectral type were ruled out as the largest anomalies would imply a change in spectral type that would grossly alter some spectral features (TiO bands). The difference in the surface gravities between WTTSs and dwarfs was ruled out as similar colour anomalies are not seen in giants, where the much lower gravities would enhance any such effect. The anomalies look very similar to what would be expected from enhanced extinction effects, but it was found that to have a change in $V-J$ of just 0.3 would require R_V=5, which is around the largest observed for star forming regions (section 1.2.4). Binary systems were ruled out as it would be highly unlikely that all the stars observed could have unresolved companions; Ghez et al. (1997b) found that only 3-4 out of every 10

systems observed would have companions at $<1.2''$ separation. The only viable cause of the colour anomalies discussed by GHBC was large spots on the stellar surfaces. They found that a cool spot covering 50% of the surface would account for the mean change in $V-J$, but that the largest changes needed a spot which covered 70% of the surface. These figures are much larger than those suggested by studies which look for cool spots on TTSs (e.g. HHGW), so the spots would have to be different to those found in these studies. GHBC presented two different explanations, one of large, axisymmetric spots which would not give strong detections in variability studies, and another that the stars may have some hotter regions similar to the solar plage as well as cool spots. Both these ideas have some support from the Doppler imaging studies previously discussed (Section 1.2.2, Hatzes 1995, Rice & Strassmeier 1996), but there is no concrete evidence to choose one or the other.

It is these observations of peculiar spectra, with derived properties changing with observed wavelength region, that motivated the study presented in this thesis. To differentiate these features from other TTS properties they shall be referred to as "multiple spectral type" spectra/stars or MST spectra/stars for the rest of this work. It is only with a thorough understanding of the processes affecting the spectra of TTSs that all the techniques used to observe these objects can be compared without the introduction of systematic errors. This extends to the study of star forming regions, as properties such as the initial mass function and age are determined from the Hertzsprung-Russell (H-R) diagram, which requires an accurate determination of T_{eff} for the stars included. This study also offers the prospect of a greater understanding of the structure of TTSs which may give insight into unresolved questions such as the level of magnetic activity and the variation of surface features when compared to MS stars.

Chapter 2

A high resolution near-I.R. search for MST stars.

MST objects have only been observed by BA and GHBC. To study the phenomena further, it was decided to perform a spectral search for MST stars. The study by GHBC suggested that the effect is very common in WTTSs, but the spectra in BA only reveal 5 candidate objects. A spectral study with greater sensitivity to the MST effect would both extend the number of known MST stars, and also demonstrate the extent to which this effect has been overlooked in previous studies.

The MST effect is manifested as a wavelength-dependent spectral type. Since previous studies have used optical spectra to determine the spectral type of TTSs, comparing near-I.R. results with previous studies will reveal MST stars. The near-I.R. provides a large enough difference in wavelength for any changes to be obvious, whilst not being dominated by any CTTS disc features other than continuum veiling (Appendix B). The data presented by GHBC shows that the MST features extend to the I.R. (figure 1.8) and the figures suggested by BA enable the theoretical effect in the I.R. to be calculated. Using BA's canonical figures of 5250 K and 3950 K for the two regions on a K0 star showing an MST spectrum, the flux difference for the regions at 1.6 μm can be

estimated. Assuming a black-body spectra:

$$B_\lambda(T) = \frac{2hc^2}{\lambda^5\left(e^{\frac{hc}{\lambda kT}} - 1\right)} \tag{2.1}$$

All but the exponential terms cancel in the ratio:	$\left(e^{\frac{hc}{\lambda kT_1}} - 1\right)^{-1} : \left(e^{\frac{-hc}{\lambda kT_2}} - 1\right)^{-1}$
For λ=1.6μm, T_1=5250 and T_2=3950 this is:	1.93 : 1
For the optical, λ=0.6μm, this is:	4.53 : 1

These two ratios show that the hotter region is 2.3 times more dominant in the optical than in the near-IR, so the MST spectra will be more obvious in the near-I.R., particularly in temperature sensitive lines.

2.1 The observation technique

To ensure that no other TTS features could be mistaken for MST, a technique similar to LDRs would have to be used. The near-I.R. region of CTTSs will include some emission both from the infall shock front and the accretion disc itself, although the effect is minimised around 1 μm (figure 1.6). Line ratios are independent from any continuum emission as follows:

The total continuum is the stellar continuum plus continuum emission: $F_C = F_{C*} + F_E$

The line flux is the stellar flux plus continuum emission $F_L = \alpha_\lambda F_{C*} + F_E$, where α_λ is an absorption coefficient. So the ratio of two line depths will be:

$$\frac{F_C - F_{L1}}{F_C - F_{L1}} = \frac{F_{C*} + F_E - \alpha_{\lambda 1}F_{C*} - F_E}{F_{C*} + F_E - \alpha_{\lambda 2}F_{C*} - F_E} = \frac{1 - \alpha_{\lambda 1}}{1 - \alpha_{\lambda 2}} \tag{2.2}$$

So the LDRs are only dependent on the absorption coefficients. LDRs are also independent of rotational broadening, as all lines are affected the same way (Gray & Johanson 1991). Any line characteristic that is proportional to the depth will also have this feature, e.g. the equivalent widths of Gaussian profiles.

2.2 The choice of instrument

Previous I.R. spectroscopic studies of T Tauris have been carried out by Greene & Meyer (1995), who observed ρ Ophiuchus in the 1.1-2.5 μm range. They found that their spectral resolution, R=720 or 500, did not allow them to measure line ratios as most of the lines were blends, and concluded that higher resolution data was required. Greene & Meyer (1995) used an 'I.R. spectral type', which could include some continuum from the disc and so is not always directly comparable with optical spectral types.

To overcome these problems it was decided to use a high resolution instrument. This both reduced the number of blends, and the short wavelength coverage ensured that there would be no slope or lines in the continuum emission.

Time was granted on the UKIRT telescope in Hawaii to use the CGS4 spectrometer. This instrument contains an echelle grating which enables high resolution spectra to be obtained in the near-I.R..

2.3 The choice of stars

In order to compare the results of this survey directly with those of BA, TTSs in the ρ Ophiuchus dark cloud were observed. The project was allocated 3 nights on UKIRT from 29^{th} May, with up to 6 hours a night on ρ Ophiuchus. The stars were selected by magnitude, spectral type and TTS classification to ensure a good sampling from the range of T Tauris. The young stars observed are shown in table 2.1.

2 sets of standards were also observed. A selection of hot standards were measured, these were required to determine the variation of instrumental response with wavelength; they were B3V to B5V stars. The second set were spectral standards: 8 late-type giants and 19 late-type dwarfs. These were used for spectral classification of the TTSs (see tables A.1 & A.2).

Object	A.K.A.	Spectral Type	Hα Å	V
ROXs 6	SR 4	K6	84	12.8
ROXs 8	DoAr 21	K0	-0.6	13.9
ROXs 12		M0	1.2	15.4
ROXs 16	VSS 27	G9	19	16.7
ROXs 21	SR 12a	M2	4	13.4
ROXs 29	SR 9	K4	12	11.5
ROXs 39		K5	6	13.0
ROXs 42c		K6	1.6	12.5
ROXs 43b		K5	0.8	12.3
ROXs 44		K3	54	12.6
ROXs 47b		K3	-2.0	12.3
SR 24n		M0	24	16.0
SR 24s		K2	76	15.9
LKHα 172		K4	28	14.5
LKHα 188		G8	44	13.6
LKHα 191		K0	22	12.8

Table 2.1: The young stars that were observed. A.K.A, Also known as. Hα, equivalent width of Hα, $> 5 \equiv$CTTS. V, magnitude in V.

2.4 The Observations

As ρ Oph was only visible for 6 hours around midnight the spectral standards were observed in the time after sunset and before sunrise. The echelle grating gave high resolution spectra (R$\approx$20,000) from 1.618 μm to 1.636 μm. This region was chosen as it contains a selection of molecular and metal lines. The many OH lines will be sensitive to cool regions as this molecule dissociates around $\approx$5000 K in dwarf stars, the CO band head at 1.619 μm will enable easy identification for the giant stars. The metal lines are mostly Fe features, these will provide a good contrast with the OH lines. The detector was stepped in $\frac{1}{3}$ of a pixel width to ensure that the whole spectrum was fully sampled. A journal of the observations is shown in tables 2.2-2.4.

Object	Sp. Type	UT start	Exposure (s)	R.A.	Dec	Exp
BS 6141	B3V	11:46:42	4.0	16:27:09.08	-25:00:24.8	2
ROXs 42c	K6	11:56:05	40.0	16:28:13.06	-24:27:36.0	8
ROXs 43b	K5	12:36:31	40.0	16:28:18.02	-24:23:39.4	4
ROXs 8	K0	12:56:40	20.0	16:23:01.05	-24:16:49.0	4
BS 6308	M1III	13:12:21	1.0	16:56:53.07	-25:01:05.0	2
BS 8001	B5V	13:25:34	6.0	20:51:28.06	+44:11:48.8	2
LKHα 188	G8	13:37:48	80.0	20:56:35.08	+43:41:31.0	9
BS 7919	K2III	14:59:03	1.0	20:38:17.08	+43:16:50.0	2
BS 7969	K5III	15:04:02	0.5	20:46:10.03	+47:38:47.9	2
BS 7800	K7III	15:10:35	0.5	20:20:58.07	+40:51:53.0	2
BS 8699	M0III	15:17:52	0.2	22:49:46.08	+43:02:47.8	2
BS 7798	K0III	15:26:00	2.0	20:20:27.05	+45:38:03.1	2

Table 2.2: The journal of observations for May 29th 1996.

2.5 Reduction

All the data were reduced using the same process. Initial reduction from the telescope was performed using CGS4DR. This produced images of the oversampled frame. The CGS4 chip is 256x256 pixels, so the 3 step jitter pattern produced 256x768 images.

The system was used in its NDR (non-destructive read) mode with OBJECT–SKY pairs, so it was unnecessary to use either BIAS or DARK frames. CGS4DR automatically produced a FLAT frame as shown in figure 2.1, the bad pixel map (b.p.m.) fpa46_short was used for all the reductions and the FLATs were normalised by fitting a polynomial to an area specified by the b.p.m. (Daly 1995). OBJECT and SKY frames were divided by a FLAT as shown in figure 2.2.

Further reduction of the spectra was the performed using FIGARO routines. Each observation produced 4 image files, 2 SKY and 2 OBJECT. The process ISUB was used to subtract the SKY frames and the process EXTRACT was used to produce a 1-D spectrum from the required region. The two spectra thus produced were directly added

Object	Sp. Type	UT start	Exposure (s)	R.A.	Dec	Exp
BS 4456	B4V	05:32:41	5.0	11:32:06.04	+17:04:24.5	2
GL 486.1	G7V	05:49:59	5.0	12:46:19.07	+25:06:44.1	2
GL 471.1	K4V	06:05:42	15.0	12:29:16.08	+33:45:47.8	3
GL 459.2	K4V	06:16:05	15.0	12:14:13.09	+44:40:37.6	2
GL 480.2	K4V	06:28:57	5.0	12:38:26.06	+34:22:33.2	2
GL 450	M1V	06:41:37	15.0	11:48:31.04	+35:32:49.9	8
GL 526	M3V	07:03:16	5.0	13:43:17.09	+15:08:27.6	2
GL 454.3	K0V	07:17:18	15.0	11:59:45.01	+43:24:43.1	6
GL 443.1	K3V	07:34:28	5.0	11:44:21.03	+27:18:02.4	2
GL 459.3	M2V	07:45:14	15.0	12:16:53.01	+28:39:34.7	5
GL 484.1	K3V	07:57:56	5.0	12:44:42.05	+32:50:26.1	2
BS 6141	B3V	08:10:01	5.0	16:27:09.08	-25:00:24.7	2
ROXs 44	K3	08:17:15	40.0	16:28:31.05	-24:21:13.0	4
ROXs 47b	K3	08:39:39	40.0	16:29:21.00	-24:33:58.0	8
ROXs 8	K0	09:20:36	40.0	16:23:01.06	-24:16:50.6	7
SR 24s	K2	10:03:16	40.0	16:23:56.05	-24:38:54.7	8
BS 6141	B3V	10:45:06	5.0	16:27:09.08	-25:00:37.6	2
SR 24n	M0	10:55:57	40.0	16:23:56.04	-24:38:50.5	8
ROXs 6	K6	11:38:23	40.0	16:22:54.07	-24:14:01.0	8
ROXs 39	K5	12:20:08	40.0	16:27:33.06	-24:27:50.0	7
BS 6141	B3V	12:57:09	5.0	16:27:09.08	-25:00:25.4	2
BS 7507	B8V	13:08:26	10.0	19:42:50.00	-32:01:51.6	2
BS 7578	K3V	13:19:57	3.0	19:51:17.08	-24:04:20.4	2
BS 8382	K2V	13:29:25	3.0	21:56:19.01	-04:36:45.2	2
BS 8215	B3V	13:40:06	5.0	21:25:18.09	+36:54:32.5	2
BS 8086	K7V	13:48:11	1.0	21:04:57.02	+38:32:52.0	2
BS 8372	K5V	13:53:55	0.5	21:54:03.06	+21:00:05.9	2
LKHα 191	K0	14:01:37	40.0	20:57:17.08	+43:45:20.0	16

Table 2.3: The journal of observations for May 30th 1996.

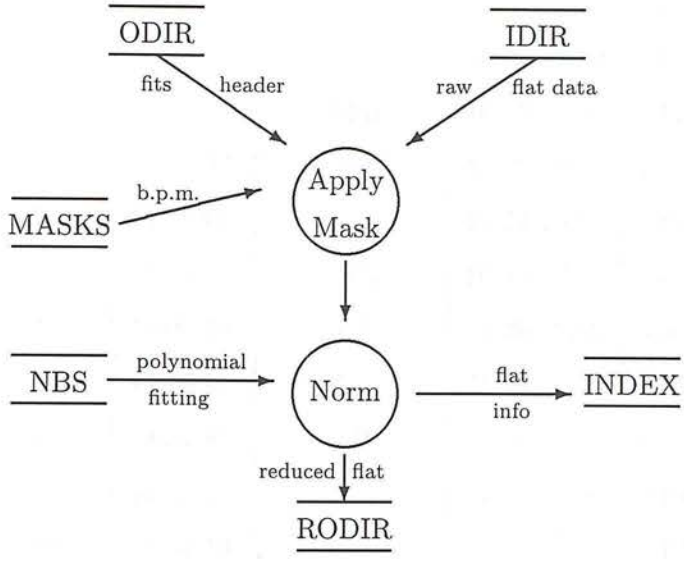

Figure 2.1: Reducing a FLAT (from Daly 1995)

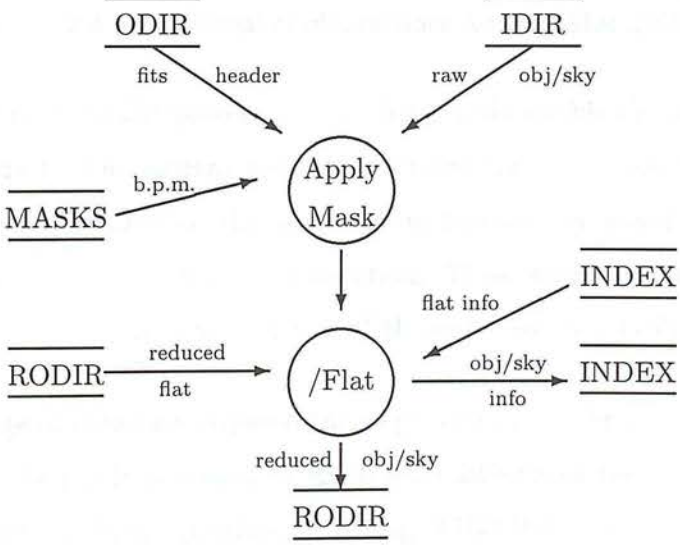

Figure 2.2: Reducing an OBJECT or SKY (from Daly 1995)

Object	Sp. Type	UT start	Exposure (s)	R.A.	Dec	Exp.
BS 6141	B3V	08:36:30	3.0	16:27:13.04	-25:00:38.3	2
SR 12a	M2	08:59:53	40.0	16:24:17.04	-24:35:03.3	16
ROXs 16	G9	10:32:31	40.0	16:23:45.01	-24:05:14.4	8
BS 6141	B3V	11:13:27	3.0	16:27:09.08	-25:00:24.9	2
ROXs 12	M0	11:19:00	40.0	16:23:25.02	-25:20:03.0	8
ROXs 29	K4	12:12:44	40.0	16:24:38.06	-24:15:26.0	8
BS 8215	B3V	13:06:14	9.0	21:25:18.09	+36:53:54.2	2
BS 8085	K5V	13:25:16	1.0	21:04:55.07	+38:32:38.5	2
BS 8086	K7V	13:27:35	1.0	21:04:57.00	+38:32:15.5	2
BS 8631	G4V	13:35:11	2.0	22:38:24.07	+14:17:05.9	2
BS 8455	G0V	13:44:49	2.0	22:07:56.03	+19:22:06.6	2
GL 725a	M4V	13:54:06	4.0	18:42:05.05	+59:34:39.3	2
BS 8517	M4III	14:03:45	0.3	22:18:42.04	+26:41:16.8	2
BS 8833	G8III	14:13:53	2.0	23:10:55.04	+10:47:34.4	2
BS 8781	B9III	14:18:03	0.6	23:02:16.03	+14:56:07.4	2
LKHα 172	K4	14:32:04	40.0	20:50:40.06	+44:05:45.0	8

Table 2.4: The journal of observations for May 31st 1996.

to each other using the IADD process. For the hot standards this was all the processing that was performed. The spectra were then divided by the closest hot standard in airmass using the IDIV process, this was done to remove any wavelength dependent instrumental response or atmospheric absorption. These spectra were output as text files for further reduction using the NDF2ASCII routine in the CONVERT package.

The next stage of reduction required the ripple introduced by the stepping process to be removed. The ripple is caused by slight level differences between the exposures of each step, resulting from variations in seeing. FIGARO contains a routine called IRFLAT that is supposed to remove this ripple. This makes the assumption that the ripple is constant across the whole spectrum. It was found that whilst this routine de-rippled the central area correctly, the edges contained some residual systematics, as is shown in figure 2.3. To overcome this, a program (QUAT) was written to process

Normalisations given by QUAT		
1.03221	0.980296	0.988403
1.03375	0.977808	0.989004
1.05255	0.964662	0.98447
1.07067	0.950924	0.978894
Normalisation given by IRFLAT		
1.043626	0.9701726	0.9862012

Table 2.5: The normalisations for de-rippling given by QUAT and IRFLAT for BS 8086

the files by splitting the spectra into quarters and apply different de-rippling weights in each quarter. Table 2.5 shows the relative weights applied by the two programs for a typical spectrum, it can be seen that whilst IRFLAT does produce a ripple similar to those of QUAT, the differences between the quarters is significant. This is can again be seen in figure 2.3 where the region of the spectrum beyond the 600^{th} pixel produced by IRFLAT clearly contains more noise than that produced by QUAT.

The spectra were then smoothed using a Hanning function, figure 2.4. This was chosen to match the stepping pattern of the observations, each pixel in the reduced spectra contains 1/3rd of the flux of its nearest neighbours. Convolving the Hanning function with the spectra will therefore smooth with a weighting comparable to the steps.

This completed the reduction of the spectra. Line identification was performed by comparing the spectra with the solar atlases produced by Livingstone & Wallace (1991 and Wallace & Livingstone 1992). The photospheric atlas was used for the hotter stars and the spot atlas was used for the cooler objects. It was found that each spectrum contained roughly 40 strong lines, with blending occurring between metal and OH lines in all but the hottest stars. Because of this it was decided that the standard spectral inspection packages (FIGARO, IRAF) would require too much manual input to reliably extract line information from the spectra, instead a program was written (REDCGS) that performed both the final stages of reduction and line fitting.

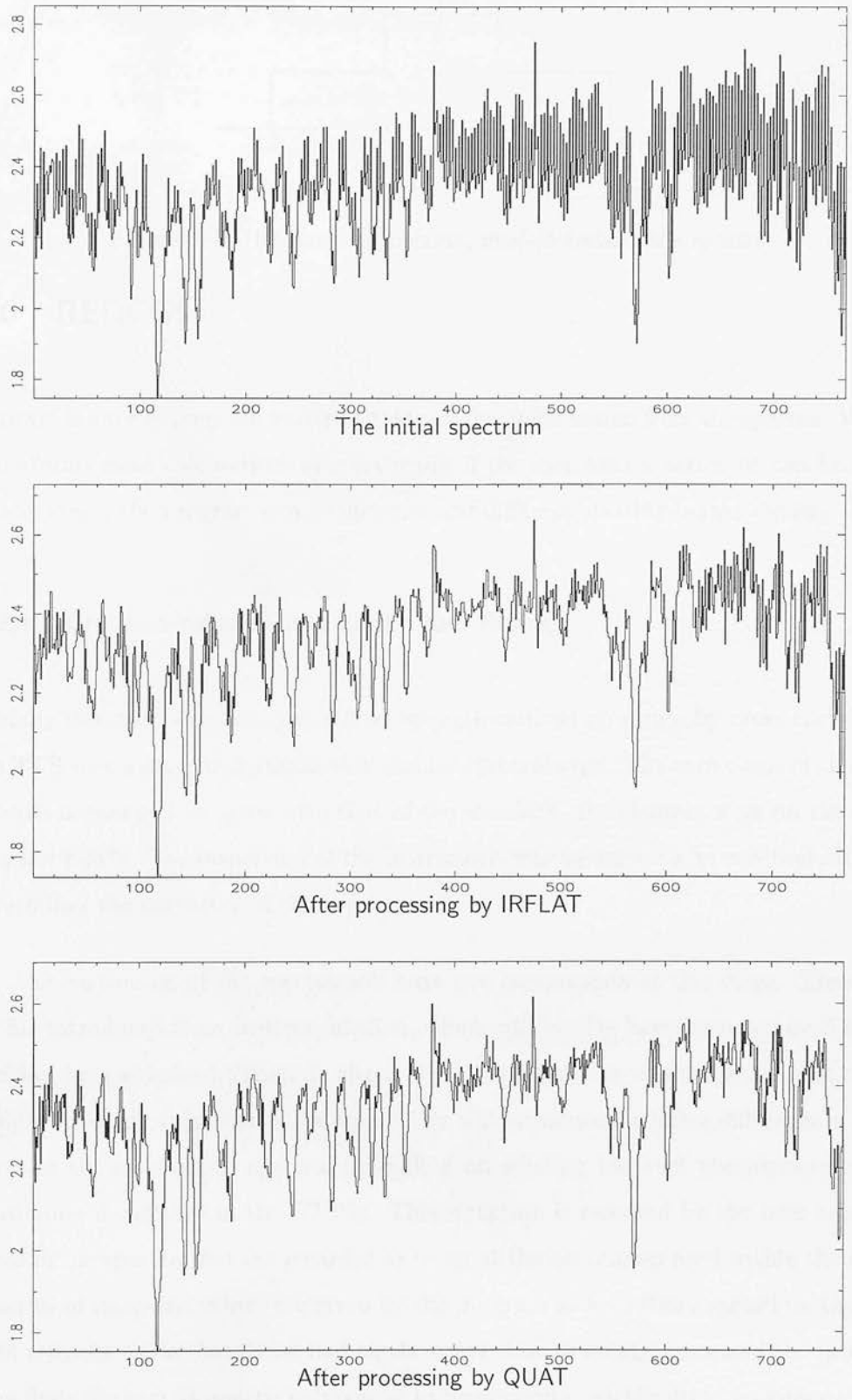

Figure 2.3: The comparison of the de-rippling methods.

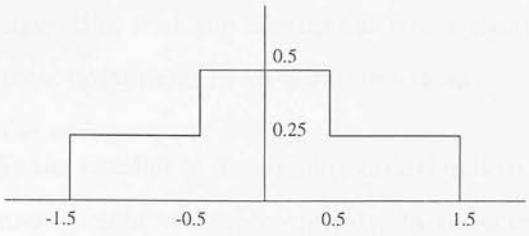

Figure 2.4: The Hanning function, used to smooth the spectra.

2.6 REDCGS

REDCGS is a C++ program written to extract line information from the spectra. Whilst it performs most calculations automatically, if the user feels a better fit can be made at any stage, the program can be stopped and different starting points chosen.

2.6.1 Cross-correlation and continuum fitting

Initially REDCGS detects any slight wavelength calibration errors by cross correlating the TTS spectrum with a standard of similar spectral type. The zero point of the TTS spectra is changed to agree with that of the standard, the changes were on the order of a few pixels. The dispersion of the instrument was assumed to be constant. It next determines the curvature of the continuum.

The continuum of the spectra will have two components at this stage. There is a profile introduced from instrumentation, which will mostly have been removed in the division by a standard. There is also a slight curvature across the spectra due to the basic black-body spectrum of the stars. This will introduce a relative difference of 2-3% between the ends of the spectra, depending on whether the cool photosphere or hot continuum dominates in the CTTSs. This structure is removed by the user selecting areas in the spectra that are regarded as being at the continuum level within the noise. A series of inter-line values are given by the program as an initial suggestion, the user then removes those that lie on bad pixels or are close to strong lines, and the program then finds the best fit quartic polynomial to these points. All the fitted polynomials had

small higher orders, suggesting that the continuum was a simple curve. The spectra were then divided by their continuum fit to normalise them.

In some of the TTSs the number of lines and poorer signal to noise ratio meant that the selection of continuum points was more difficult. In these cases the continua were compared with those that were previously calculated and were recalculated if there were any gross differences, or else the initial continuum was assumed to be flat within the noise.

2.6.2 Wavelength calibration and line shape

Once a spectrum had been cross-correlated and checked for level continuum, a model spectrum is fitted to it. The modelling was done in three stages. First a table of line wavelengths was read in, and a calibration of wavelength to pixel number is performed. This is done rather than wavelength calibrating the spectrum data as this would produce a variable instrumental profile across the spectra. A 'typical' line is then chosen by the user, one which is free from blending and bad pixels, so that the program could fit a single gaussian profile to it.

The profiles of the lines will in fact be a convolution of the instrumental profile (an $\approx$30 kms^{-1} Lorentz profile, due to the square aperture of the instrument convolving with the telescope instrumental profile), the Hanning smoothing function and the line profile of the star which could be up to 20 kms^{-1} wide (table 2.1). Rather than attempt to find the exact profile for each spectrum, which was impossible as all the spectra contain so many lines that the wings of the profiles were blended, it was decided to fit a gaussian to the peaks of the lines. Whilst this was an approximation to the profile it provides more robust measurement than just measuring the line depths, as it is less affected by noise.

2.6.3 Line fitting

The width of the gaussian was calculated from the strongest line in the spectrum, this was then used to produce a model spectrum from a list of reference wavelengths. It is assumed that all lines will be centred on their reference wavelength. An initial estimate was given by picking the lowest point of each referenced line and assuming this was the true line depth. The program then passed through each line and adjusted its amplitude to minimise the least squares difference in the region of that line (all pixels were assumed to have approximately equal errors when compared to the errors introduced by blending and bad pixels on the line profile). This passing procedure was iterated to improve the fit to blended lines.

If a significant line was found to lie close to a bad pixel (which appear as triangular features in the spectra, due to the smoothing), the user was able to flag the pixel as bad interactively. The program would then refit the data, masking out the region that was flagged as bad.

This completed the modelling stage, the program finally produced a file listing the equivalent widths of the lines and an error for each line found by the least squares fit of the real line profile to the modelled one. An example of the fit is shown as the red line in figure 2.5.

2.7 Data analysis

The first stage of the data reduction was to determine which lines could be used for analysis, figure 2.5 shows the lines found in this spectral region. Not all of these lines will be visible in all of the spectra as the OH lines become weaker as the photospheres become hotter. For a line to be suitable for analysis it must behave consistently under changes in both temperature and surface gravity. This immediately ruled out all the ones that were potential metal/OH blends, as these will peak for both hot and cool atmospheres. This also ruled out the region immediately beyond 1.619 μm, as this is the CO Δv=3 band head. Inspection of figure 2.5 shows that there are only three

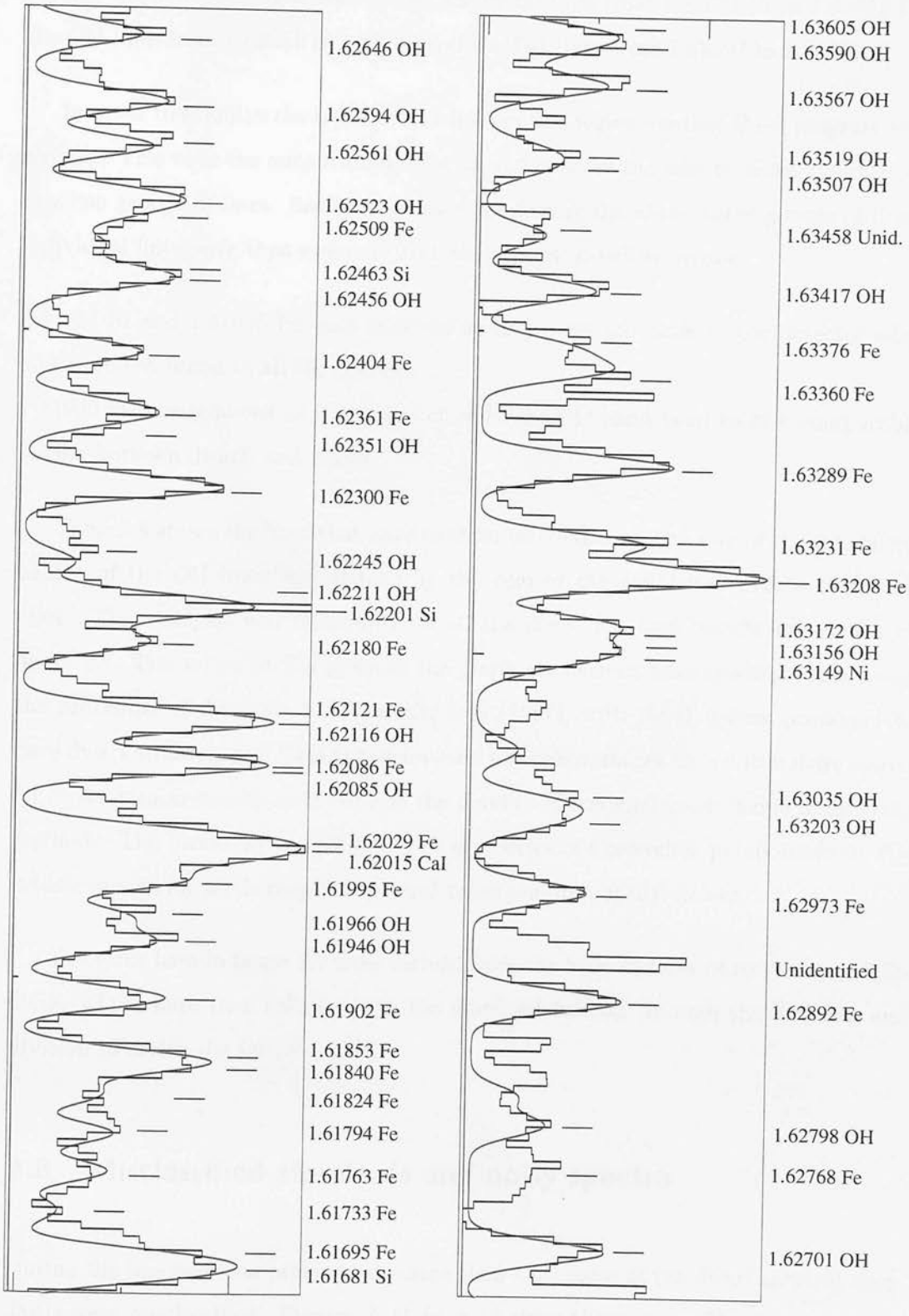

Figure 2.5: The lines found in a typical spectrum, all figures in microns.

regions which satisfy these conditions: the metal lines from 1.61681 Si to 1.61902 Fe, the OH lines from 1.62561 to 1.62701 and the OH lines from 1.63507 to 1.63605.

In order to examine the trends of the lines in this region another C++ program was written. This took the output from REDCGS and enabled the user to select the ratio of any two groups of lines. Ratios were calculated using the above three groups of lines, individual lines were then removed from the groups to reduce errors:

1.61681 Si and 1.61695 Fe were removed as they were too close to the detector edge and were not found in all the spectra.
1.61902 Fe was removed as it was too close to the CO band head to give comparable results between dwarfs and giants.

Table 2.6 shows the lines that were used for calculations. The sum of the equivalent widths of the OH lines was divided by the sum of the equivalent widths of the Fe lines. This analysis was performed on all the stars, the final results are shown in figure 2.7. The values of T_{eff} given in the graph are derived from spectral types using the procedure of de Jager & Nieuwenhuijzen (1987), with the T Tauris presumed to have dwarf atmospheres. This approximation was taken, rather than a literature search for direct measurements, as it reduced the number of systematic errors due to differing methods. The procedure is based on a fit of a series of Chebychev polynomials to T_{eff} measurements for a full range of spectral types and luminosity classes.

The error bars in figure 2.7 were derived from the least squares fit routine in REDCGS, which were then calculated in the standard fashion through the addition and division to derive the OH/Fe value.

2.8 Misclassified standards and noisy spectra

During the line selection process it became clear that some of the dwarf spectral standards were misclassified. Figures A.11 to A.13 show these stars. When the stars in the first two figures are compared with the correct standards in Appendix A it is clear

Fe	OH
1.61733	1.62561
1.61763	1.62594
1.61794	1.62646
1.61824	1.62701
1.61840	1.63507
1.61853	1.63519
	1.63567
	1.63590
	1.63605

Table 2.6: The lines used for the OH/Fe calculations

that they are Giant rather than Dwarf stars, the two most notable features being the large CO bandhead around 1.62μm and the increased depth of all the lines compared to the dwarfs. Of these, 2 stars, GL 459.2 and GL484.1, had already been reclassified as Giants by Xu (1991). This paper also classified GL454.3 as being a Giant, see figure A.13, which does contain the CO bandhead, although it is weaker than in the previous stars. It was decided to remove these stars from the analysis as well as BS7578, a spectroscopic binary, and GL 459.3 which did not appear to fit either the dwarf of giant classification, see figure A.13. Note the excess absorption in the region of the 1.620 Ca I and 1.6336 Fe lines.

It was also found that some of the T Tauris were too faint to give a good signal to noise ratio. These were LKHα 188, ROXs 39 and LKHα 172. It was also found that the observations of ROXs 44 had failed and contained no data. These stars were also removed from the analysis.

2.9 Interpretation of the OH/Fe data

If the giants and dwarfs in figure 2.7 are considered, it is clear that this technique is sensitive to 2 different parameters. The OH/Fe ratio decreases with temperature, as

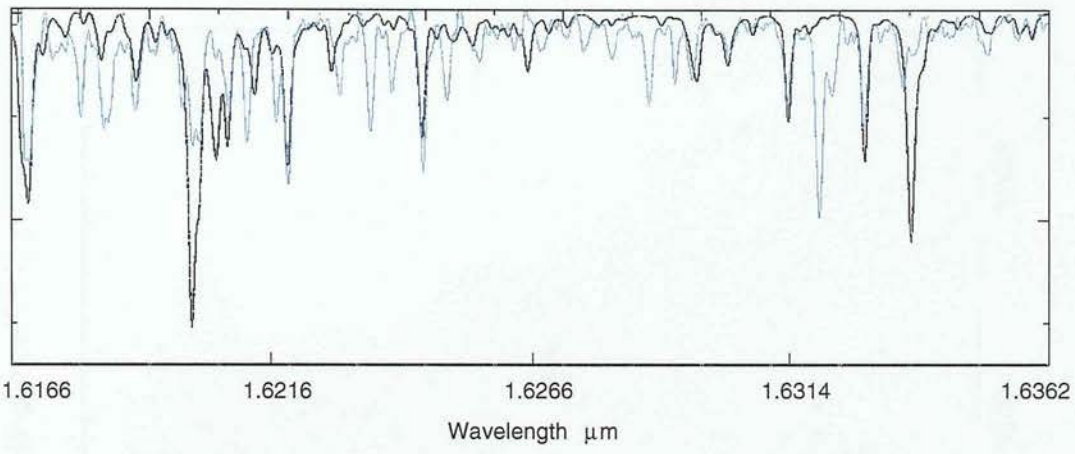

Figure 2.6: A comparison of a G4V star (blue) with a 5400 K log g=5.0 synthetic spectrum

the OH approaches dissociation. At the cooler end, the ratio also changes with surface gravity, this is shown in the separation of log g values in figure 2.8. The turn over around 3400 K is a result of line saturation in the OH lines.

To check these were the only parameters to which the OH/Fe ratio is sensitive, synthetic spectra were analysed in the same way as the observations. The NextGen models of Hauschildt, Allard & Baron (1999) were used. Previous versions had already been tested in the near-I.R. by Jones et al (1996). Figure 2.6 shows a comparison of a synthetic spectrum with a comparable dwarf star. Several lines are missing from the synthetic spectra, most obviously 1.63208 and 1.63231 Fe, and also 1.61794 Fe. This means that a direct comparison with observations cannot be made, but it is possible to perform a similar analysis to that of the observations.

The synthetic spectra were first convolved with a gaussian to give them a similar profile and width to that of the observations. They were then read into REDCGS and treated in the same manner as the observations. An OH/Fe figure was then derived, again using the lines listed in table 2.6. The errors are larger for the synthetic spectra as they do not contain all of these lines. The results can be seen in figure 2.8.

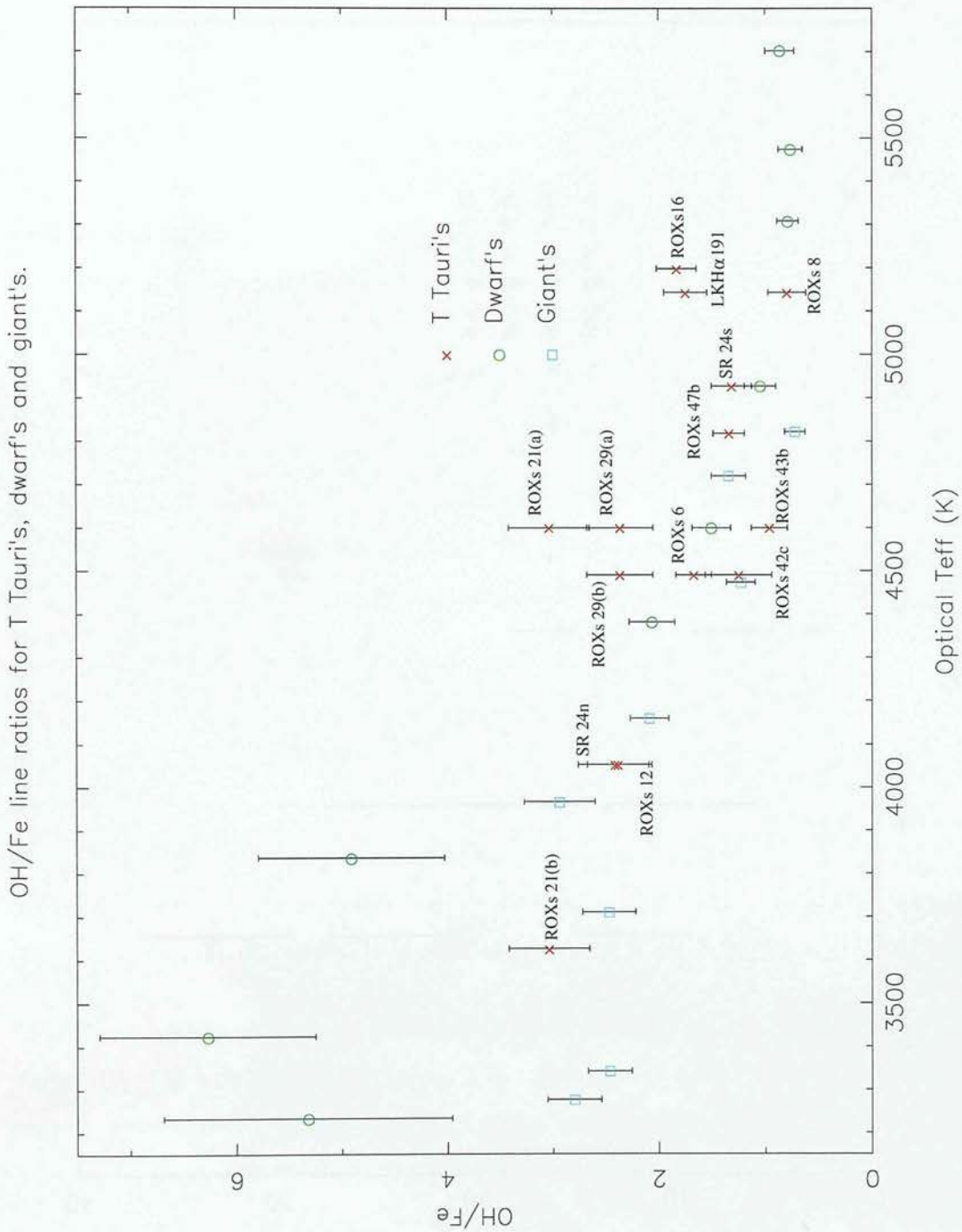

Figure 2.7: OH/Fe line ratios for T Tauris, dwarfs and giants. ROXs 21 and 29 are shown at both the hottest (a) and coolest (b) temperatures found by BA.

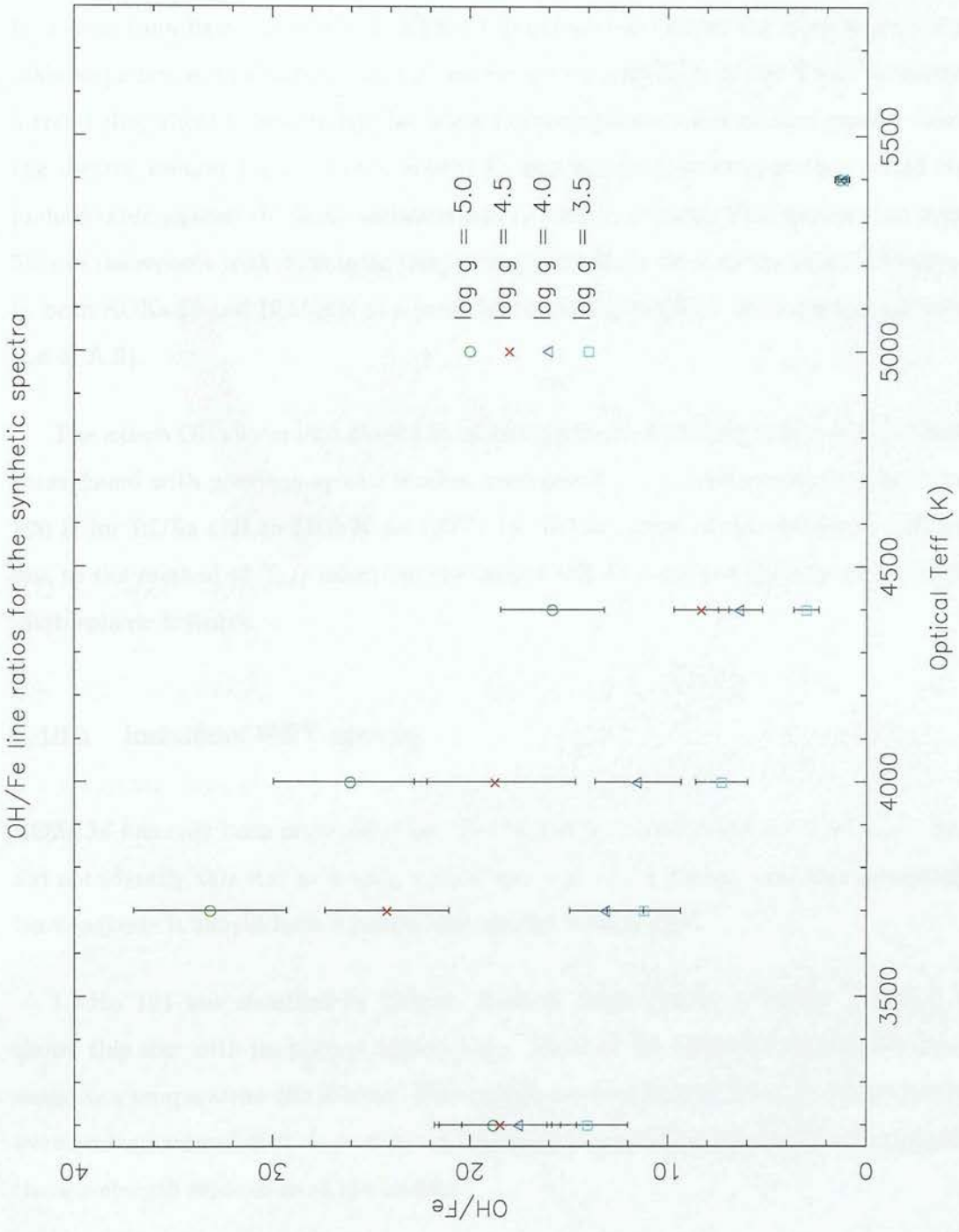

Figure 2.8: OH/Fe line ratios for the synthetic spectra.

2.10 Results for the T Tauris

It is clear from figure 2.7 that the TTSs observed do not behave the same way as the main sequence stars observed. In the section above 4500 K, 5 of the TTSs lie above a trend they should theoretically be below (as they have a lower surface gravity than the dwarfs, section 1.2.2). Below ≈4000 K, any variation in temperature would be undetectable against the large variation due to surface gravity. This means that over 50% of the sample with detectable temperature variations show excess OH absorption. In both ROXs 29 and 16 this is at a level that is clearly visible in their spectra (figures A.8 & A.9).

The excess OH shows that these I.R. observations are detecting cooler regions than those found with previous optical studies, with possible T_{eff} differences varying from 100 K for ROXs 47B to 1100 K for ROXs 16. Whilst some of this difference will be due to the method of T_{eff} selection, the largest OH excesses can only be due to cool photospheric features.

2.10.1 Individual MST spectra

ROXs 16 has only been previously classified by BA, as a G9 optical spectral type. BA did not identify this star as having a MST spectrum, even though the data presented here suggests it should have a component around 4400 K (K7).

LKHα 191 was classified by Valenti, Basri & Johns (1993) as K0/3. Figure 2.7 shows this star with its hottest optical T_{eff}. Even at K3 (4800 K) the OH/Fe data suggests a temperature 400 K lower. The spectra used by Valenti, Basri & Johns (1993) were centred around 4000 Å, so it is not suprising to see such a large MST effect, given the wavelength separation of the studies.

ROXs 29 has been comparatively well observed, although its classification has varied from K3 (Padgett 1996) to K7 (Cohen & Kuhi 1979). This data implies an even lower temperature as it has an OH/Fe value similar to that of SR 24n and ROXs 12, both of

which are M0 stars.

ROXs 21 has only been previously classified by BA. It was found to be a MST star with feature varying from K4 to M2. The OH/Fe results suggest a temperature <3900 K, lying in the region where surface gravity effects become dominant. This result agrees with the M2 features found by BA.

SR 24s lies just above the expected position of a K2 star when compared with the trend of the dwarfs. This apparent MST result is most likely caused by the use of spectral types to find optical temperatures, which implies very coarse sampling. As this star has been observed with K2 spectral type from the optical to the mid-I.R. (Greene & Meyer 1995) it is probable that the temperature difference suggested in figure 2.7 is just an error in the exact T_{eff} chosen for K2.

2.11 Conclusion

This near-I.R. data has shown that MST stars can be found by comparing high quality I.R. data with optical studies. Figure 2.8 shows that it is important to understand the behaviour of spectral lines studied with both temperature and surface gravity. If the extent to which lines in cool stars are affected by surface gravity were ignored the temperatures calculated would be very inaccurate (e.g. ROXs 24(b) in figure 2.7 would be 400 K hotter if it were assumed to have a dwarf-like atmosphere). The technique used in this study is very good at finding MST stars with optical temperatures >4500 K, and has shown that 50% of the TTSs above this display the MST effect, with 2 newly discovered MST stars, LKHα 191 and ROXs 16.

The statistics on the frequency of the MST effect are only slightly improved by this study. Only 8 of the objects are in the region where MST spectra are observable, of these 4 have higher than expected OH/Fe values. The 50% detection rate is much higher than that found in BA, but the small number statistics and the inclusion of objects with known MST phenomena make this study exploatory rather than conclusive. The figures do suggest that the 11% detection rate of BA and the 100% detection rate of

GHBC are not irreconcilable.

Chapter 3

The optical MST effect and the variability of T Tauri stars.

3.1 The need for variability data.

The current observations of MST stars, through the studies of BA, GHBC and Chapter 2, do not contain any information on the variability of MST features. BA only show that the non-MST features of their sample have no variation on the order of days. The detection of variation in MST features would help in understanding the nature of the phenomenon. For example, if they are due to a multiple system, variation would only be seen on the scale of the orbital periods. They could be due to unusual accretion processes, where the MST features would be seen as a single event. The effect could be on the stellar surface, where an uneven distribution of features would lead to rotional modulation of the spectra on a timescale of days. It is vital to accurately model the MST features as otherwise the stars cannot be placed accurately on the H-R diagram, observational techniques cannot be campared and the structure of TTSs will not be fully understood.

Optical data would also allow direct comparison with the spectra presented in BA, showing if the spectra have varied over a period of years, as well as looking for day to

day variations.

3.2 The choice of instrument.

As MST phenomena have been found spectrally in many TTSs (BA, Chapter 2), any temporal study would have to include a large number of stars in order to maximise the chance of detection. As TTSs have a typical V magnitude of >12, the integration time on a smaller telescope would mean that only a few objects could be observed in one night. This meant that a multi-object spectrometer was the only way to study the same objects on every night of an observing run. After taking into consideration regions previously studied for these MST spectra, the requirements of field of view and of separation between individual objects for multi-object spectrometry, it was decided to use the FLAIR system on the UK Schmidt telescope at Coonabarabran in Australia to observe the ρ Ophiuchus region.

3.3 The UK Schmidt telescope and FLAIR spectrometer.

The UK Schmidt telescope (UKST) consists of a 1.83 m mirror with a 1.24 m aperture corrective lens. It has a 6.4° field of view and a plate scale of 67.12 arcsec/mm. The FLAIR system sits in the primary focus, in the plate holder normally used for photographic plates. A FLAIR plateholder has about 100 100 μm optical fibres that are terminated in prisms (ferrules) that direct light falling on them into the fibres. The fibres are taken out of the telescope tube in a bundle and are fed into an optical bench containing the spectrograph. The physical size of the ferrule means that only stars that are >2 arcmin apart can be observed. Due to light leakage between the fibres, only half the fibres can be used when observing objects of differing magnitudes, and 6 fibres are reserved for running the system, one for a guide star and 5 fiducial fibres used to align the plateholder with the field. These constraints meant that only 40 objects were observed in the field.

In order to correctly position the ferrules on the plate a film copy of a UKST photographic plate is placed in the bottom of the plateholder and the ferrules are glued on top. To obviate the need for a special photographic run, a plate taken in a sky survey is used. Fortunately, UKST field 517, which is centred at 16° 30', -25° (1950), contains most of the ρ Ophiuchus TTSs. For a more detailed description of the FLAIR system see Parker & Watson (1995).

3.4 The choice of stars

The nature of the FLAIR system placed several restrictions on the choice of stars. Not only were there separation constraints, but all the stars had to be contained within the field and the support staff regarded the limiting magnitude of the system as being V<16 for stellar observations, although no direct testing had been done to enable a clear signal to noise cut-off.

T Tauris were chosen within these constraints to give a broad range of spectral types and a selection of CTTSs and WTTSs. Preference was given to stars that had been observed with MST features. Eleven standards were observed with a range in spectral types similar to that of the T Tauris, they were both dwarfs and giants. These were observed to enable similar analysis to that performed on the UKIRT data. Their selection did not limit the number of TTSs observed as this was limited by the instrumental constraints. Tables 3.1 and 3.2 list the observed stars. Blanks indicate unknown stellar properties.

The positions of the TTSs selected are shown in figure 3.1, the positions are overlaid on the 100 μm map of the region. This shows that all the stars observed are visually associated with the ρ Ophiuchus cloud, as seen in the dust emission detected by IRAS. Figure 3.2 shows a UKST plate of the field. This clearly shows the nebulae and dark clouds associated with the star forming region. The regions of bright emission in the 100 μm map are seen as the areas of greatest nebulosity (bright or dark) in the optical.

Object	Sp. Type	R.A.	Dec	V
HD 150968	G5V	16:45:24.0	-25:22:07	9.5
HD 149826	G3V	16:38:06.2	-22:26:34	9.3
SAO 184463	B7V	16:34:03.3	-26:30:19	9.93
HD 148212	G2V	16:27:31.6	-25:08:59	9.62
CoD 24 12677	M2V	16:23:01.2	-24:41:46	10.25
VSS II-135	G8V	16:20:57.9	-23:52:34	10.35
HD 150470	K1III	16:42:01.7	-24:48:55	8.7
HD 150383	M5III	16:41:49.7	-27:06:18	8.6
BD 22 4175	K5III	16:34:34.5	-22:36:40	9.2
HD 148369	K4III	16:28:27.5	-26:40:37	9.43
SAO 184604	M0	16:41:58.3	-23:06:16	9.3
CoD 24 12753	K0	16:39:53.9	-25:04:48	9.5

Table 3.1: The standard stars observed with FLAIR

Object	Sp. Type	R.A.	Dec	V	Hα EW Å	new Hα EW Å
WSB 77	M1	16:32:21.9	-24:42:14			55
ROXs 47A	K8,M0	16:32:11.9	-24:40:17	13.3	9.2	9.7
ROXs 45E	K7	16:31:44.9	-25:30:28	13.7		-5
ROXs 44	K3	16:31:33.4	-24:27:33	12.5	68	69
ROXs 43B	K6	16:31:19.8	-24:30:04	11.4	0.8	0.7
HBC 644	K3	16:31:05.2	-24:04:37	12.3		2
ROXs 40	K6	16:30:51.3	-24:11:32		-1.2	-1.9
ROXs 39	K5,7	16:30:35.5	-24:34:15		4.8	3.4
ROXs 38A	K2	16:30:15.5	-25:35:36		-1.5	-1.1
ROXs 35B	G5	16:29:34.4	-24:52:24	10.6	-2.0	-1.9
ROXs 35A	K3	16:29:33.7	-24:55:29	12.6	-1.0	-1.5n
ROXs 34	K	16:28:45.3	-24:28:17	13.5	39	72
SR 15		16:28:10.2	-24:16:00	13.6		-8
HBC 265	M2	16:27:55.4	-24:26:17	14.0		98n
ROXs 29	K3.5,7	16:27:40.2	-24:22:03	11.3	12	13
ROXs 30C	K4	16:27:38.8	-23:58:19	15.0	14.3	19n
ROXs 21	M2	16:27:19.4	-24:41:38	13.1	6.7	4.2
SR 24N		16:26:58.2	-24:45:30	11.6		-1.5n
HBC 261	K5	16:26:47.6	-23:14:55	13.8		38
ROXs 9C	K4	16:26:37.8	-25:45:13		-1.0	-1.4n
WSB 28		16:26:20.8	-24:08:51			n
ROXs 8	K	16:26:03.0	-24:23:35	13.8	-0.6	n
ROXs 6	K5	16:25:56.1	-24:20:47	13.6	154	95
ROXs 5	K7	16:25:55.6	-23:55:09		1.4	1.7n
ROXs 3	M1	16:25:49.6	-24:51:30		2.5	2.2
WSB 22		16:25:17.1	-25:11:04			n
HBC 257	K6	16:25:10.6	-25:19:15	13.4	50	68
HBC 256	K6	16:21:34.8	-26:12:24	13.3		130

Table 3.2: The young stars observed with FLAIR. Hα EW, previous Hα equivalent width measurement (BA or Herbig & Bell 1988). New Hα EW, Hα equivalent width as measured in FLAIR data (positive in emission), n indicates noisy spectra.

Figure 3.1: The positions of the observed TTSs overlaid on the 100μm IRAS map of UKST field 517.

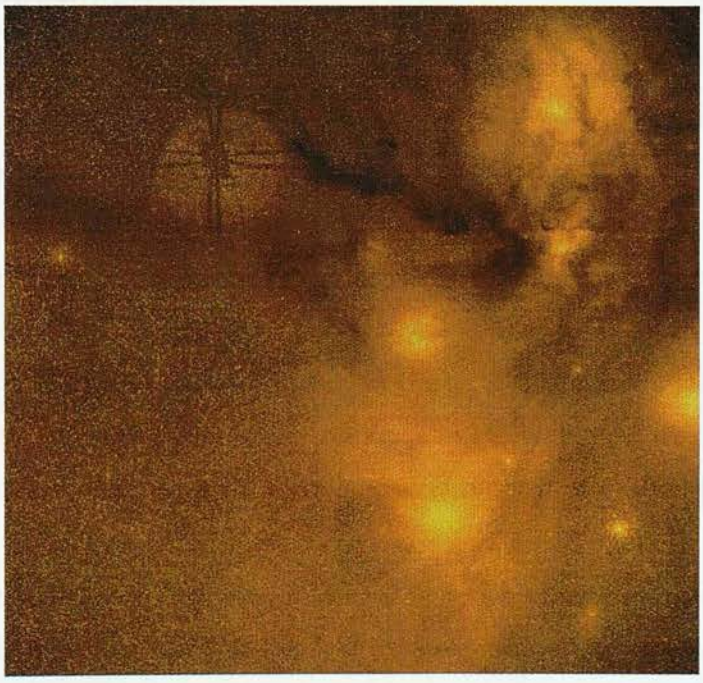

Figure 3.2: An optical image of UKST field 517.

3.5 The spectral regions observed

In order to detect subtle spectral peculiarities, the largest possible range in wavelength had to be observed. As seen in section 2.2, it was also necessary to observe at high resolution in order to be able to select individual temperature sensitive lines. B, V and R gratings were used to study the useful range of the system (3800 to 9000 Å), see table 3.4 for the ranges of the spectra taken.

The first B grating region was the most difficult to obtain. This was taken at the limit of the instrumental range and could not accurately be selected, giving an ≈100 Å change in the start position between observations. The resolution of the R grating spectra could be less, as the main lines under observation in this region are TiO bands, which are a few 100 Å wide. During the 6 hours of observations possible each night, 3 hours were spent observing the field, the other 3 were required for flats, arc observations and overheads.

3.6 The observations.

The project was given 6 consecutive half nights of observations in August 1998. Unfortunately the second and forth nights were lost to cloud. Cloud also interrupted the observations on nights 1, 3 and 5; these delays caused problems for a temporal study. The other problem that was discovered during the observations was the pointing method of the FLAIR system. As mentioned in section 3.3, the telescope is pointed using a single guide star, normally placed centrally in the field. The fiducial stars (section 3.3) are then used to rotate the plateholder until it is correctly aligned with the field in the sky. This is checked using a monitor in the control room which shows the output from the 5 fiducial fibres. As these fibres have slightly different errors in their positions, and differing transmission efficiency, it is near impossible to find a position where the light from each fibre is equal. This requires the judgement of the telescope operator to find the 'best' position, leading to subtle differences in the position of the plateholder between observations. As the object fibres also have slight errors in their positioning,

Night	Grating	Time (s)	Exposures	Comments
1	1200B	3000	4	Some cloud
	1200B	900	2	Lost guiding
	1200V	1800	3	
	600R	1000	2	
	600R	450	3	
3	1200B	2400	4	
	1200B	1800	3	Some cloud
	1200V	1800	3	Some cloud
	600R	900	3	
	600R	750	3	
5	1200B	4500	5	Some cloud
	1200B	2700	3	
	1200V	1800	2	
	600R	900	3	
	600R	450	3	
6	1200B	4500	5	Clear night
	1200B	3600	4	
	1200V	1800	2	
	600R	900	3	Dome not tracking
	600R	450	3	

Table 3.3: Journal of observations for the FLAIR data, night 1 is August 14-15th 1998. The same FLAIR plate was used for all observations. See table 3.4 for wavelengths observed.

Grating	Name	Start Å	End Å	Resolution Å
1200B	B1	3779	4535	2.37
1200B	B2	4538	5282	2.09
1200V	V	5235	5978	1.92
600R	R1	5861	7314	3.81
600R	R2	7366	8863	4.38

Table 3.4: The wavelength regions observed with FLAIR, the resolution is determined from the FWHM of arc lines. The name is that used in the rest of this thesis.

this added systematic error means that the fibres which are most accurately aligned to the sky differ from night to night. The result is that each object fibre samples a different part of each stellar PSF on each night, giving different flux levels. Again this is not desirable in a temporal study.

For the nights that were partly interrupted by cloud, the observing runs were altered to keep the range in wavelength. This meant that less time was given for the 1200V filter.

3.7 Data reduction.

The data reduction follows the normal procedure for FLAIR data as described in Drinkwater & Holman 1996. The first stage is to convert all the frames. The FITS frames produced by the FLAIR system are not compatible with the standard FITS files, and so must be converted using the **fixhead** IRAF routine supplied by the AAO.

The bias and flat field frames are then combined using the **zerocombine** and **flatcombine** commands. At this stage the only processing performed on the frames is using average sigma clipping to reject bad pixels.

The **ccdproc** command is then used to perform all the necessary reduction on the full frames. This applies bias correction, using both the bias frames and an overscan

region on the chip, removes the overscan regions from all the frames and can correct for any known bad pixels. After this similar files can be combined using the functions **imarith** or **combine**. These can be either arc frames which cover the same wavelength region, or repeated observation frames.

The final stage of reduction uses the task **dofibers**. This routine performs all the necessary steps to extract the spectra form the observation frames. It starts by comparing the flat field with a list of fibre apertures that specifies if that fibre is on an object, sky or is to be ignored. This enables interactive identification of the positions of all the spectra in the frames. The spectra from the flat field are then extracted and used to correct for the throughput differences between fibres.

Wavelength calibration is then done using a specified arc frame. A list of known lines is compared with a spectrum extracted from the frame, with interactive control over which lines are selected for the wavelength calibration. **dofibers** then identifies these lines in all the spectra on the frame and applies an individual dispersion correction to each aperture. Sky subtraction is then performed on the frames using the spectra specified in the aperture list. Finally **dofibers** extracts each object spectrum as a 1-dimensional data set.

Additionally, for this data set, care was taken to select the best frames for each set of observations as several had high noise levels due to the problems described in section 3.6.

3.8 The FLAIR spectra.

If the MST spectra observed by BA were caused by the presence of two different temperature regions on the same star, the spectral region most likely to show variation would be the blue. The model requires the red region displays mainly cool photosphere features, whereas the blue region will be affected by the small warmer regions. See Section 4.3 for further discussion.

Time constraints on this project have not allowed for a full reduction to be performed, i.e. fitting model atmospheres and emission spectra. Instead the lines chosen by BA to be the most important were examined in detail.

The first set of lines presented are of the B1 observations, figures 3.3 and 3.4. The spectra are combined from the 5th and 6th nights of observation, as these had the highest s/n ratio. The G band is seen to decrease with later spectral type in most of the stars (within an error of ± 1 sub class, due to the noise in the spectra). Conversely, tha Ca I line increases with later spectral type, seen in extreme in the cool star SR 24N. Two spectra are presented for ROXs 3, from the 5th and 6th nights. Comparison of these spectra suggests that some variation has taken place, particularly around the Ca I line and the G band.

To investigate this variation difference spectra were constructed from the two nights B1 observations. Initially the spectra from night 5 were divided by their conterparts from night 6. The resulting ratio spectra were fitted with a 3rd order polynomial which was then multiplied with the night 6 data. This placed the 2 nights data onto the same flux scale. The calibrated night 6 data was then subtracted from the night 5 spectra. The difference spectra for 5 stars are shown in figure 3.5.

The 3 stars marked with red crosses in figure 3.5 had too low a signal to noise ratio to be included with the other results, but are shown here as they have clear variability in their emission lines. The variable emission lines, Ca II H & K, Hϵ, Hδ and Hγ, are commonly seen in TTSs. All 3 of these stars have large Hα emission (> 70 Å EW) and are therefore classified as CTTSs, it is highly likely that these emission lines are related to accretion processes. See Appendix B for a discussion of CTTS accretion.

The other two stars, ROXs 3 and 21, both have low Hα emission, 2.2 and 4.2 Å EW respectively. This classifies the stars as WTTSs, and so it cannot be assumed that the variability is the result of accretion. ROXs 3 shows probable variation in 3 emission lines, the Ca II/Hϵ blend, Si IV and Hγ, all these lines were stronger on night 5. Hϵ and Hγ are associated with active chromophere emission. Si IV is an ion associated with the transition region and chromosphere. It is seen to some extent in most of the observed

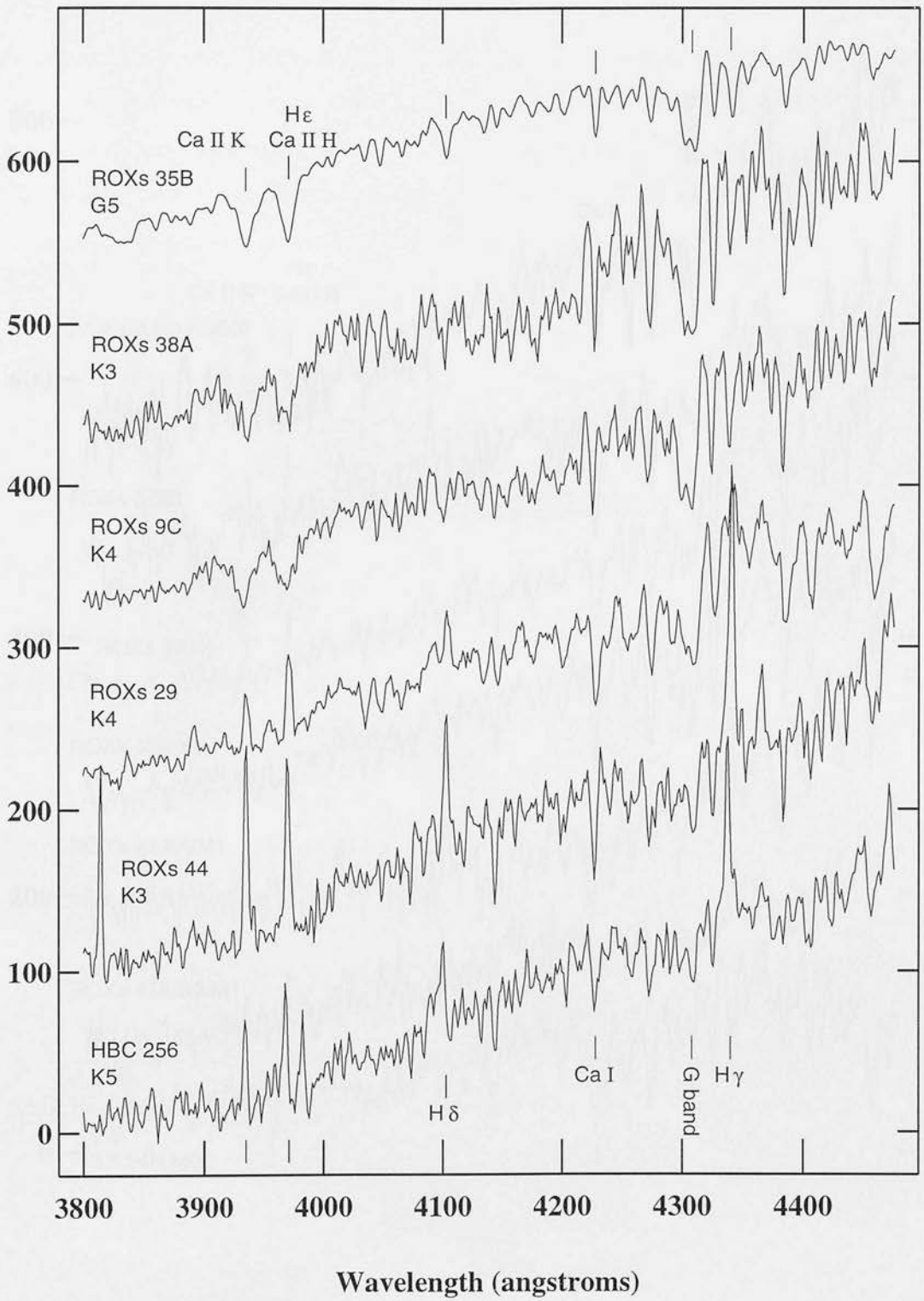

Figure 3.3: T Tauri spectra from the B1 observations. The spectra have been scaled and shifted for clarity.

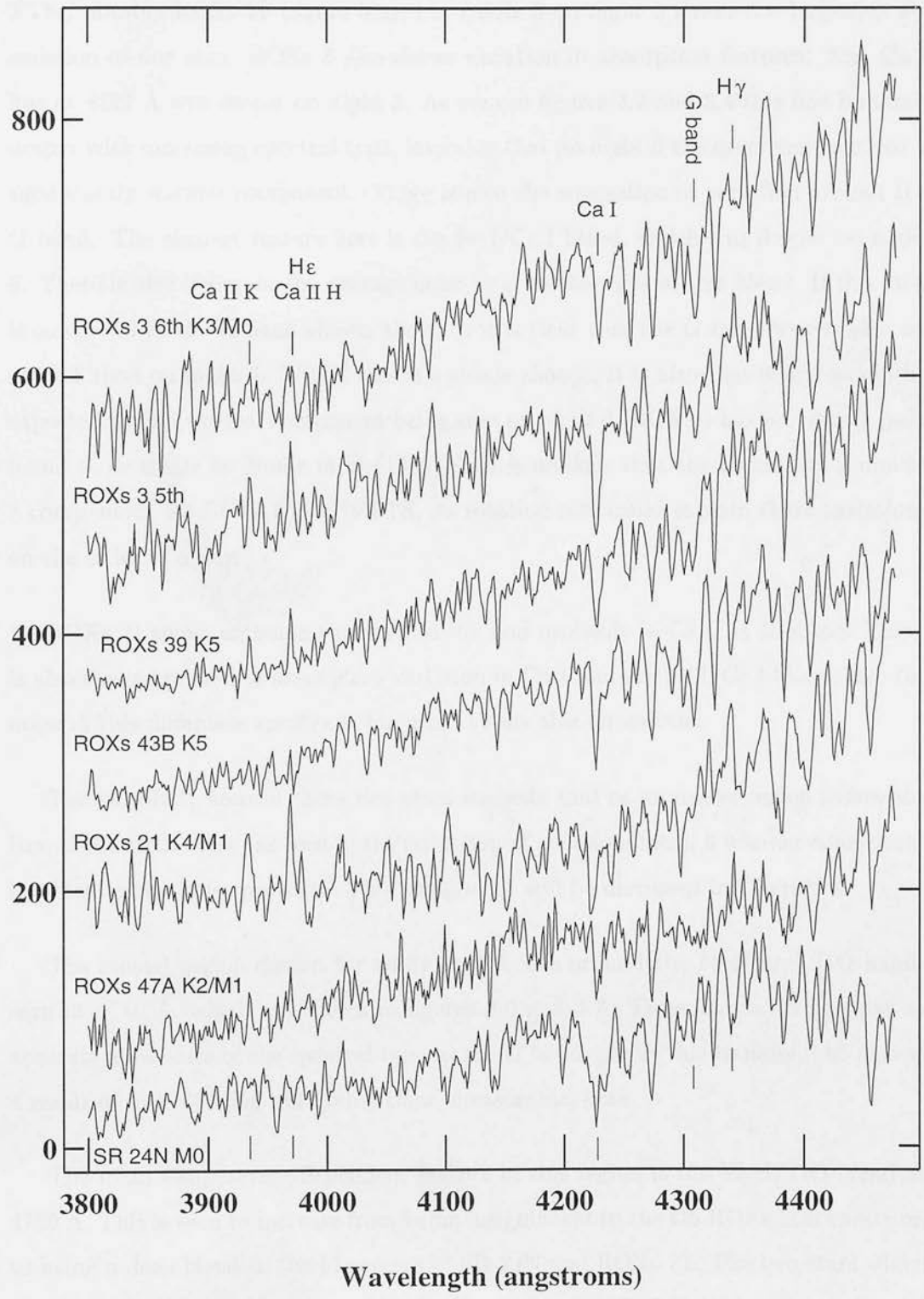

Figure 3.4: T Tauri spectra from the B1 observations. The spectra have been scaled and shifted for clarity.

TTSs, notably ROXs 29 (figure 3.3), but ROXs 3 on night 5 shows the largest Si IV emission of any star. ROXs 3 also shows variation in absorption features. The Ca I line at 4227 Å was deeper on night 5. As seen in figures 3.3 and 3.4 this line becomes deeper with increasing spectral type, implying that on night 6 the spectrum contains a significantly warmer component. There is also the suggestion of variation around the G band. The clearest feature here is the Fe I/Cr I blend, which was deeper on night 6. There is also a step in the average noise level to the right of this blend. If this step is compared to the G band shown above it, it is clear that the G band was weaker on night 5 than on night 6. Whilst this is a subtle change, it is also that which would be expected from a warmer component being seen on night 6. ROXs 3 has previously been found to be single by Simon et al. (1995) So it is unlikely that the variability is due to a companion. As ROXs 3 is a WTTS, its rotation rate could explain these variations on the order of a day.

ROXs 21 shows emission variation in Hδ, and probably in Ca II H & K too. There is also the suggestion of absorption variation in Ca I and the Fe I/Cr I blend, but the noise in this difference spectra is too great to say this for certain.

The variabilty seen in these two stars suggests that as an active region leaves the face of the stellar disc (as seen in the reduction of emission lines), a warmer component is added to the blue spectrum. This component will be discussed in Chapter 4.

The second region chosen for study by BA was around the MgH and TiO bands seen at 4780 Å, which are shown in figures 3.6 and 3.7. These bands do not give as accurate a measure of the spectral type as the G band, partly due to noise, but also as a result of line blending not giving clear, measurable, lines.

The main temperature dependent feature in this region is the MgH/TiO blend at 4780 Å. This is seen to increase from being insignificant in the G5 ROXs 35B spectrum to being a deep blend in the M spectra of SR 24N and ROXs 21. The two stars which are mis-placed in this sequence are ROXs 29, with the Mg/TiO blend being as dominant as in the K5 stars and ROXs 47A, with the blend being weaker than any other M star. Previously the spectral type of ROXs 29 has been measured as K3,4 (Padget 1996),

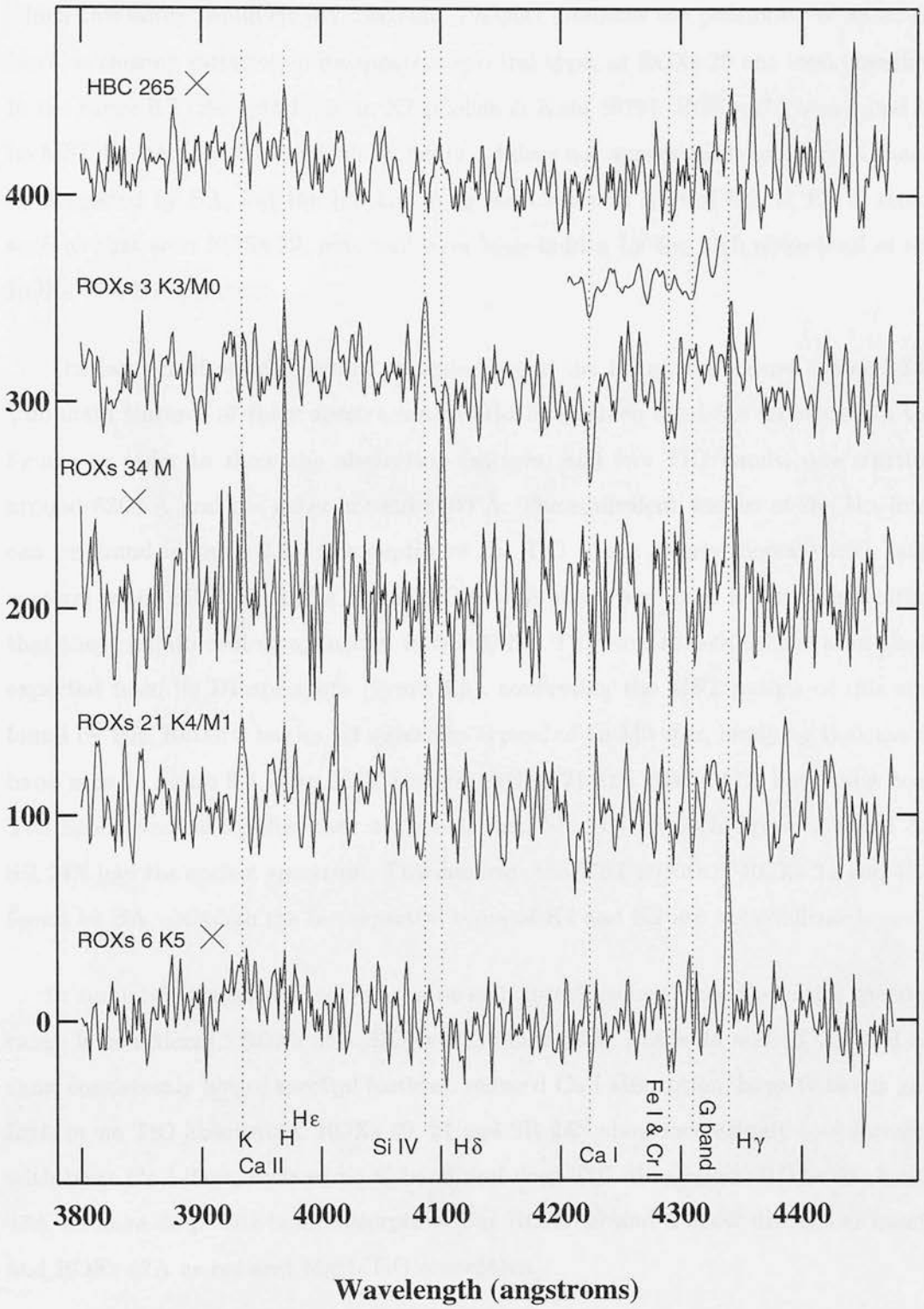

Figure 3.5: The difference spectra for the B1 filter based on the data from nights 5 and 6. The small spectrum between HBC 256 and ROXs 3 is part of the ROXs 29 spectrum from figure 3.3 and is included to show the shape of the G band. The spectra have been scaled and shifted for clarity.

which this study would clearly discount. Padgett discusses the possibility of spots on the star causing variation in its apparent spectral type, as ROXs 29 has been classified in the range K3 (Padgett 1996) to K7 (Cohen & Kuhi 1979). ROXs 47A was found to be MST by BA. The B1 spectrum in figure 3.4 does not appear to show a large G band as suggested by BA, but the B2 data suggests a spectral type of K5. A K5 G band, such as that seen ROXs 39, may well have been hidden by the high noise level of the ROXs 47A B1 spectrum.

The last set of optical spectra presented are of the R1 region, figures 3.8 and 3.9. The main features of these spectra are the Hα line, which has been truncated in the figures in order to show the absorption features, and two TiO bands, one starting around 6200 Å and the other around 6600 Å. The equivalent widths of the Hα lines can be found in table 3.2. The depths of the TiO bands clearly increase with later spectral type. SR 24N, ROXs 21 and ROXs 47A show very deep features, indicating that they contain cool components. ROXs 29 has TiO bands much deeper than those expected from its B1 spectrum (figure 3.3), confirming the MST nature of this star found by BA. ROXs 3 has an R1 spectrum typical of an M0 star, implying that the G band seen in figure 3.4 is an MST feature. ROXs 21 and ROXs 47A have very deep TiO bands, indicating that they are cooler than SR 24N, in both figures 3.4 and 3.7 SR 24N had the coolest spectrum. This confirms the MST nature of ROXs 21 and 47A found by BA, although the blue spectral types of K4 and K2 are not confirmed.

In summary, the stars observed can be split into 3 groups when the entire spectral range is considered. ROXs 35B, ROXs 9C, ROXs 38A, ROXs 44 and ROXs 43B all show consistently hotter spectral features, reduced Ca I absorption, large G bands and little or no TiO absorption. ROXs 39, 21 and SR 24N show increasingly cool features with large Ca I lines, little or no G band and deep TiO absorption. ROXs 29, 3 and 47A all have deep TiO band absorption, but ROXs 29 and 3 show distinct G bands and ROXs 47A as reduced MgH/TiO absorption.

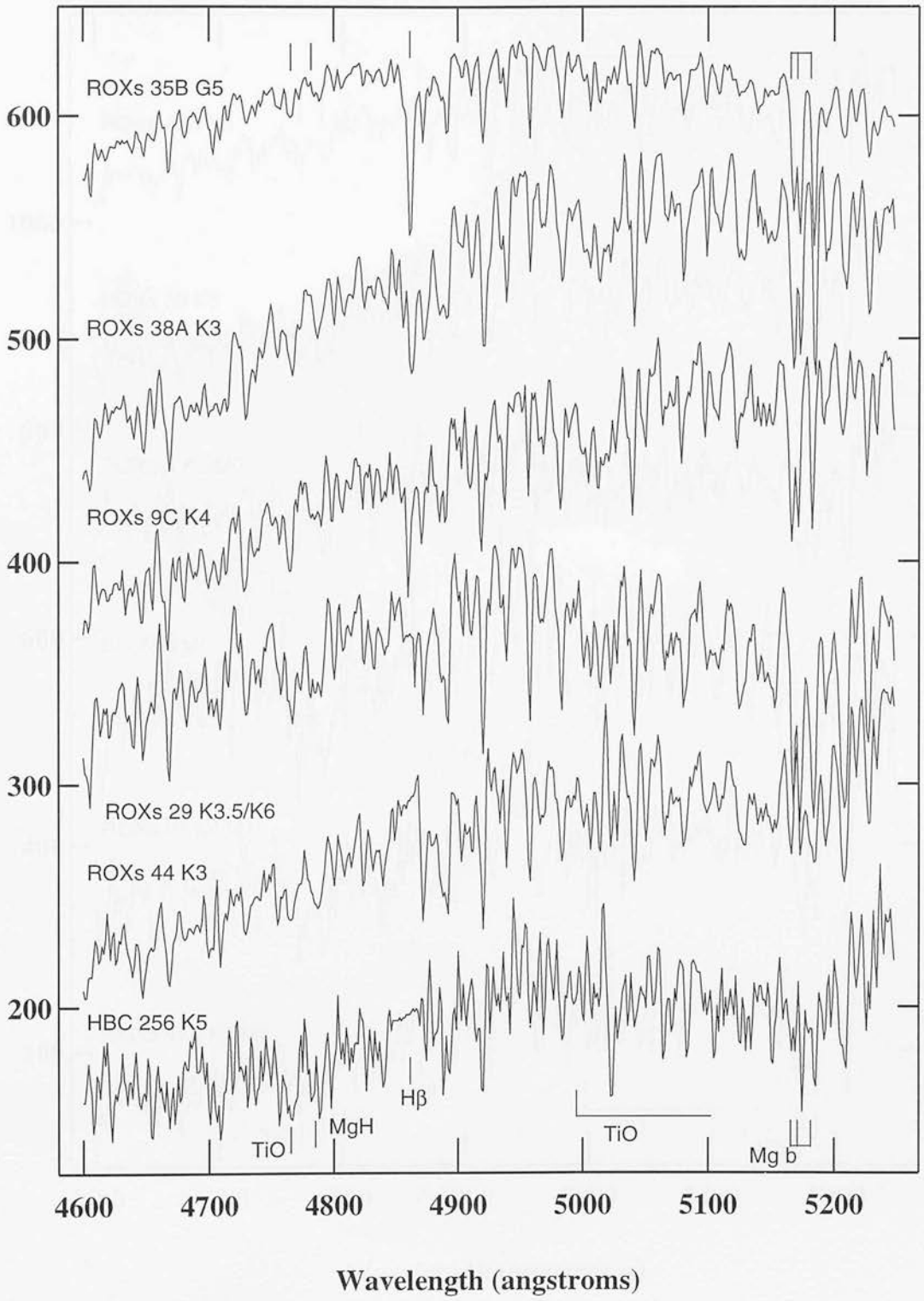

Figure 3.6: T Tauri spectra from the B2 observations. Note that the Hβ line has been truncated where in emission. The spectra have been scaled and shifted for clarity.

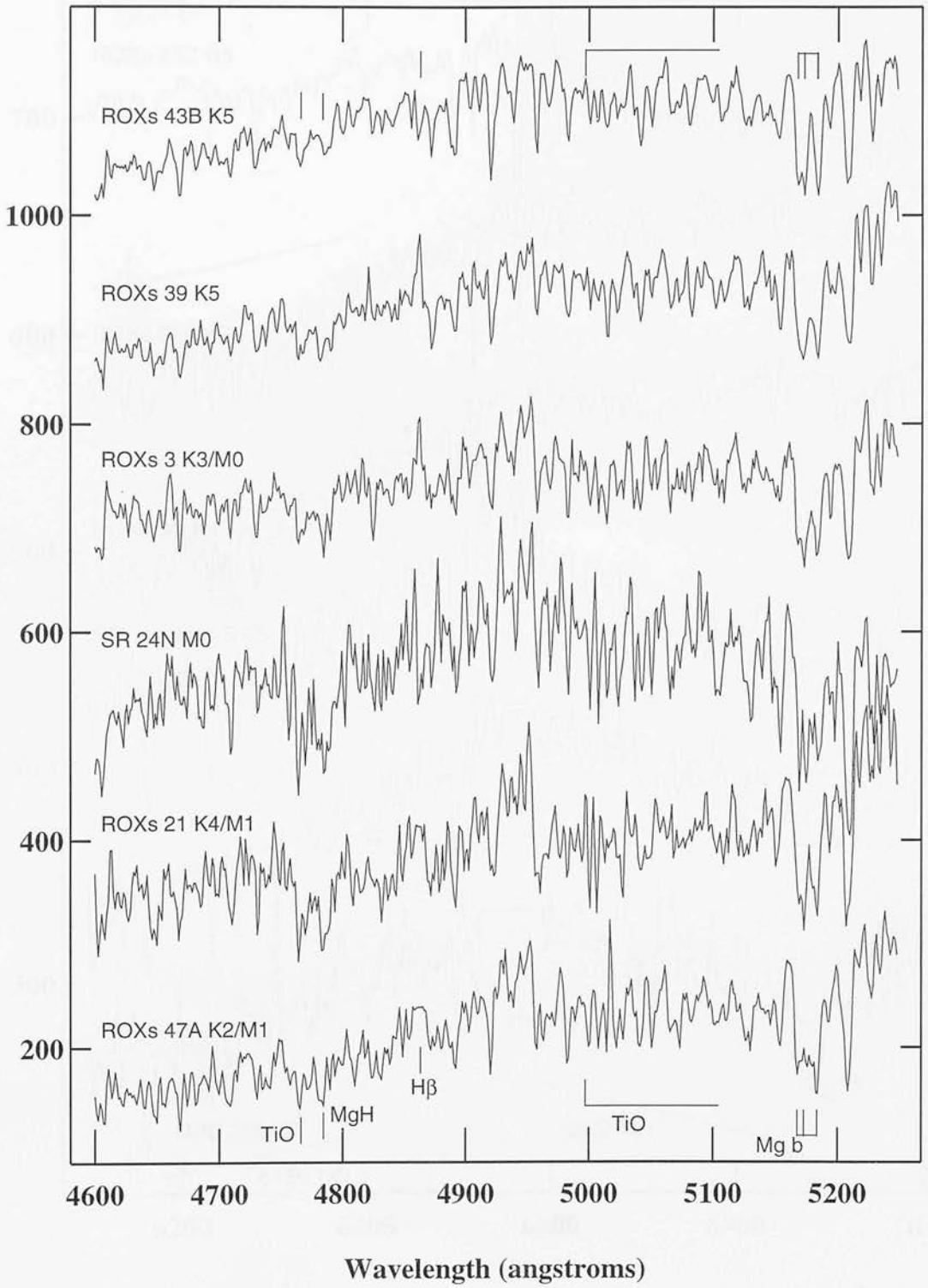

Figure 3.7: T Tauri spectra from the B2 observations. Note that the Hβ line has been truncated where in emission. The spectra have been scaled and shifted for clarity.

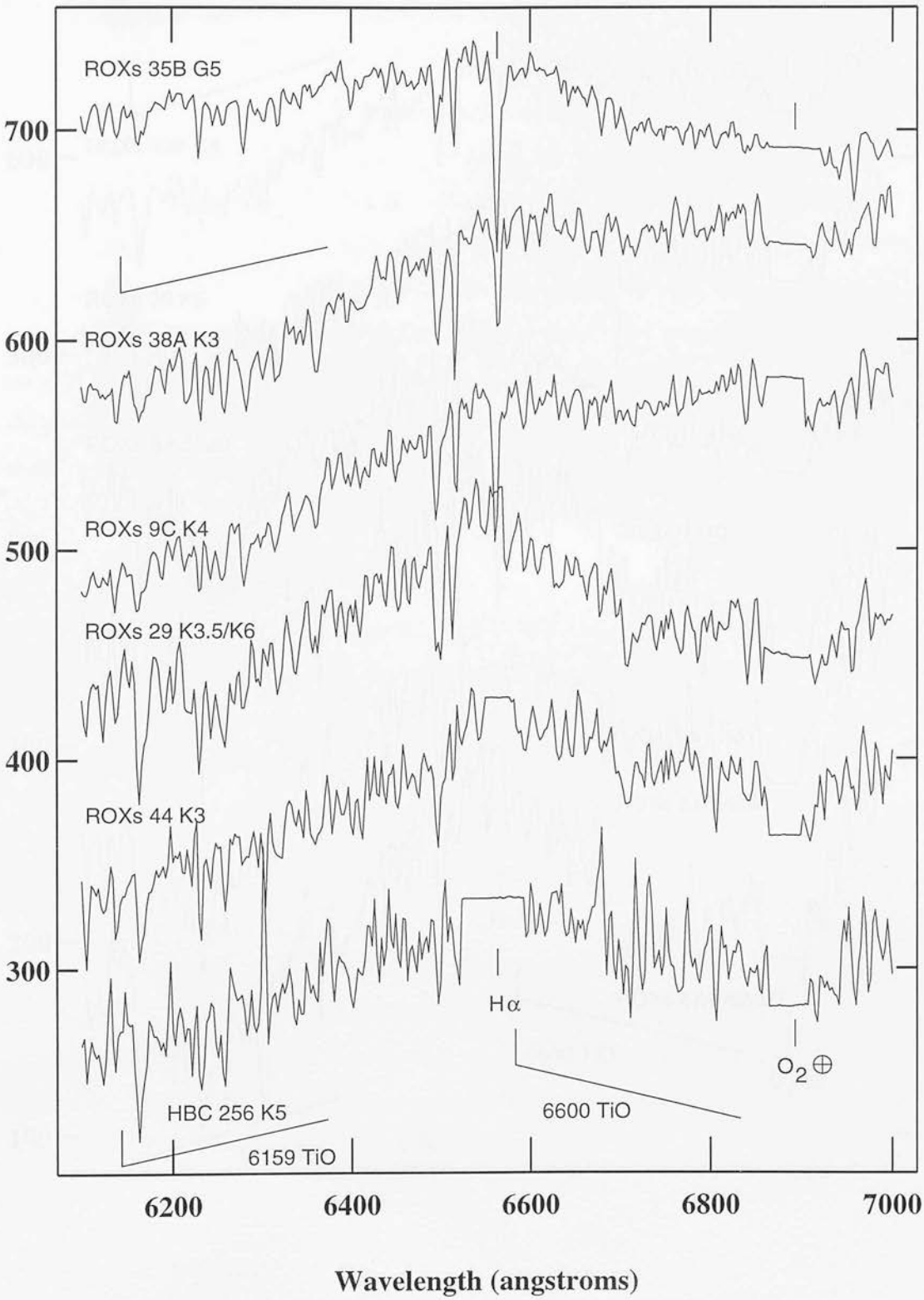

Figure 3.8: The first set of R1 spectra. Note that the Hα line has been truncated where in emission. The spectra have been scaled and shifted for clarity.

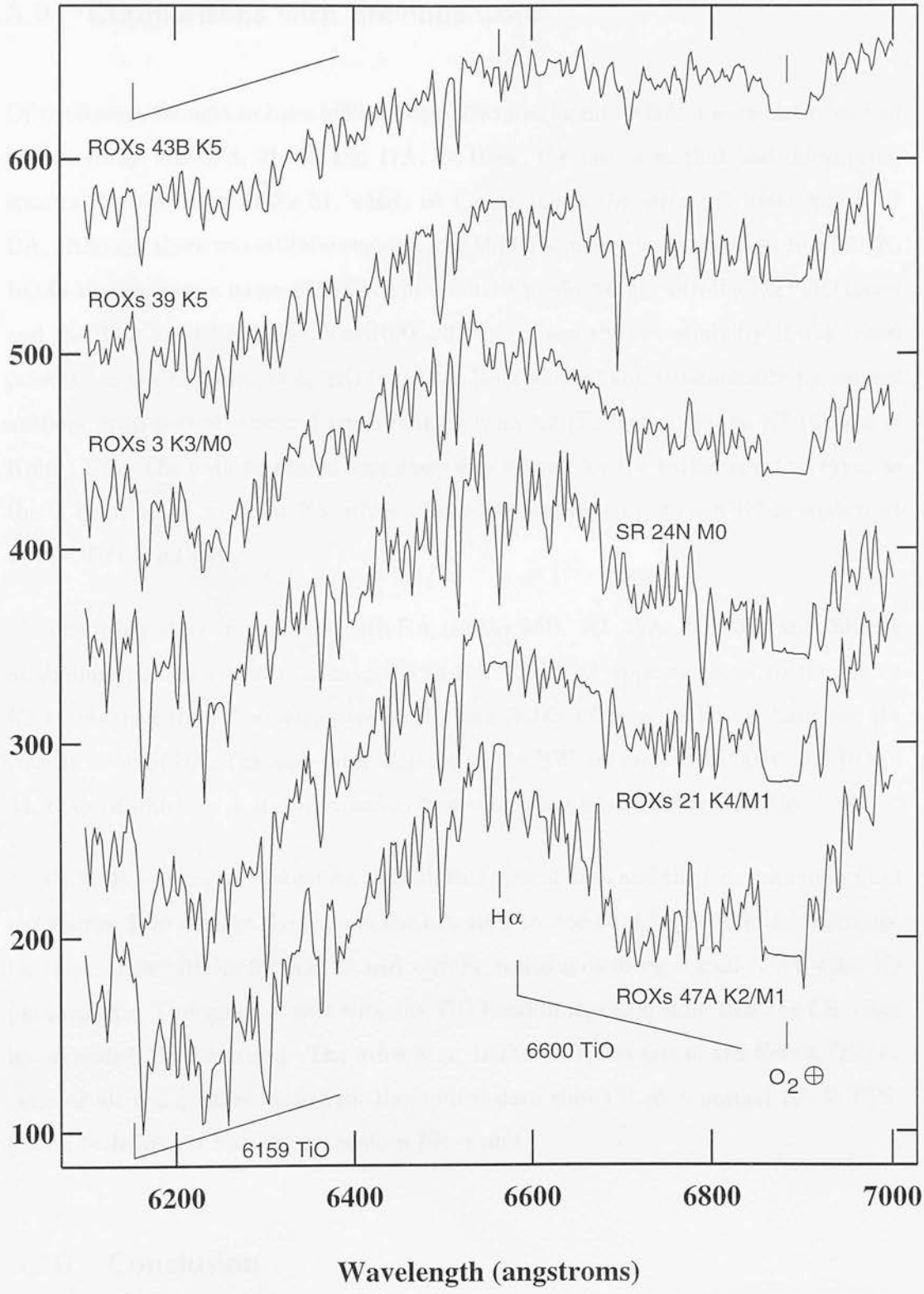

Figure 3.9: The second set of R1 spectra. Note that the Hα line has been truncated where in emission. The spectra have been scaled and shifted for clarity.

3.9 Comparisons with previous work

Of the 5 stars thought to have MST spectral features found by BA, 4 were also observed in this study, ROXs 3, 21, 29 and 47A. Of these, the only star that had no unusual spectral features was ROXs 21, which no longer shows the strong G band found by BA, although there was still the suggetion of MST features when compared to SR 24N. ROXs 29 does have a larger G band than would be predicted by both the Mg/TiO blend and the TiO band heads, as does ROXs 3, which also shows variability in Ca I and possibly in the G band. Only ROXs 29 has been studied spectroscopically by several authors, with derived spectral types ranging from K3 (Padgett 1996) to K7 (Cohen & Kuhi 1979). The data presented here show no evidence for the earlier spectral type, as the G band is too weak for K3, while a later spectral type of at least K7 is confirmed by the TiO band data.

The other stars in common with BA (ROXs 35B, 9C, 38A, 44, 43B, and 39) are of similar spectral types to those given in BA. ROXs 44 appears closer to the K4 or K5 stars, than the K3 as suggested in BA and ROXs 9C may be hotter than the K4 classification of BA. The only large changes in Hα EW are seen in ROXs 6 and ROXs 34, both of which have strong emission lines which are known to be variable.

Only three stars were observed in both this optical data and the I.R. data presented in Chapter 2, as most of the stars in the I.R. set were too faint for FLAIR observations. Of these three, ROXs 29 and 21 had OH/Fe ratios indicating a cool (3500-4000 K) photosphere. This matches well with the TiO band data, confirming that the I.R. data has revealed MST features. The other star, ROXs 43B, has one of the lowest OH/Fe ratio of all young stars measured, the optical data shows it as a normal K5 WTTS, giving little insight into the anomalous I.R. result.

3.10 Conclusion

The overall sensitivity of this study to MST stars is about the same as that in BA. The only stars which have clearly shown MST features are ROXs 29, 47A and 3, which were

already found to be such by BA. The only one of these stars which shows variation in Ca I and the G band between the two nights is ROXs 3, ROXs 29 shows no variation whereas the ROXs 47A spectra are too noisy to discuss variation. The G bands in the MST stars are not directly comparable to any of the low noise spectra presented. They are weaker than that seen in the K3 ROXs 38A, and larger than that seen in the K5 ROXs 39. This suggests that the K4 comparison made by BA is still applicable, although the large change in G band features over this small range means that higher signal/noise spectra are required to perform a proper classification. Changes since the BA study are that ROXs 3, 21 and 47A no longer show the large G band expected from the hotter spectral types assigned by BA.

The R band spectra are in close agreement with those from BA, bar the earlier spectral type seen at all wavelengths for ROXs 9C. The observations of SR 24N have shown that the classification of both ROXs 21 and 47A as M1 in the red by BA was correct.

Whilst this optical study has not discovered any new MST stars, it has demonstrated the variabilty of some features. The R band spectra show no clear daily variation nor have they changed when compared to the results of BA. ROXs 3 has shown variation in the warmer MST features (specifically Ca I and the G band) both on the timescales of days and years.

Chapter 4

The nature of MST stars and their location on the H-R diagram.

There is now much evidence to suggest that a large number of TTSs have MST features. The frequency could range from 11% (BA) to 100% (GHBC). The spectral data from BA and Chapters 2 and 3 has shown that MST features can span anything from ΔT$\approx$110 K (BA, ROXs 29, K4/K6) to ΔT$\approx$1000 K (BA, ROXs 21, K4/M2.5). This has shown that TTSs must contain regions at temperatures different to T_{eff} that are not accounted for in the standard model. In this chapter the various possible sources of this temperature differential are considered, and the resulting position of MST stars on the H-R diagram is explored.

4.1 Models of MST stars

4.1.1 Accretion effects

CTTSs display many spectral features that are thought to originate from the various accretion regions: the disc, the accretion columns and the parts of the photosphere heated by the accretion radiation.

A disc can easily be ruled out as the cause of MST effects, as the temperature structure means it would only show warm features in the regions close to the star (section B.2.2), where the rotational velocities will be so great the broadening would be obvious in high resolution spectra (20 kms^{-1} at 1.6 AU for a $0.5\,M_{\odot}$ star). If the disc is seen face on, its features will not be doppler broadened, but it would have a large affect on the SED of the system. As the MST stars described in GHBC, as well as ROXs 3, are classified as WTTSs it is highly unlikely these sytems contain face-on accretion discs.

The emission from the column, shock front and heated photosphere has been modelled by Calvet & Gullbring (1998). Again, the narrow absorption lines observed constrain the region from which the MST spectra originate. The normal models applied to accretion columns have their rotation fixed to the stellar rotation velocity (Ostriker & Shu, 1995). This leads to the rotational velocity being proportional to the distance from the star, so any features beyond 2 R_* will be seen with velocities greater than 20 kms^{-1}, for a star with a surface rotation of 10 kms^{-1}, which would be a lower limit for WTTSs. For the emission from the inner region, Calvet & Gullbring show that whilst some absorption features can form, the spectra are dominated by strong emission lines, notably the Hydrogen Balmer series and Ca II H & K (see figure 1.2). As some of the stars observed with MST spectra have comparatively low Hα equivalent widths, ROXs 21, 4.2 Å, and ROXs 3, 2.2 Å, as opposed to anything up to 100 Å for some of the CTTSs without MST features (see table 3.2) this rules out the MST spectra being an effect of the normal magnetospheric accretion model.

4.1.2 Chromospheric effects

Most TTSs are known to have chromospheric activity. The sample studied in BA was based on Einstein X-ray observations of the ρ Ophiuchus star forming region, the young stars showing as point sources due to their chromospheric active regions. Active low mass stars contain several emission lines from their chromospheres, most notably Ca II H&K and Hα, although many other lines have chromospheric emission. Weak chromospheric features are seen as line filling in low and medium resolution spectra.

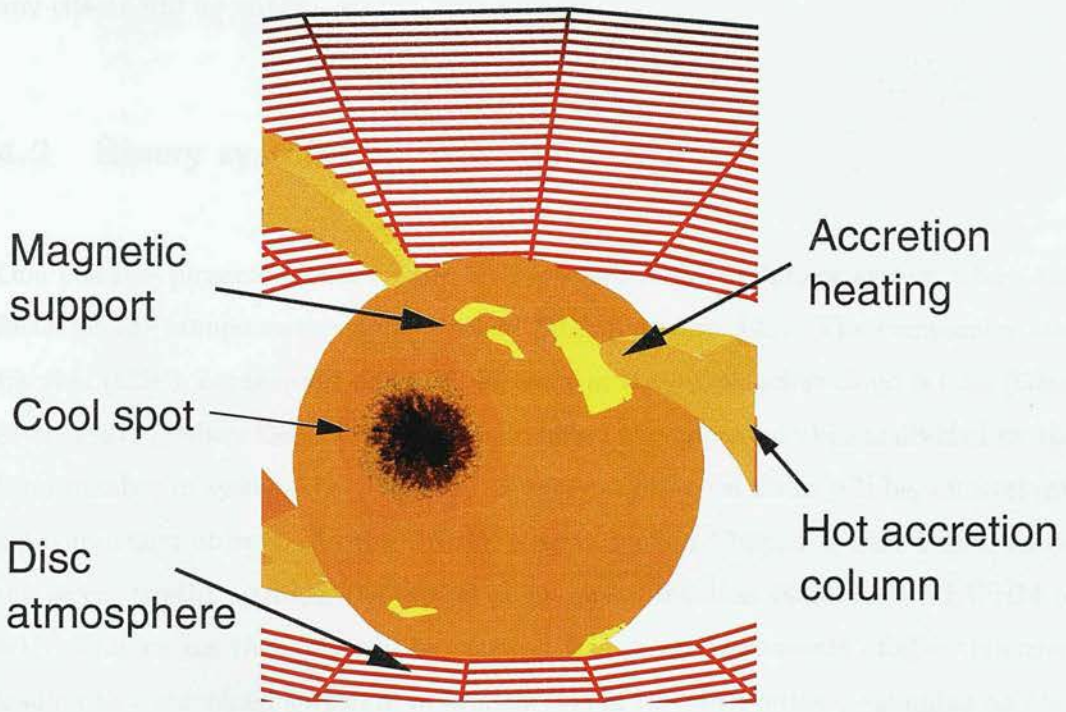

Figure 4.1: The possible sources of optical spectra from a single stellar system

So for spectra that have been classified using only a few lines it is entirely possible for active chromospheres to introduce systematic classification errors.

Of the lines used in Chapter 3 to examine the temperature of the blue spectrum, only the Ca I 4227 Å line shows chromospheric effects in the most active stars. Thatcher & Robinson (1993) investigated chromospheric lines in early-K stars and found that the line was broader in active stars, although the broadening was more closely correlated with spectral type than other activity indicators (e.g. Ca II K emission). BA considered that chromospheric emission was not a likely source of MST effects as their MST spectra did not have strong Ca II H and K emission features, indicating weak chromospheres. BA also noted that the TTSs in a study by Finkenzeller & Basri (1987) did not show MST features despite being chromospherically active.

The Fe lines used in the I.R. data may be affected by an active chromosphere. In this region, not enough of the atomic properties of Fe are known to predict which lines will show emission, but as many lines, with different properties, are used it is thought

any effects will be minimised.

4.2 Binary systems

One possible physical model for the MST phenomenon is a binary system where the SEDs of the components overlap around 5000 Å (figure 4.2). The companion star fraction (CSF), between 0.1 and 1.2″, for stars in the ρ Ophiuchus cloud is 0.23 (Ghez et al. 1997b), where the CSF is the total number of companion objects divided by the total number of systems i.e. for every 10 systems observed there will be, on average, 2.3 companion objects. As the UKIRT observations in Chapter 2 were taken before the recent tip-tilt upgrade, the typical point spread function would have a FWHM of $\approx$1″. This means that flux will be received from both components of close binaries, leading to a combined spectrum in around 20% of the observations, assuming no bias in the sample. These combined spectra will give MST features if the components of the binary have similar flux in the optical.

Examples of the spectra expected from combined binary systems are shown in figures 4.2 and 4.3, these represent the two possible extremes for observed systems producing MST spectra. In the former (figure 4.2) the two stars have an equal flux at $\approx$5500 Å, as suggested by BA. If the contribution from the hotter star was much greater the TiO bands would appear so veiled the effect would clearly been seen in WTTS spectra, similar to the accretion emission veiling seen in CTTSs. The latter (figure 4.3) shows a spectrum much like those seen in the FLAIR data presented in this work, the contribution from the hotter star is low enough that the majority of features are retained from the cool star, but the G band is enhanced in the combined spectrum. If the differences in flux for these two cases were considered to be entirely due to the sizes of the stars: the former would have a cool star with 3.2 times the radius of the hot star, whereas in the latter the size difference would need a factor of 7.

The first detailed investigation into the MST spectra found by BA was performed by Koresko (1995). This study used near-I.R. speckle observations to search for companions around 4 of the stars shown to have MST features by BA. This found companions

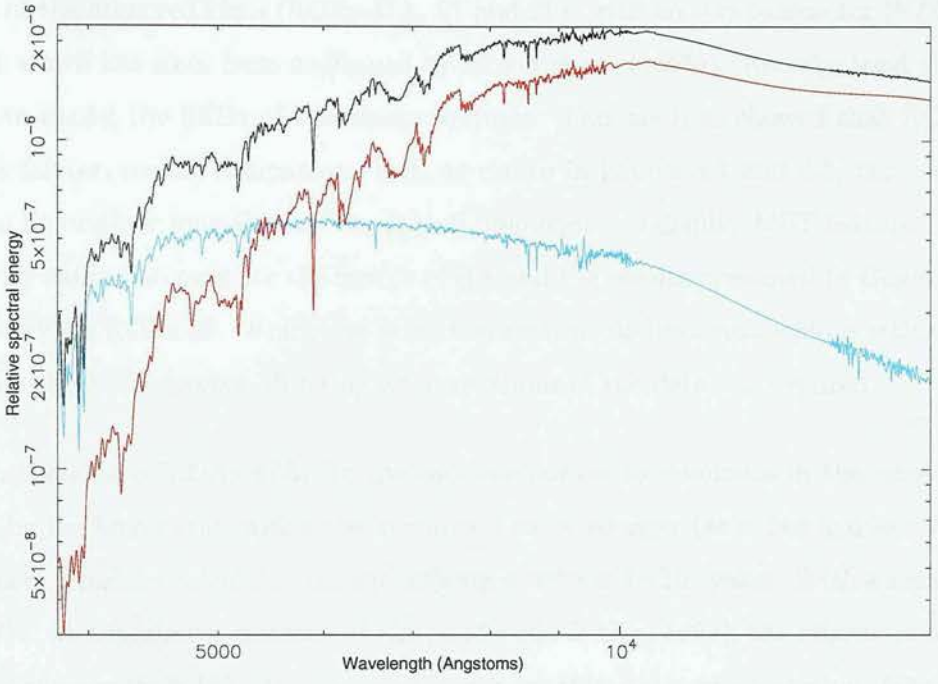

Figure 4.2: The combined spectrum (black) of a G5V photosphere (blue) with an M2V photosphere which has 10× larger area.

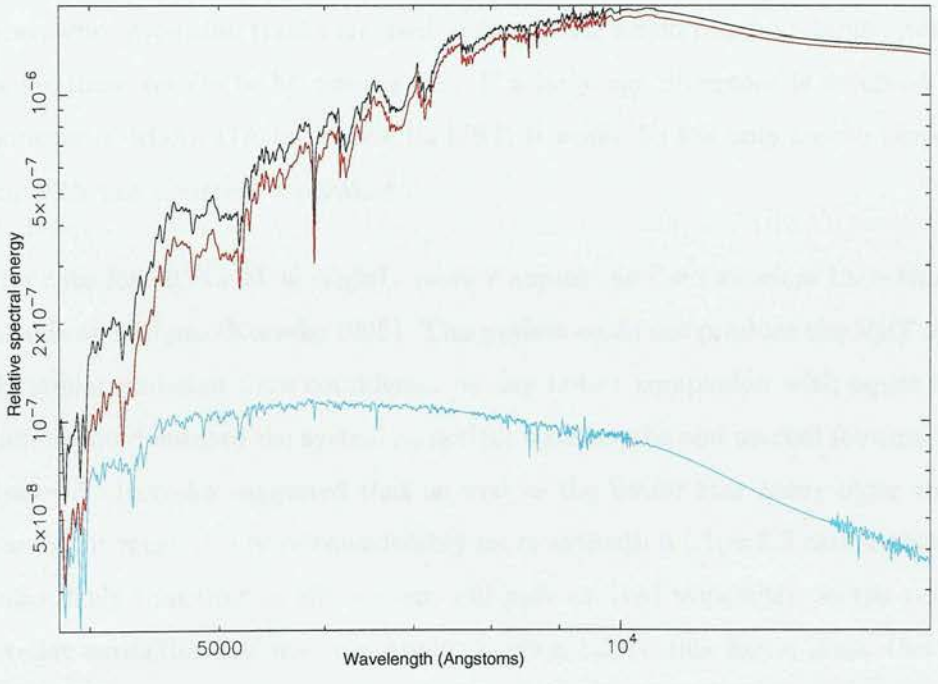

Figure 4.3: The combined spectrum (black) of a G5V photosphere (blue) with an M2V photosphere which has 50× larger area.

for 3 of the observed stars (ROXs 47A, 21 and 29), with no companion for ROXs 3 (a result which has since been confirmed by Simon et al. (1995)). Koresko used the I.R. data to model the SEDs of the binary systems. This analysis showed that ROXs 29 had a fainter, cooler, companion. But, as shown in figures 4.2 and 4.3, the cool star has to be brighter long-ward of the optical blue region to display MST features, so the binarity cannot account for the results of BA and the results presented in Chapter 2 of this work for ROXs 29. Whilst the other two systems do have companions which could explain the MST spectra, differing interpretations of the data are required.

In the case of ROXs 47A, for the cool companion to dominate in the near-I.R. it must be the larger star, which also requires it to be younger (as it has had less time to collapse). Koresko calculated the age difference to be $\approx 1 \times 10^7$ years. With a separation of $0.77''$, at a minimum distance of 120 pc (Knude & Høg, 1998), the minimum separation of these stars is 185 AU. Studies of stars with this apparent separation (Ghez et al. 1997b, Brandner & Zinnecker 1997) have found that systems of this type are normally coeval, with the greatest age difference being 5.5 and 3 Myr respectively. Although these figures are not directly comparable with the results of Koresko, as different pre-main-sequence evolution tracks are used, a factor of 2 would require a large systematic errors for these results to be comparable. If a large age difference is assumed in the components of ROXs 47A to explain its MST, it would be the only known non-coeval system with this apparent separation.

The case for ROXs 21 is slightly more complex, as the two stars have the same magnitude at 1.65 μm (Koresko 1995). This system could not produce the MST spectra if only stellar emission were considered, as any hotter companion with equal flux at 1.65 μm would dominate the system at optical wavelengths and no cool features would be observed. Koresko suggested that as well as the hotter star being older than its companion, it must also have considerably more extinction (A_V=2.2 rather than 1.5). It is also likely that dust in this system will have evolved somewhat, so the standard interstellar extinction law may not apply (Section 1.2.4), this would make the actual difference in A_V greater than suggested. In the other studies of close binaries Ghez et al. (1997b) found all companions had the same A_V within errors, but Brandner & Zinnecker (1997) found variations on the order of those suggested by Koresko. The

observed extremes of coevality and extinction would require that to explain all the features of ROXs 21 with binarity would place the system on the edge of the currently observed parameter space.

The study by Koresko (1995) only found 2 companion stars out of the 4 MST stars observed that might account for the MST effect. Both of these required systems which are not commonly seen in TTSs if the companions were the cause of the effect. GHBC found that all the WTTSs tested showed some degree of MST, this was taken as ruling out a binary model as the chance of randomly selecting 14 TTS systems with the required flux ratios is extremely small.

To conclude, whilst unresolved companions could alter the spectra to produce the MST effect, this would require an as yet unkown, but common, class of TTS multiple system.

4.3 Photospheric features

It is well known that the large magnetic fields on TTSs affect the photosphere to produce spots much larger than those seen on the solar surface. The long term photometric variations seen in many young stars are thought to be due to these spots, a study of which was performed by HHGW. This showed that typical WTTSs displayed photometric variations with a period similar to that of the surface rotation, and had colour variations which would be expected from a photospheric component 1000 K cooler than the stellar surface. The maximum size of cool spot spot discussed by HHGW is 40% whilst the largest spot invoked by GHBC to account for their MST stars is 60%. Figure 4.4 shows the spectrum resulting from such a cool photospheric component covering a G5V star. The majority of this combined spectrum shows the deep metallic lines typical of a G star, but if the region around a broad molecular band is chosen (figure 4.5) the cool features are still visible, although the slope of the G5 spectrum is clearly present when compared to the M2 spectrum. Such an effect might explain the deep Hα line and lack of 6600 Å TiO absorption in ROXs 40, as seen in figure 3.8 (imagine a combination of ROXs 9C and ROXs 47A).

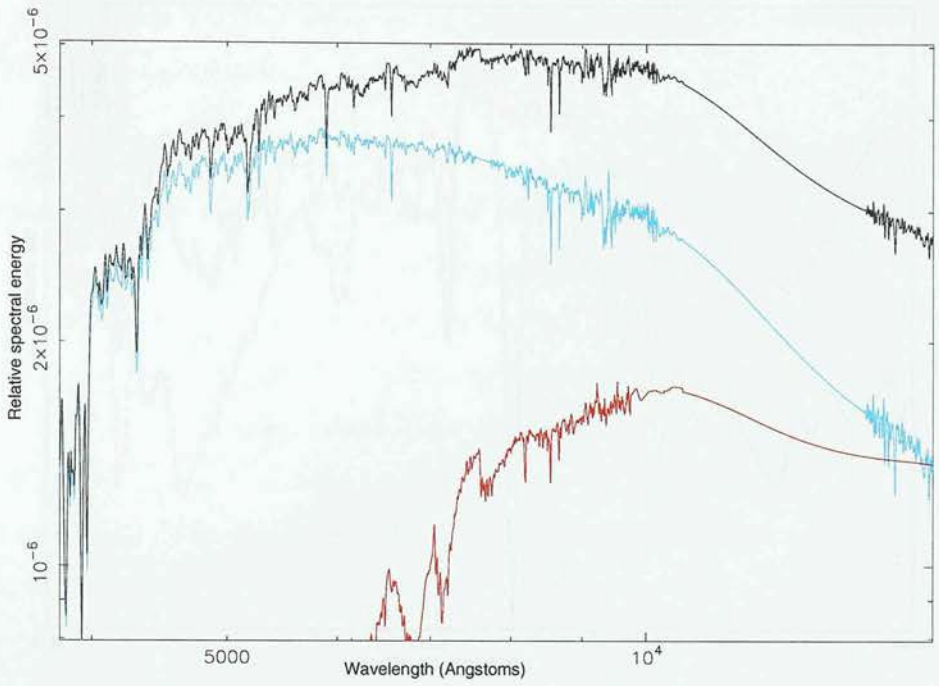

Figure 4.4: The combined spectrum (black) of a G5V photosphere (blue) with an M2V photosphere which has 1.5× the area.

Could the large cool spots seen in photometric variations be responsible for all of the MST results? The main argument against this is the data of BA. This not only shows that the MST spectra only display cool features in the red, but also that the features of the spectra from 5500-7500 Å do not change on the scale of days, contrary to what would be expected from rotationally modulated spots. It is also difficult to explain the differences between the data in BA and that presented in Chapter 3 with large cool spots, as the red spectra are consistent with the results of BA, but the blue spectra show greater variation, with none of the MST stars showing the large G bands found by BA. Again this variation cannot be reconciled with the concept of large cool spots rotating on a warmer photosphere, as a much larger area of spot is required to affect the G band (see figure 4.2).

Cool spots could account for the MST effect if they were evenly distributed across the stellar surface. With such a distribution the features of the stellar disc could be changing with rotation, but the integrated flux would remain the same. The photometric variations would then be explained as a slight uneveness in the distribution. The

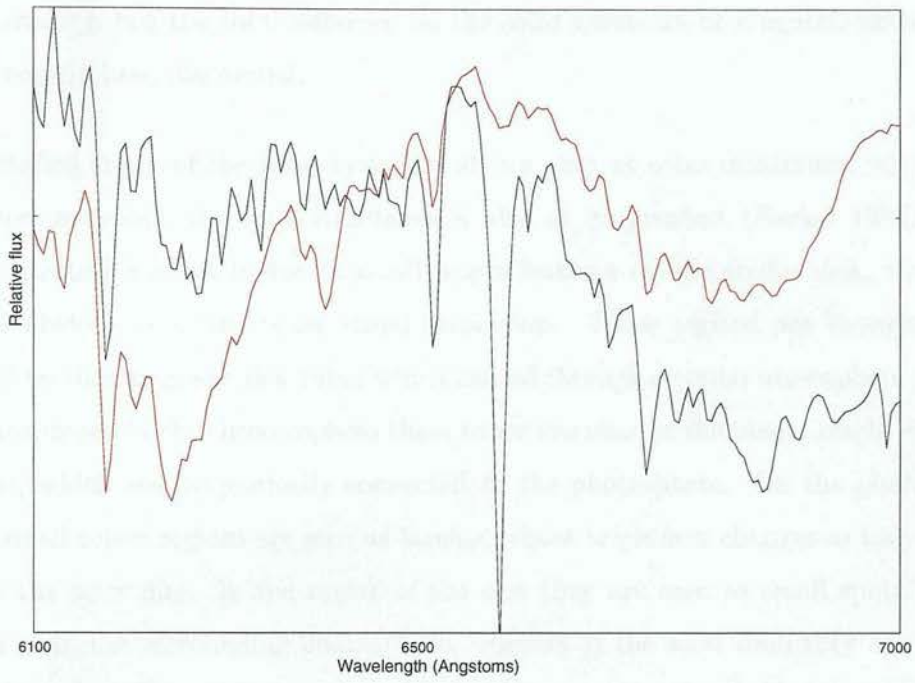

Figure 4.5: The same combined spectra as figure 4.4 (black), but on a flux scale showing the 6100-7000 Å region, as seen in figures 3.8 & 3.9. The red line is the M2V spectrum with the line depths reduced by a factor of 4 and shifted by 7 dex to be comparable.

relative flux arguments would remain the same as above, so the spots would have to cover somewhere between 60% (GHBC) and 90% (figure 4.2) of the surface to create a MST. Clearly, the distribution of spots would either have to be axisymmetric, or be made up of many smaller spots with filaments of 'normal' photosphere between them to create such a coverage. Doppler images of TTSs (section 1.2.2) have neither shown such large groups of cool spots, nor such even distributions. It is difficult to reconcile these results with the invariant spectra of BA if only cool features are present in the photosphere.

Bright photospheric features

As the cool MST features found by BA appear constant, it would seem likely that any unusual photospheric features would have to be warmer than normal photosphere, mainly affecting the blue spectra. Cool spots are often considered on dwarf stars by

solar analogy, but the total influence on the solar spectrum of magnetic activity has only recently been discovered.

Detailed study of the solar cycle has shown that at solar maximum, when there are most sunspots, the total irradiance is also at its greatest (Foukal 1998). This counter-intuitive result is due to small bright features on the stellar disk, which are not as obvious as sunspots on visual inspection. These regions are thought to be formed by thin magnetic flux tubes which extend through a stellar atmosphere into the chromosphere. In the chromosphere these tubes are seen as the plage, bright emission regions, which are magnetically connected to the photosphere. On the photosphere these small active regions are seen as faculae, whose brightness changes as they transit across the solar disc. In the centre of the disc they are seen as small spots slightly darker than the surrounding photosphere, whereas at the solar limb they are seen as bright features. There have been several models to explain these features, but the most widely accepted resembles miniature sunspots.

Figure 4.6 shows a simplified model for solar faculae. The base of the region is cool as the magnetic flux tube supporting the region prevents convection from below, the walls are hot as they are formed in lower regions of the photosphere than are normally seen. The depression is caused by the gas pressure within the region being lower than the normal photosphere, as the total gas+magnetic pressure within the region must balance the gas pressure outside (assuming the change in radiation pressure is negligible).

Even in this simplified form, which ignores all the effects which lead to the formation of plage in the chromosphere, calculation of the emergent spectrum from the region is a complex problem. The first approximation, of modelling the temperature along the $\tau = 1$ line in figure 4.6, picking an observed angle to determine the areas of the structure seen, and then fitting a black-body or standard stellar spectrum to the apparent T_{eff}s, will not work. This is because, at this scale, the height of formation of lines in the stellar atmosphere becomes important. Absorption lines are not formed at the $\tau = 1$ layer, but are formed by any part of the atmosphere along the line of sight where the source function, S_λ, is less than that at $\tau_\lambda = 1$. This requires a model for the atmosphere

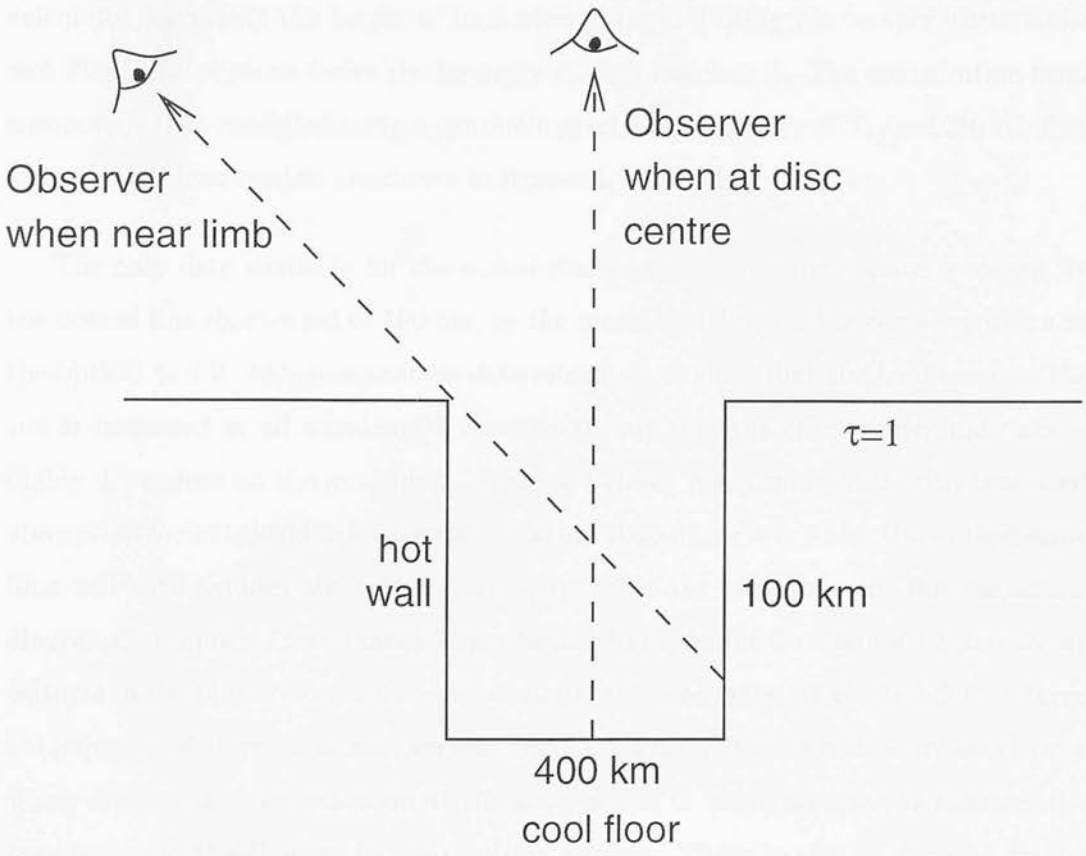

Figure 4.6: A simplified model for the structure of a solar facular spot, after Topka, Tarbell & Title (1997).

above the facular region, as well as a model for the facular depression.

Solanki & Unruh (1998) have developed a model which predicts the spectral changes in solar irradiance. This model does not concentrate on the photospheric shape of faculae, but instead examines the effects of varying vertical temperature structures. The 'quiet' solar surface is taken to be that of the synthetic spectra of Kurucz (1992) at T_{eff}=5777 K and log g=4.44. Two models of the vertical temperature structure are then considered, one is that of the quiet sun, and is used in conjunction with the Planck function to determine the formation height of each wavelength in the Kurucz spectrum. The other vertical temperature structure model is that of the faculae, this starts as being slightly hotter than the quiet model, but is eventually 500 K hotter at 1000 km, the start of region in which the plage is formed. The facular spectrum is then

calculated by taking the height of formation data, and using the temperature model and Planck function to derive the intensity at each wavelength. The contribution from sunspots is then modelled using a synthetic spectrum of Kurucz of T_{eff}=5250 K. Two examples of these models are shown in figures 4.7 and 4.8.

The only data available for the actual change of the solar irradiance is shown by the dotted line short-ward of 400 nm, so the model which gives the correct spectra in the optical to I.R. region cannot be determined. It is clear that the irradiance of the sun is increased at all wavelengths considered, but that the effect individual lines is highly dependent on the modelling. Figure 4.8 shows many more lines with increased absorption for wavelengths long-ward of 400 nm than figure 4.7, which shows that some lines will have reduced absorption (seen as emission like features in the flux variations diagrams). Figure 4.7 has a much larger facular filling factor than figure 4.8 and shows features in the blue region of the optical similar to those found by BA in MST. A large reduction in absorption is seen around the Ca I 4227 Å line, which is followed by a sharp drop in the flux variation at the start of the G band, this would enhance the appearance of the G band in the resulting spectra. There is also an increase in the absorption in the region of the Mg/TiO 4775 Å lines, this could account for the lack a variation seen in these features in section 3.8. The changes seen in the solar spectrum due to increased magnetic activity could easily account for the MST stars. However, to assume that the relative effects of features will remain the same with a factor of 10 increase in the magnetic field would be an over simplification. This is shown by the fact that the model of Unruh, Solanki & Fligge (1999), predicts that the Ca I 4227 Å is smaller and narrower at solar maximum, whereas Thatcher & Robinson (1993) found it to be wider in the active stars they observed.

Faculae on other stars

The determination of the facular filling factor on other stars is very complex due to the dependance of their spectra on the exact stellar structure. Foukal (1998) showed that during the most active solar maxima, the ratio of facular area to sunspot area decreases, compared to typical solar maxima. This matches well with other results by

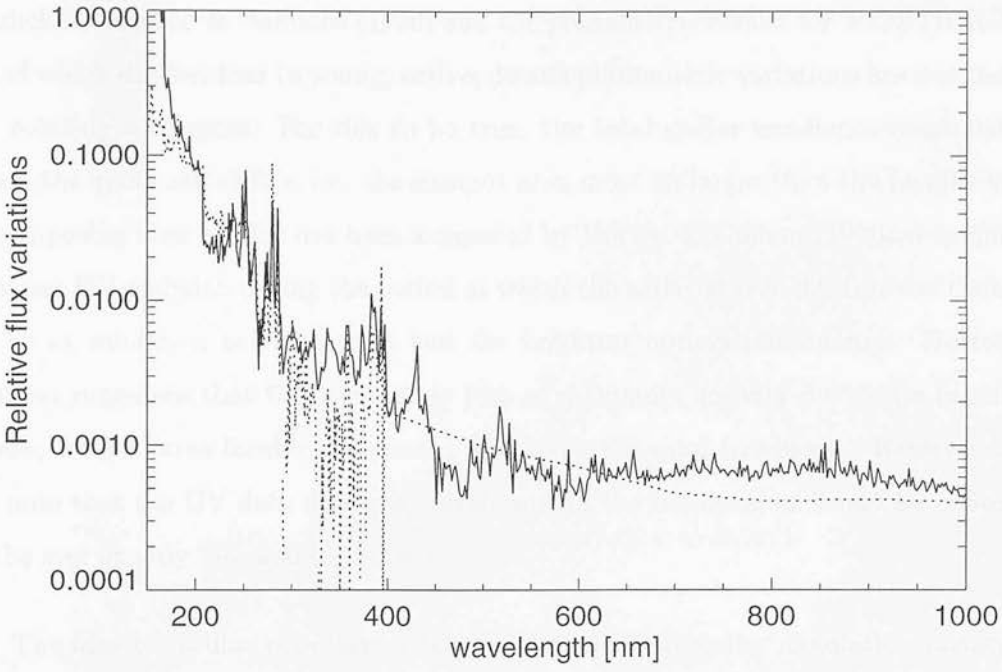

Figure 4.7: The relative flux variations calculated by Unruh, Solanki & Fligge (1999) for a facular filling factor of 2.3% and a spot filling factor of 0.23%.

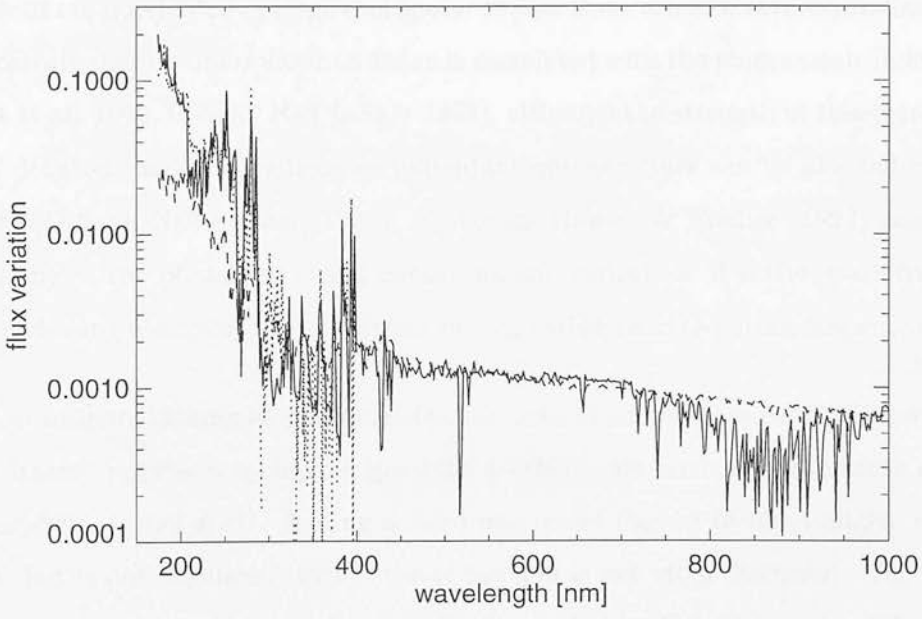

Figure 4.8: The relative flux variations calculated by Solanki & Unruh (1998) for a facular filling factor of 0.04% and a spot filling factor of 0.0025%.

Radick, Lockwood & Baliunas (1990) and the photometric results for TTSs (HHGW), all of which suggest that in young, active, dwarfs photometric variations are dominated by rotating cool spots. For this to be true, the total stellar irradiance must reduce when the spots are visible, i.e. the sunspot area must be larger than the facular area. An opposing view to this has been suggested by Dorren & Guinan (1990), who found greatest UV emission during the period at which the active star V711 Tau was thought to be at minimum activity, as it had the brightest optical photometry. Dorren & Guinan suggested that the star was in fact at maximum activity during its brightest phase, with a large facular component increasing the total irradiance. However they do note that the UV data does not correlate with the Hα data, as would be expected if the star exactly followed the solar model.

The idea of faculae providing a large contribution to stellar irradiation variations has been extended by Pettersen, Hawley & Fisher (1992). They collate data from papers on a range of active stars, concentrating on BY Dra stars, which are K-M type dwarfs displaying photometric variations up to a few tenths of a magnitude. They demonstrate that not all the data agrees with the accepted idea that the photometric variations are purely due to large cool spots. In fact there are now several studies which demonstrate that chromospheric emission is correlated with the photometric light curve (Doyle et al. 1989, O'Neal, Neff & Saar 1998), although the strength of this correlation is still debated, particularly because individual emission lines can be affected by flare activity (O'Neal, Neff & Saar, 1998). Pettersen, Hawley & Fischer (1992) concluded that many of the photometric and chromospheric variations of active stars could be explained using a simple facular network model, rather than requiring large cool spots.

Most authors looking at photometric variations of active stars have taken an "Occam's Razor" approach by finding good fits to their data with 2 temperature models (photosphere + cool spot). Adding a third parameter (bright faculae) might improve the fit, but is not significant within the errors and is not often discussed. The photometric bands that would show the most facular variation, U & B, are also affected by other magnetic features, such as flares. This occurs to the extent that HHGW found very low correlation between rotation phase and U or B magnitude for their WTTSs.

Large photospheric active regions could easily explain the MST effect. The facular component would alter some of the lines seen in blue spectra, although, as shown in figures 4.7 and 4.8, not all lines would show the same apparent temperature change. The cool spot component will enhance the molecular bands used to classify the star in the red, which will extend the scale of the observed temperature differences. Adding features with large temperature variations to the photosphere would also account for the effect seen in GHBC, as the shape of the total spectrum will be significantly different to that of a normal MS star.

4.4 Observability of MST photospheric models

If the MST effect is as common as suggested by the results in GHBC (14 out of 14 stars analysed) it should have been observed many times before it was found by either GHBC or BA. The faculae+cool spots+'quiet' model of active photospheres requires careful interpretation for each observation method applied.

4.4.1 UBV variability

As discussed above, UBV variability would be the perfect photometric method to detect any unusual changes in WTTS facular regions, but this is prevented by the U and B bands being dominated by flare activity. CTTSs will be dominated by accretion optical emission (HHGW). If simultaneous data were taken in the UV and optical, some of this flare 'noise' could be removed. Careful comparisons would then have to be made of the variability in the blue and red optical regions to see if a three temperature model (faculae, quiet photosphere and cool spots) was needed to explain the modulations.

4.4.2 Doppler imaging

As discussed in section 1.2.2, all doppler imaging techniques contain a degeneracy between the photospheric temperature, and temperature of variations. Any attempt

to detect hotter photospheric regions will require good red to I.R. spectroscopy to determine the underlying photospheric temperature. Currently most groups assume that all photospheric features will be cooler than the measured T_{eff}, so the hotter regions will not be detected.

The detection of faculae also provides an interesting problem for doppler imaging groups. As the faculae are only significantly brighter at certain positions in their transit of the stellar disc, the gradual changes in the shapes of lines looked for by doppler imaging code will not be detected. A first approximation is to look for correlation between emission line strengths and spot rotation, as the emission lines will be enhanced by the plage which should be related to any facular features. This method would still require careful interpretation as there is no model for determining the time of the active region maximum, HHGW suggest the photometric minimum implies the largest spots, whereas Pettersen, Hawley & Fisher (1992) suggest the photometric maximum implies the greatest facular coverage.

4.4.3 Modelling the spectral variations

The techniques described in section 1.2.1, where a base photosphere is subtracted to examine the remaining emission components would be the best way to examine the hotter regions. In most CTTSs the blue region of the spectrum will be dominated by accretion related emission, so the technique can only really be applied to WTTSs.

With high resolution, low noise, spectra that span a large wavelength range, it would be possible to determine a typical T_{eff}, an approximate photospheric temperature. A synthetic or empirical model spectrum could then be calculated for the entire spectral region observed, which would be subtracted from the observations. The resulting data would then show if the hotter component is in fact photospheric in nature, giving a T_{eff} for this region, or if the structure of the component is more complex, indicating large active regions. If the star were monitored for a week, the variations in this residual spectrum would provide enough information to determine if the hotter region is due to binarity, or if it is on the stellar surface.

4.5 The effective temperature and luminosity of MST stars.

The MST effect on TTSs will alter the position of stars on the H-R diagram, with both the luminosity and T_{eff} having to be re-evaluated. Spruit & Weiss (1986), investigated the effect of cool spots on the structure of main sequence stars. They found that the influence of spots depended on the internal structure of the star. For ZAMS stars with a convective zone containing a small mass compared to the total mass (such as an $M_{\odot}$ star), it was found that the T_{eff} and radius both increase to balance the flux lost by the spot coverage. For wholly convective stars it was found that the loss of flux from the spotted area is not replaced by the quiet photosphere, but that the radius increases, retaining the original T_{eff}. The results for the ZAMS stars considered are shown in figure 4.9, note that the arrows indicate twice the predicted change.

These results are not exactly those that would be found for TTSs, due to the absence of a central energy source. However, the overall stellar structures of TTSs are sufficiently similar to those of MS stars that their behaviours should be similar in the short term. In the long term no equilibruim spotted model will be found for TTSs as is found ZAMS stars, as the TTSs are not in true hydrostatic equilibrium. Despite this, the initial changes seen in figure 4.9 will be similar to those found in TTSs. If the level of changes is compared to the range and typical errors for TTSs on the H-R diagram (section 1.3), it is clear that the presence of spots on the stars will only minimally alter the derived properties of star forming regions.

4.6 Measuring the T_{eff} of MST stars

As well as investigating the effect of active regions on T_{eff}, it is also important to ensure that T_{eff} is being correctly measured. Figure 4.10 shows the stars for which there are observations both in Chapter 2 and BA, placed on the DM CM Alexander pre-main sequence tracks. The changes in T_{eff} show the differences in temperatures observed by both studies, the luminosity figures are those taken from BA. BA used dereddened V magnitudes to calculate the luminosity by comparison with dwarfs. As

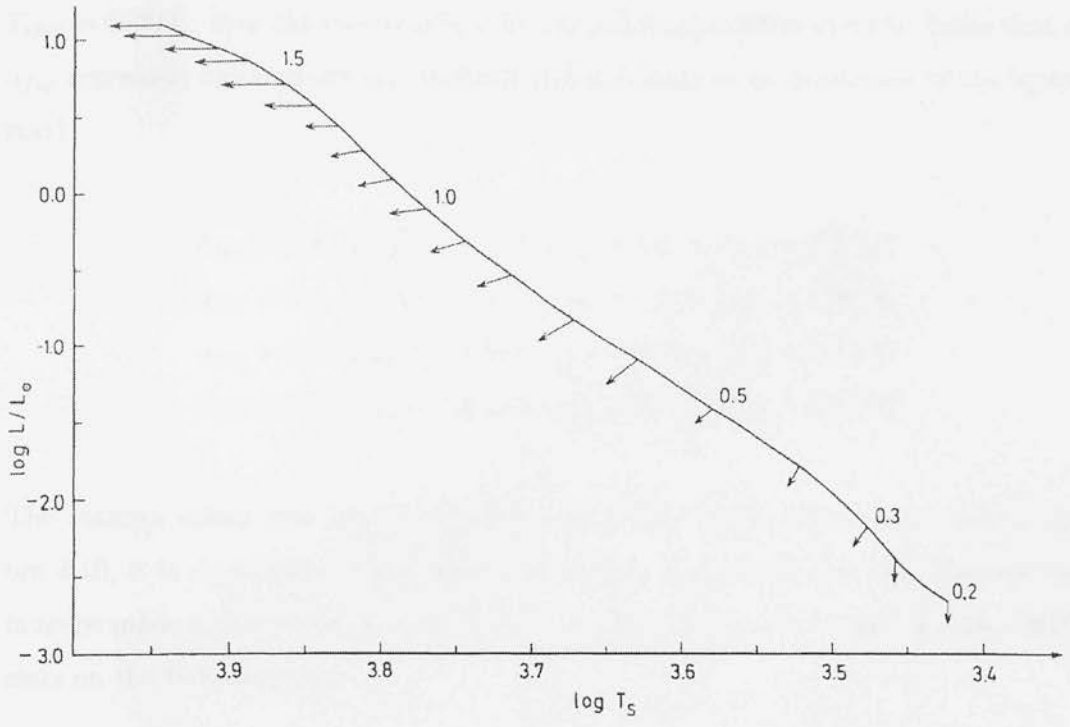

Figure 4.9: The change in position on the H-R diagram for theoretical ZAMS stars. The arrows are twice the length of the change predicted for spots covering 50% of the stellar surface. The numbers indicate stellar mass. From Spruit & Weiss 1986.

shown above, the luminosity of MST stars only changes slightly even with large active regions, so this technique should still be applicable. Figure 4.10 only shows the extreme values of T_{eff} measured in the spectra, neither of which necessarily represent its true value.

The true T_{eff} of the star can only be found by the following method. The total luminosity is the sum of the luminosities of all photospheric regions:

$$L_{tot} = L_{fac} + L_{phot} + L_{spot} \tag{4.1}$$

Assuming the facular contribution is approximately black-body, and applying Stefan's law:

$$T^4_{eff} = a_{fac}T^4_{fac} + a_{phot}T^4_{phot} + a_{spot}T^4_{spot} \tag{4.2}$$

So the T_{eff} of a MST star is depedent on the temperatures and relative areas of each photospheric region. If we take example values of $T_{fac} = 5100$ K, $T_{phot} = 4200$ K and

$T_{spot} = 3500$ K, then the resulting T_{eff} for the following relative areas is: (note that as a_{fac} represents the area of walls the total area is not the same as the area of the 'quiet' star)

$$a_{fac} = 0.0,\ a_{phot} = 0.6 \text{ and } a_{spot} = 0.4 \Rightarrow T_{eff} = 3963 \text{ K}$$
$$a_{fac} = 0.1,\ a_{phot} = 0.6 \text{ and } a_{spot} = 0.3 \Rightarrow T_{eff} = 4160 \text{ K}$$
$$a_{fac} = 0.2,\ a_{phot} = 0.6 \text{ and } a_{spot} = 0.2 \Rightarrow T_{eff} = 4332 \text{ K}$$
$$a_{fac} = 0.2,\ a_{phot} = 0.8 \text{ and } a_{spot} = 0.0 \Rightarrow T_{eff} = 4427 \text{ K}$$

The extreme values give log $T_{eff} = 3.598$ and 3.646. When this is compared to figure 4.10, it is clear that the possible range of T_{eff} is great enough that observations must be made to determine the relative areas of active regions to accurately place MST stars on the H-R diagram.

The errors in studies which do not account for MST effects depends on the wavelength region observed. If a study is based on blue spectra, then the T_{eff} will be overestimated, as the lines used will be dominated by facular and photospheric features. Whereas if the study is based in the near-I.R., the cooler regions will be more prominant, faculae will be ignored, and T_{eff} will be underestimated. Taking the star at $\log(L/L_{\odot})$=0.2 on figure 4.10 as an example, the highest T_{eff}, from BA, will not account for cool spots, whereas the lowest T_{eff}, from Chapter 2, will not account for facular regions. This range of possible T_{eff} creates a factor of 2 uncertainty in the mass.

4.7 Interpreting star forming region parameters with MST stars

If a study of a star forming region is performed using TTS spectra and MST effects are ignored, the errors in T_{eff} for the MST stars will lead to errors in the derived parameters for that region. Figure 4.11 shows two versions of the H-R diagram of the stars observed in the Chameleon star forming region by Alcala et al. (1997). The first

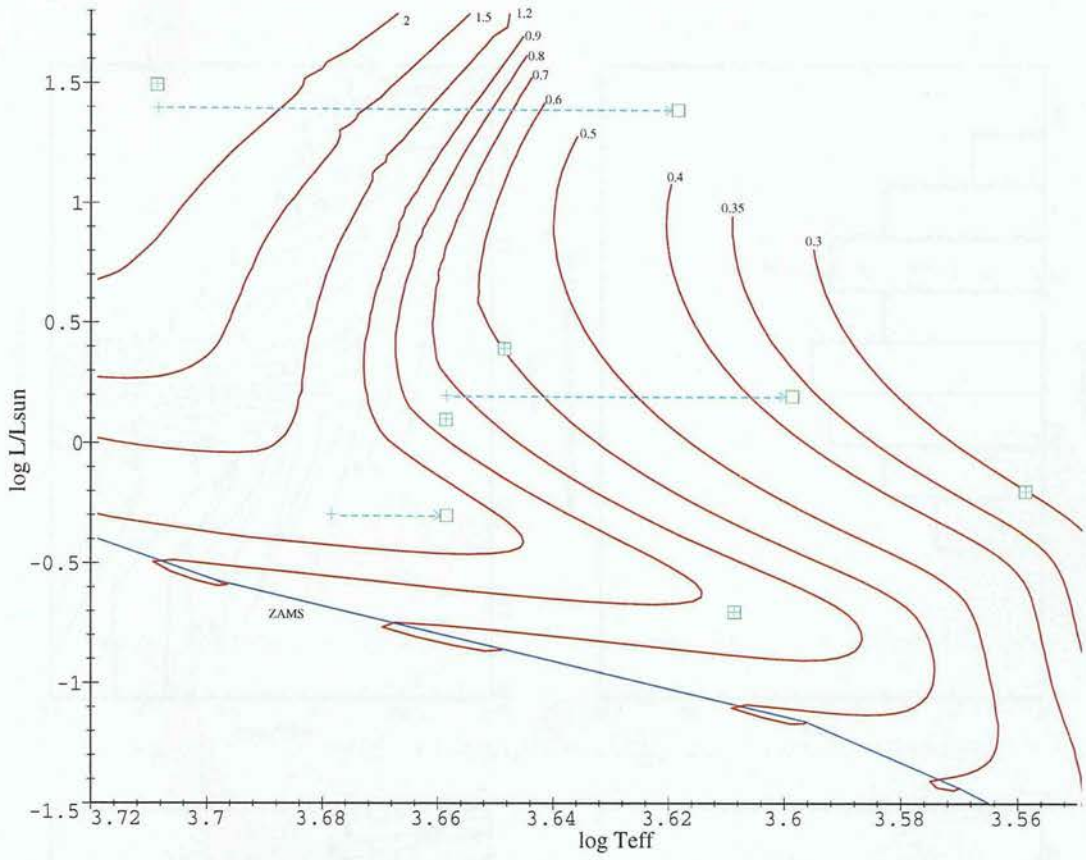

Figure 4.10: The changes in the H-R diagram from BA. The cyan crosses are the data from BA and the green squares are the data from Chapter 2. The solid lines are the DM CM Alexander evolution tracks, with masses at the top of each track.

H-R diagram is of the data reported by Alcala et al., whereas in the second, 25% of the stars hotter than 3500 K have their temperatures reduced by between 500-1500 K. This simulates observations where the selection of spectral type has been dominated by facular regions on MST stars, or large cool spots have been ignored in the T_{eff} calculations. The data from Alcala et al. is only used as an example. The observations were low resolution spectra from 4300 Å and so were less susceptible to facular effects than the observations of BA and Chapter 3. However, the changes shown in the mass distribution diagrams are similar to those that would be seen for studies that do not account for facular features. The lower two figures of figure 4.11 show that the number of lower mass stars would be seriously underestimated if facular features affected the determination of T_{eff}. The change in mass would enhance the deviation at lower

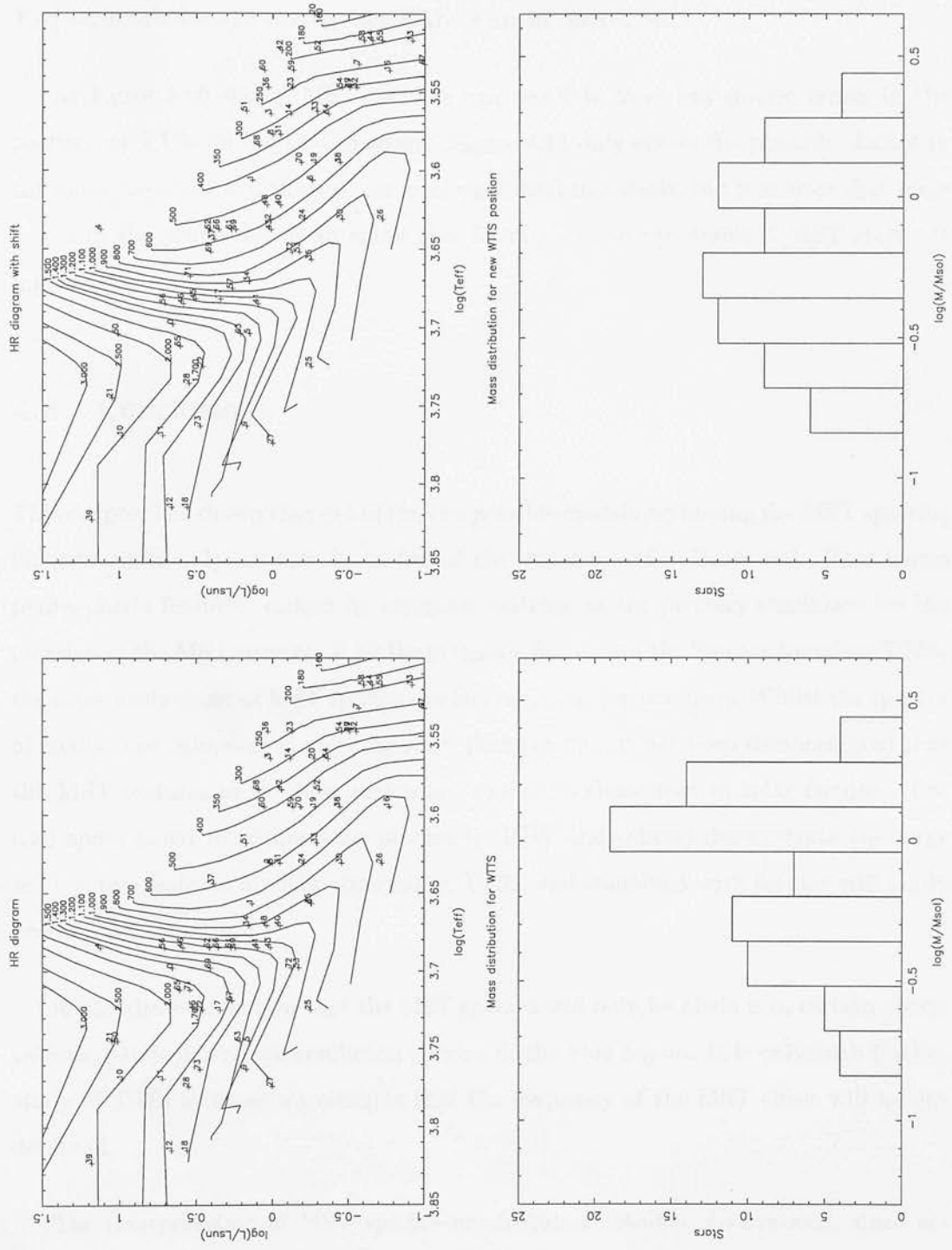

Figure 4.11: The changes in the H-R diagram and mass distribution, assuming the extreme change.

masses from the Scalo (1986) initial mass function (section 1.3) Also, the reduction in T_{eff} would reduce the average age of the stars in the region.

As figure 4.10 shows, MST features can result in large systematic errors in the position of TTSs on the H-R diagram. Figure 4.11 only shows the possible change in the mass distribution if these errors were significant in a study, but it is clear that large errors in the properties of an entire star forming region can result if MST stars are ingnored.

4.8 Conclusion

This chapter has shown that out of the two possible models explaining the MST spectra, binarity could only account for a few of the systems so far discovered. This leaves photospheric features, caused by magnetic activity, as the primary candidate for the creation of the MST spectra. If all the magnetic features of the Sun are found on TTSs, the most likely cause of MST spectra are faculae in the photosphere. Whilst the spectra of faculae are unknown on any star other than the Sun, it has been demonstrated that the MST features in the blue region are similar to those seen in solar faculae. The cool spots found in photometric studies (HHGW and others) demonstrate the large scale active features already observed in TTSs, and combined with faculae will easily produce MST features.

It has also been shown that the MST spectra will only be obvious in certain observations, particularly high resolution spectra of the blue region. It is only with further study of TTSs at these wavelengths that the frequency of the MST effect will be understood.

The interpretation of MST spectra also requires detailed observations, since accurate placement of the stars on the H-R diagram requires knowledge of both the temperatures and relative areas of the active regions and quiet photospheres. The systematic errors introduced if this calculation is not performed correctly can lead to large changes in the mass functions and ages of star forming regions.

Chapter 5

Conclusions

5.1 Observations of the MST effect.

The MST effect has now been observed using three different techniques: the optical spectra presented in BA and Chapter 3, the near-I.R. spectra presented in Chapter 2 and the photometric data of GHBC. Each of these techniques reveal separate regions of the MST effect, and are prone to differing errors.

5.1.1 Optical spectra

It is the optical data which gives the strongest indication of the warmest MST regions. The data from BA (figure 1.7) clearly demonstrates that the MST stars show warmer spectral features towards the blue end of the optical.

The optical study in Chapter 3 did not discover any new MST stars, partially due to weather problems during the observing run. However, it did confirm 3 of the MST detections from BA and demonstrated that the majority of spectral variation occurred in the blue spectra. The changes in the G band of ROXs 3 showed that variations occur on scales of days (figure 3.5) to years, by comparison with BA.

The behaviour of the Mg/TiO band around 4775 Å is interesting when considering the spectral effects of MST stars. As shown in section 3.8 this band follows the spectral type of the TiO bands around 6600 Å much more closely than it does G band, despite this being much nearer, at 4300 Å. The G band is seen as a deep feature in hotter spectra (K3 and earlier), slowly disappearing to M0 stars. The TiO bands around 6600 Å display the opposite behaviour, being very deep in M stars and all but disappearing by K3. In an MST spectra all the deep absorption regions will be seen, so the G band will show an earlier spectral type than would be taken from the Mg/TiO band, despite only being 475 Å apart. Thus it important for any observations searching for MST stars to select a spectral region with lines that will show strong absorption in both hotter and cooler features.

5.1.2 Near-I.R. spectra

Observing in the near-I.R. enables better observations of the cool features, so comparing the data with optical results is a good method for discovering MSTs. The data presented in Chapter 2 demonstrates that a good understanding of the line behaviour is vital.

In Chapter 2 the ratio of OH to Fe lines was used to investigate the near-I.R. spectra, figure 2.7 shows the results. This ratio is affected by both surface gravity and temperature. For stars hotter than ≈4500 K there is only a subtle surface gravity trend, but this increases for cooler stars until the dwarfs have twice the OH/Fe value of the giants around 3500 K. Within the dwarfs and giants the trend with surface gravity and temperature is clear enough to be able to classify individual objects, stars that had previously been misclassified are show in Section A.4. As the TTSs do not have a known surface gravity, it is only possible to put limits on their measured temperatures. A TTS with OH/Fe=3 could range from 4200 K, with $\log g = 5$ to 3200 K, with $\log g = 4$. Any surface gravity lower than this would start to show the large 1.619 μm CO bandhead seen in the giants. Therefore MSTs are seen very clearly in the near-I.R. for stars with an optically measured $T_{eff} > 4500$ K.

Within the surface gravity constraints, figure 2.7 shows four clear MST candidates,

of which two are new discoveries. ROXs 16 was observed in BA and was not found to have an MST spectrum. The increased sensitivity of the near-I.R. technique indicates a region $\approx$700 K cooler than that observed by BA.

5.1.3 Optical photometry

To date the only photometric study of MSTs is that of GHBC. Whilst photometry is the quickest technique to search for MST stars, it is also the method most likely to suffer contamination. Flares, extinction and companions can all influence photometric results. GHBC found that both extinction and companions could not explain all their results and flares would only affect the bluer filters. Despite this, care would have to be taken in any future studies, e.g. to ensure only WTTSs were investigated, to avoid any disc contamination.

5.2 The frequency of MST stars

The fraction of TTSs that contain MST features is still an unknown factor. The study of BA found 5/47, or 11% of stars observed had some degree of MST features. The fact that ROXs 16 was also detected as an MST (giving a frequency of 12%) in the near-I.R. of Chapter 2 indicates some objects will have been missed by BA, and can only be shown using techniques more sensitive to the MST effect. GHBC found that 100% of the WTTSs studied demonstrated some MST features. The photometric technique applied is not as selective as the spectral methods, so some contamination from unresolved binaries and misidentified CTTSs will be present. The current studies, therefore, only indicate that the frequency of MST stars is $> 12\%$ and $< 100\%$.

5.3 Models of MST stars

In Chapter 4 it was shown that whilst certain types of TTS binary systems could account for the MST effect, they could not account for all the observations. In fact,

if the CSF of ρ Ophiuchus is 0.23 (Ghez et al. 1997b), and the MST frequency is $> 12\%$, at least half of the observed multiple systems would have to have the peculiar conditions required to explain MSTs, which is highly unlikely. It was also shown that none of the features included in the standard model of TTSs could explain the MST effect, mainly because it has been observed in both CTTSs and WTTSs.

This leaves photospheric features, probably caused by magnetic activity, as the primary candidate for the creation of the MST spectra. To date, the main form of photospheric activity considered is cool spots, which have been detected by both variability studies (HHGW) and doppler imaging (Section 1.2.2). To explain the MST spectra as cool spots requires a spot coverage of 60% (GHBC) to 90% (BA), sizes which have not been found using current techniques. The only dwarf star in which the features of magnetic activity are fully observed is the Sun. It has recently be shown that the dominant solar photospheric active regions are, in fact, faculae (Foukal, 1998). These small, bright, active regions cause an increase in the solar irradiance at solar maximum, when there are the most sunspots. Even though it is unlikely that the physics can simply be scaled from a comparatively magnetically quite Sun, through to the highly magnetic TTSs, it seems hasty to ignore facular effects. Unfortunately, the exact form of the solar facular spectra is still unknown for all wavelengths, the change in contrast as the regions cross the solar disc creating particular problems. This means that the exact effect of stellar faculae cannot be easily calculated, but it has been shown in Chapter 4 that the models for solar faculae spectra would give MST effects very similar to those seen in BA and Chapter 3 if they were seen to a greater extent in TTSs. If the solar model can be scaled to the levels of magnetic activity seen in TTSs then when we see faculae we would expect to see star spots, and visa versa.

It is this result, that the spectra of TTSs can show features from bright photospheric regions, which can significantly alter the interpretation of these spectra, that is the main result of this work.

5.4 Changes in the H-R diagram and properties of star forming regions with MST effects.

MST effects alter the position of stars on the H-R diagram. To accurately determine the T_{eff} of MST stars, the relative coverage of each photospheric region has to be determined. It was demonstrated in section 4.5 that the presence of any active regions can alter the T_{eff} by a few hundred K. This will lead to an over or underestimation of T_{eff} if only one wavelength region is used to classify the star, depending on which temperature range the observations are sensitive to. The luminosity will not generally be changed by the active regions, as this is normally measured over several wavelengths, so all the regions will be observed. If the study of BA is taken as typical, spectra taken in the blue will overestimate T_{eff}, this will reduce the higher mass end of the mass function for a star forming region and reduce the average age of the region.

It is only when the average effects of active regions of TTSs are fully determined that the true mass function and age of star forming regions can be determined.

5.5 Future work

There are two main areas of research that can follow on from this work:

- To find best way to account for MST features in spectra, in order to find a good method of determining T_{eff}.
- To find features which are particularly sensitive to the MST features, in order to examine the active regions of TTSs.

Both of areas of future study will require a good indication of the true frequency of the MST effect. This could be found in two ways. One telescope could be used to perform observations similar to those presented in Chapter 3, but with a better signal to noise ratio, and with more objects in the sample. This could be achieved with a system such as the 2dF on the AAT. The other observing option would be to perform

both optical and near-I.R. spectral studies, using a method simialar to that described in Chapter 2 to find MST stars. This would require the use of two telescopes, such as WHT and UKIRT. Careful consideration would have to be given when selecting the sample of stars for near-I.R. spectroscopy. If the same spectral region as in Chapter 2 was observed, it would only be worthwile observing TTSs with spectral types earlier than K5, as later than this, differing surface gravities will confuse the MST effect. Of course, different observing techniques will be sensitive to different temperature regions.

An interesting new area of study would be to compare the facular effects of MST stars with other indicators of active regions. This would require a high resolution spectral study in the blue optical region, and possibly simultaneous photometry. This would enable MST effects to be compared directly with chromospheric emission and photometric variation. This data would reveal if TTSs display solar-like activity, with all active regions being visible simultaneosly, or if cool spots dominate the regions of the photosphere that they cover.

Object	Spectral Types	R.A.	Dec.	Ref.
ROXs 2	K3/M0	16 25 55	-23 55 30	BA
ROXs 3	K3/M0	16 25 49	-23 51 00	BA/Ch. 3
ROXs 21	K4/M1.5	16 27 20	-24 41 40	BA/Ch. 2/3
ROXs 29	K4/K6	16 27 40	-24 22 02	BA/Ch. 2/3
ROXs 47A	K2/K7-M0	16 32 11	-24 40 12	BA
ROXs 16	G9/K7	16 26 46	-24 12 00	Ch. 2
LKHα 191	K0/K6	20 59 06	43 57 06	Ch. 2
LkCa 3	M1	04 14 48	27 52 35	GHBC
LkCa 4	K7	04 14 28	28 07 37	GHBC
LkCa 7	K7	04 19 41	27 49 39	GHBC
HBC 376	K7	04 18 52	17 23 15	GHBC
HBC 427	K7	04 56 02	30 21 03	GHBC
L1551-51	K7	04 32 09	17 57 23	GHBC
L1551-55	K7	04 32 44	18 02 58	GHBC
V819 Tau	K7	04 19 26	28 26 14	GHBC
V826 Tau	K7	04 32 15	18 01 42	GHBC
V827 Tau	K7	04 32 15	18 20 15	GHBC
V830 Tau	K7	04 33 13	24 34 18	GHBC
V836 Tau	K7	05 00 02	25 23 20	GHBC
VY Tau	M0	04 39 18	22 48 00	GHBC
IW Tau	K7	04 41 05	24 51 07	GHBC

Table 5.1: The MST stars observed thus far.

Appendix A

The Spectra

A.1 The Giant stars

This section contains the near-I.R. spectra of the giants as discussed in Chapter 2.

Figure	Object	Spectral Type	T_{eff}
1	BS 6308	M1III	3343
	BS 7798	K0III	4720
	BS 7800	K7III	3967
2	BS 7919	K2III	4474
	BS 7969	K5III	4159
	BS 8517	M4III	3277
3	BS 8699	M0III	3711
	BS 8833	G8III	4822

Table A.1: The giant stars

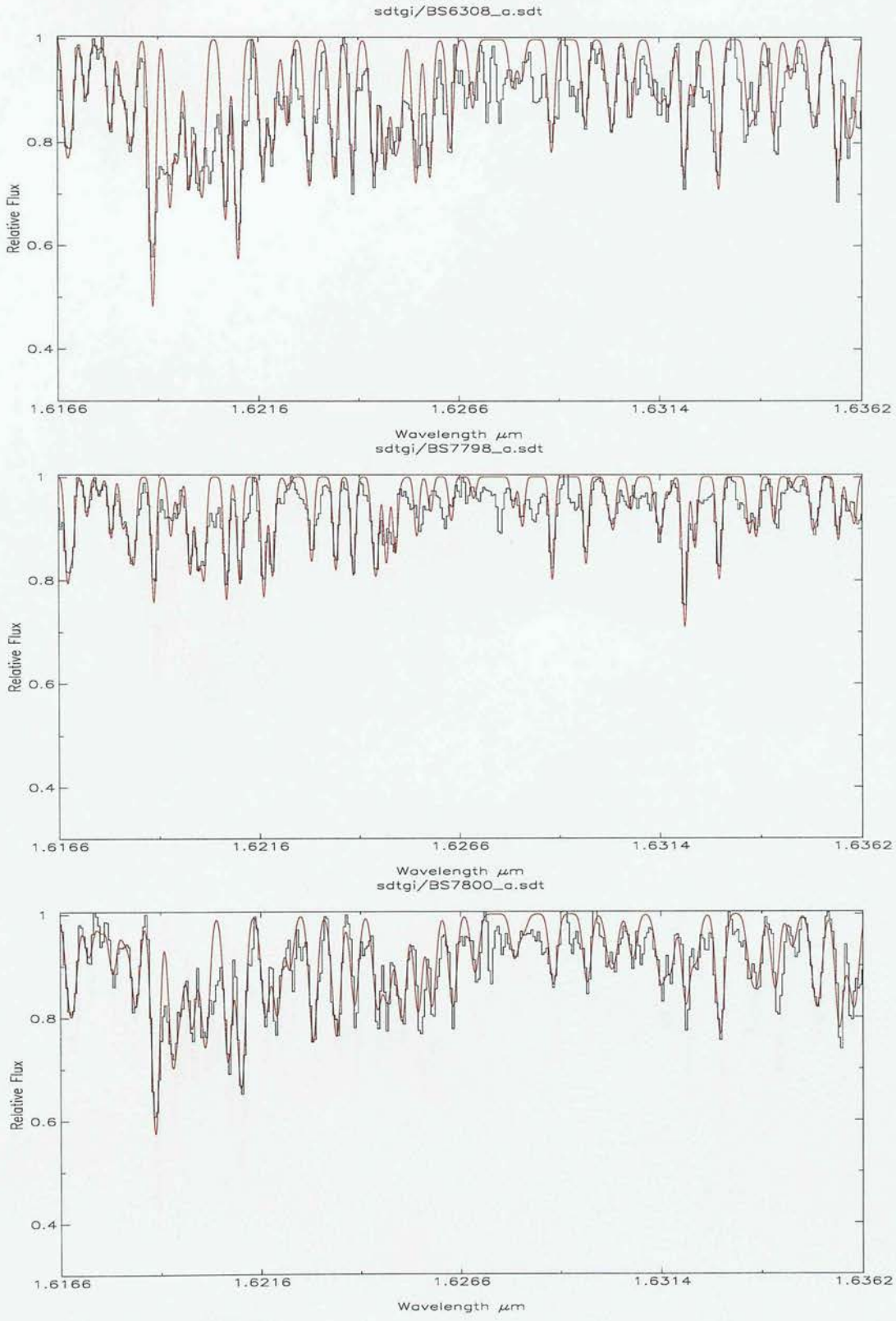

Figure A.1: BS 6308 M1III, BS 7798 K0III and BS 7800 K7III

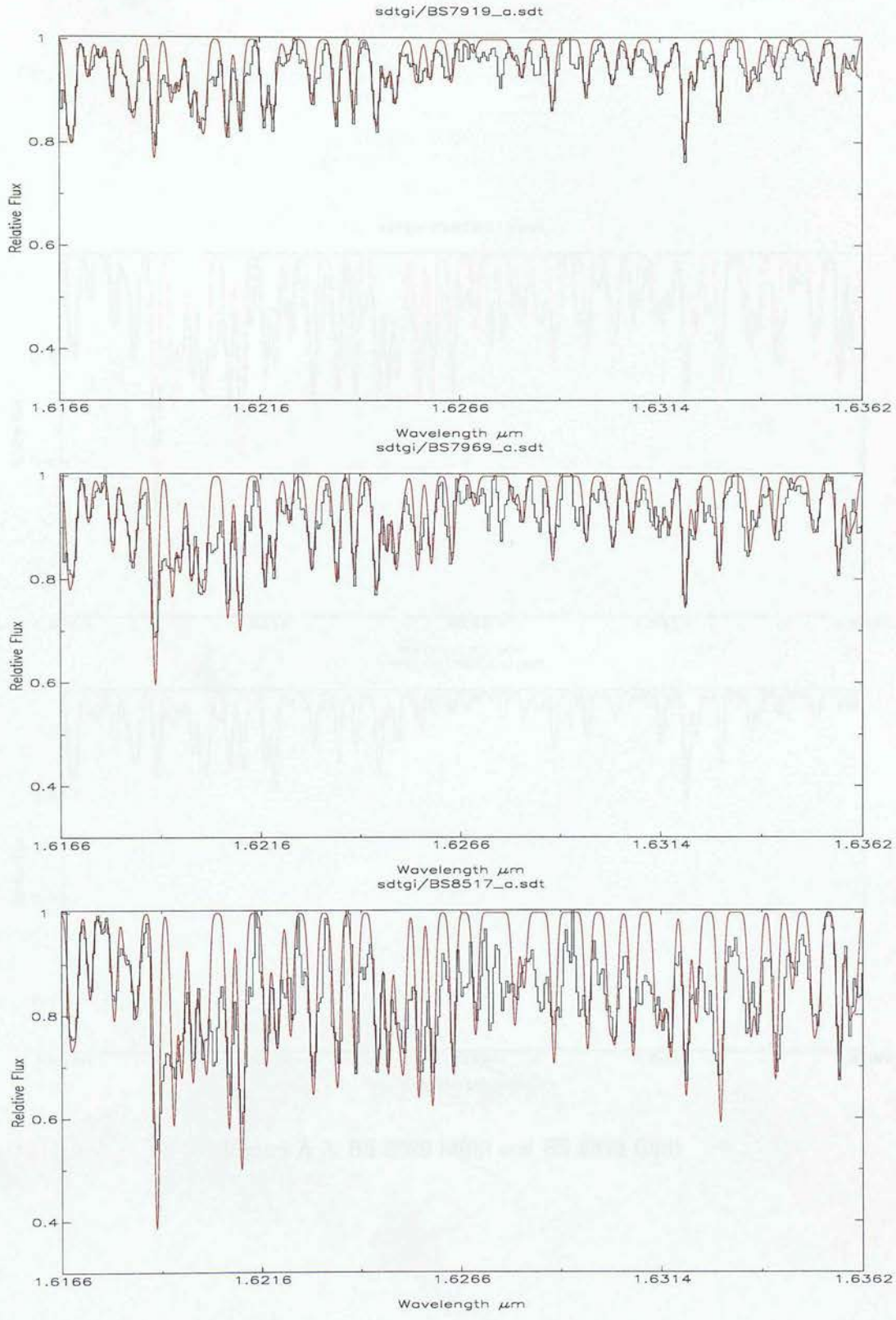

Figure A.2: BS 7919 K2III, BS 7969 K5III and BS 8517 M4III

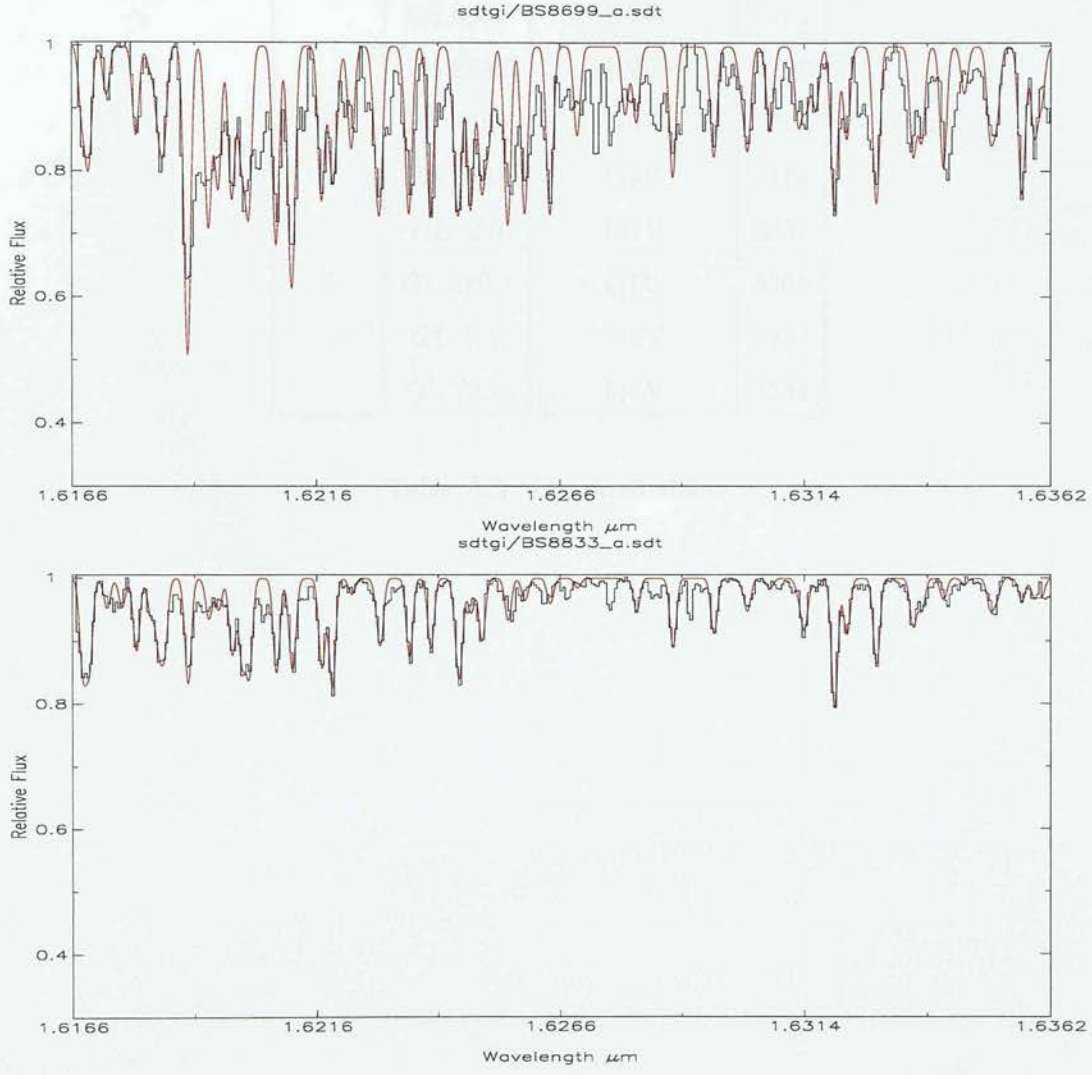

Figure A.3: BS 8699 M0III and BS 8833 G8III

A.2 The Dwarf stars

This section contains the dwarfs as discussed in Chapter 2.

Figure	Object	Spectral Type	T_{eff}
4	BS 8085	K5V	4600
	BS 8086	K7V	4382
	BS 8382	K2V	4927
5	BS 8455	G0V	5702
	BS 8631	G4V	5474
	GL 450	M1V	3837
6	GL 486.1	G7V	5308
	GL 526	M3V	3424
	GL 725a	M4V	3234

Table A.2: The dwarf stars

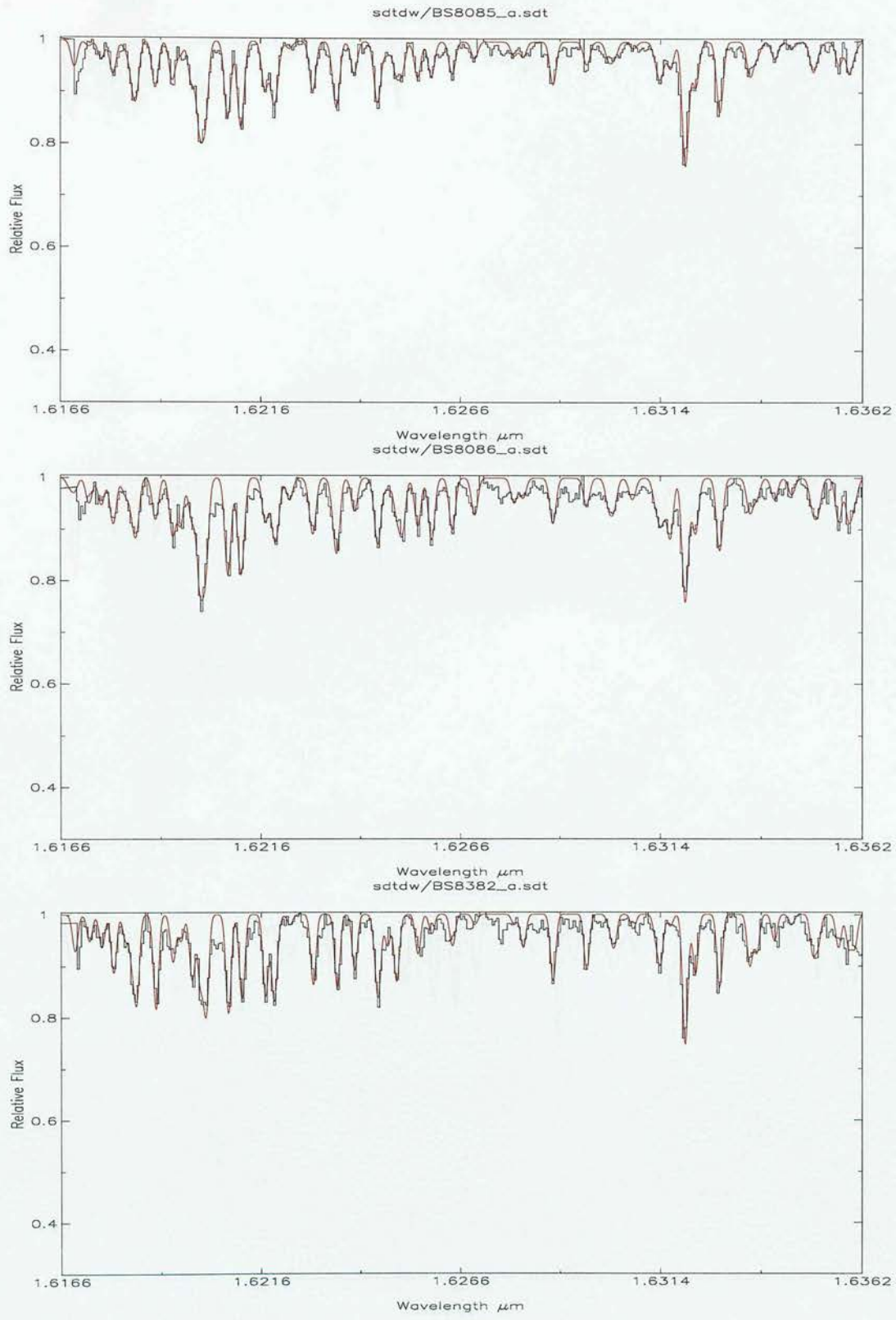

Figure A.4: BS 8085 K5V, BS 8086 K7V and BS 8382 K2V

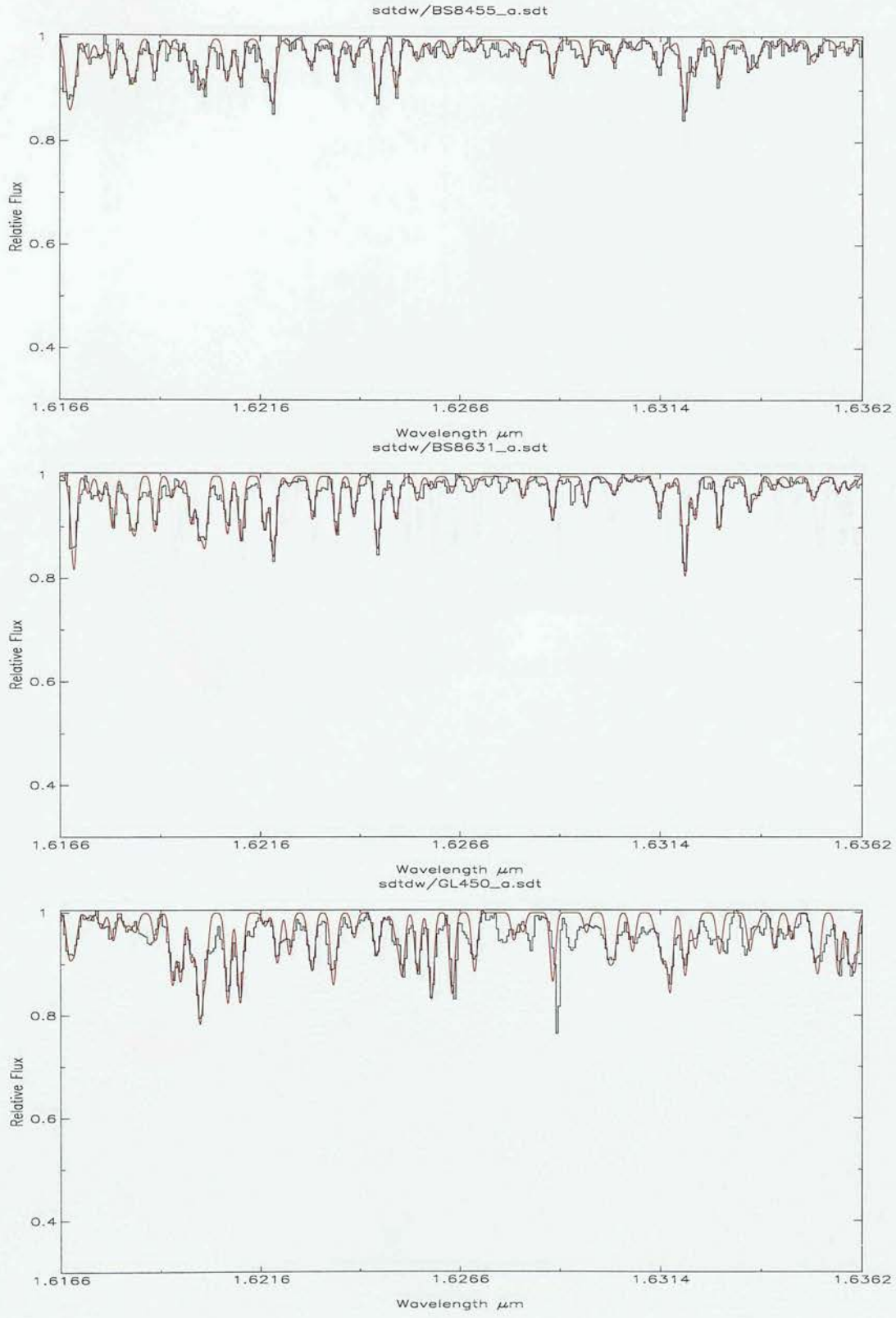

Figure A.5: BS 8455 G0V, BS 8631 G4V and GL 450 M1V

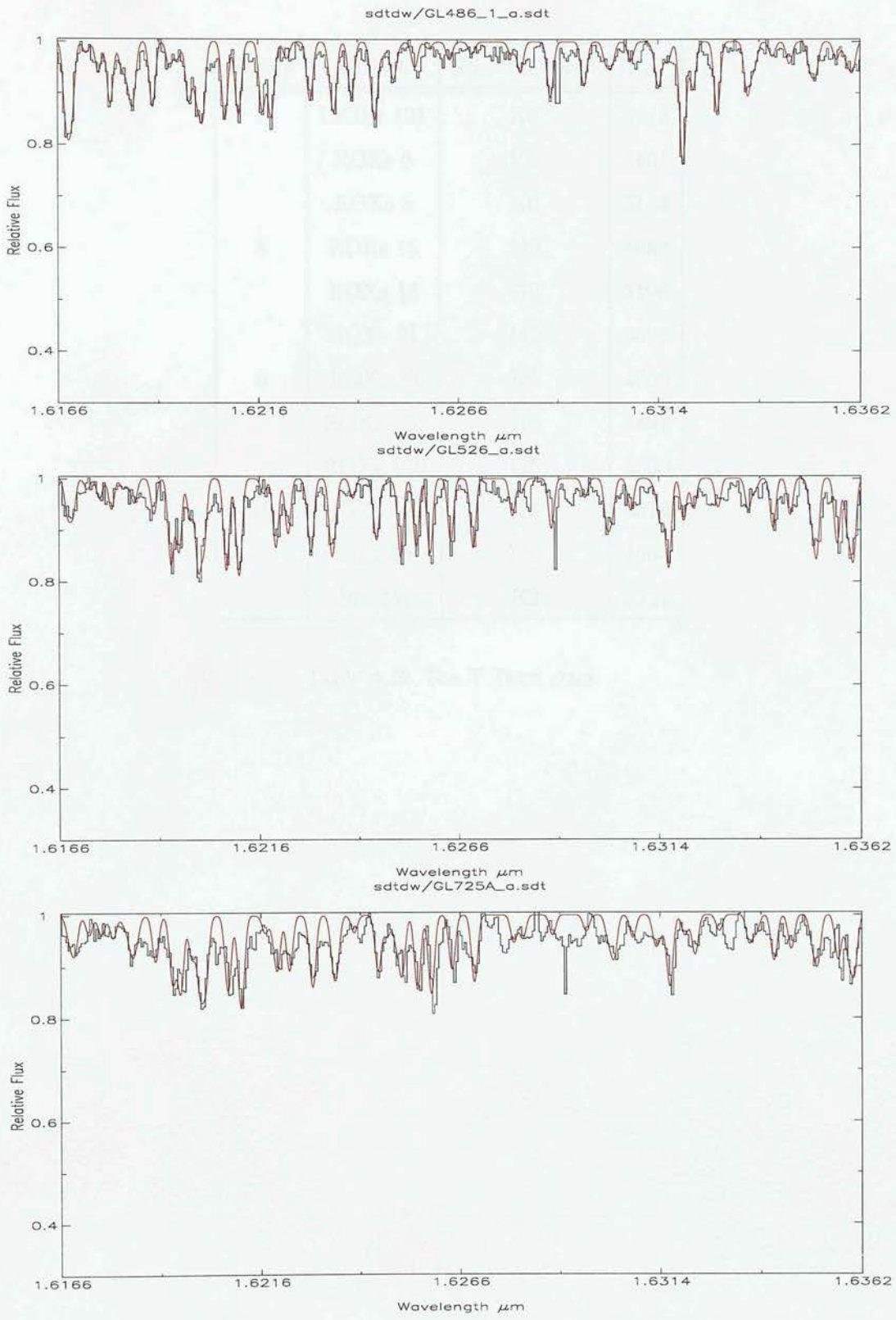

Figure A.6: GL 486.1 G7V, GL 526 M3V and GL 725a M4V

A.3 The T Tauris

Figure	Object	Spectral Type	T_{eff}
7	LKHα 191	K0	5143
	ROXs 6	K6	4491
	ROXs 8	K0	5143
8	ROXs 12	M0	4053
	ROXs 16	G9	5198
	ROXs 21	M2	3626
9	ROXs 29	K4	4600
	ROXs 42c	K6	4491
	ROXs 43b	K5	4600
10	ROXs 47b	K3	4818
	SR 24n	M0	4053
	SR 24s	K2	4927

Table A.3: The T Tauri stars

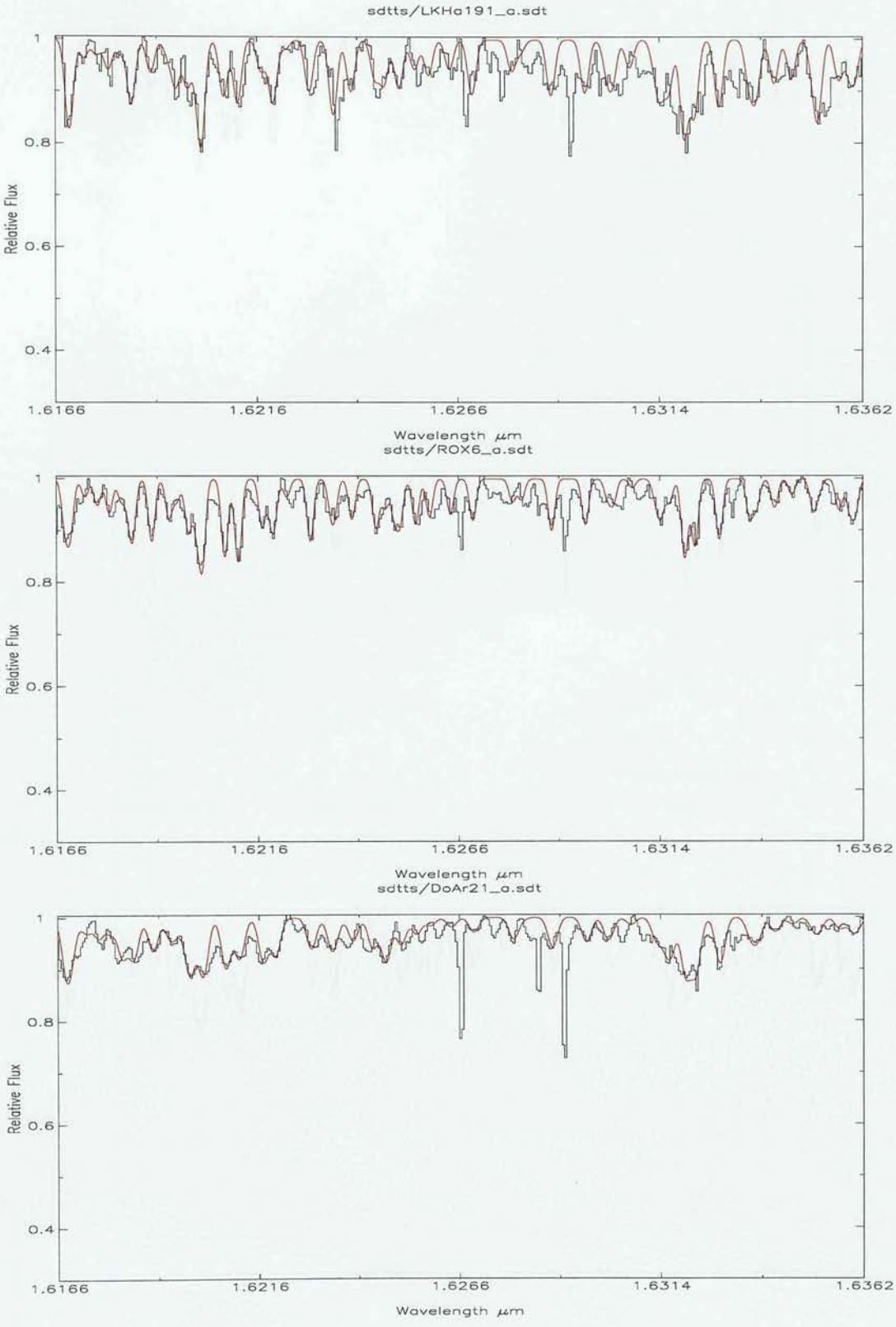

Figure A.7: LKHα 191 K0, ROXs 6 K6 and ROXs 8 K0

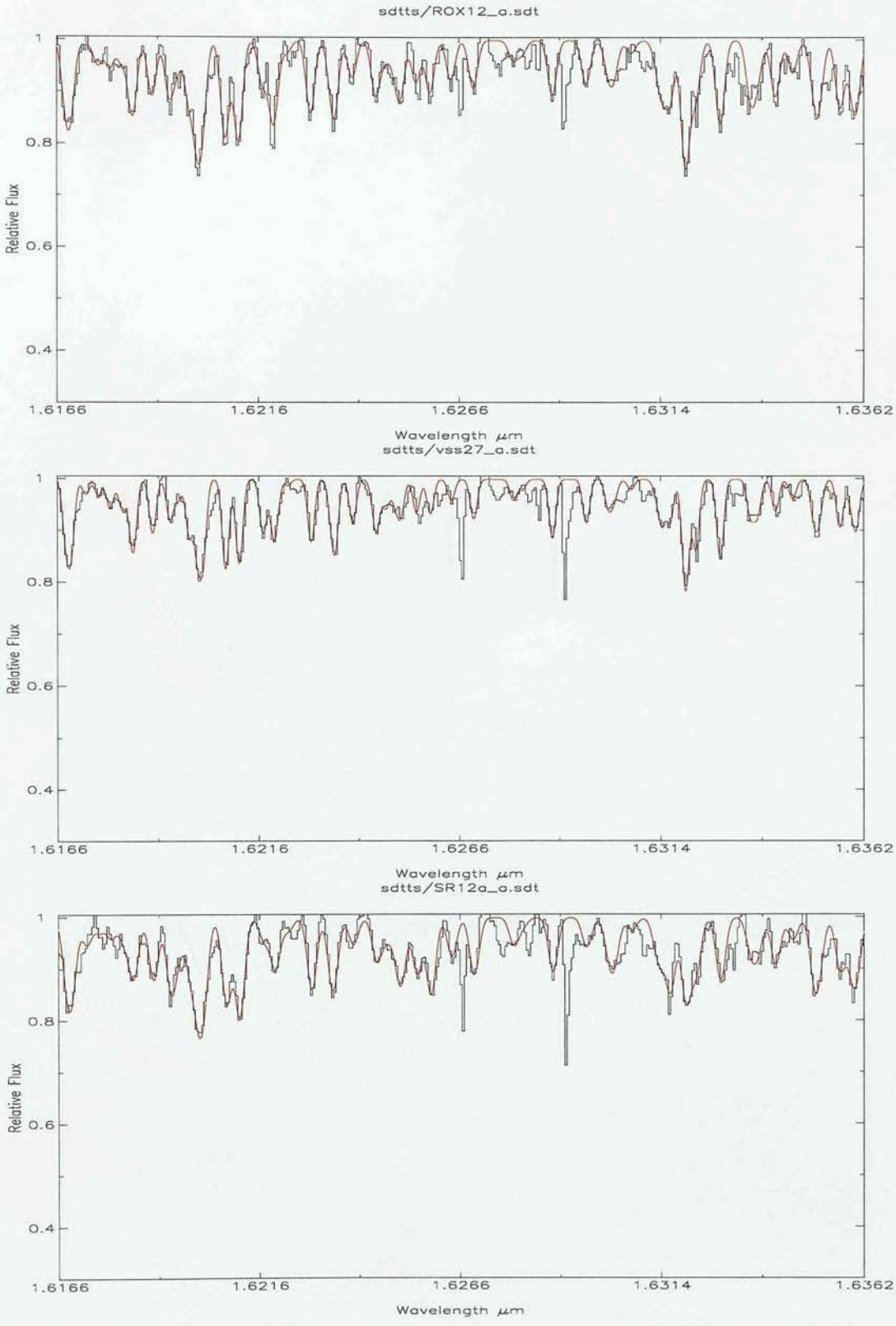

Figure A.8: ROXs 12 M0, ROXs 16 G9 and ROXs 21 M2

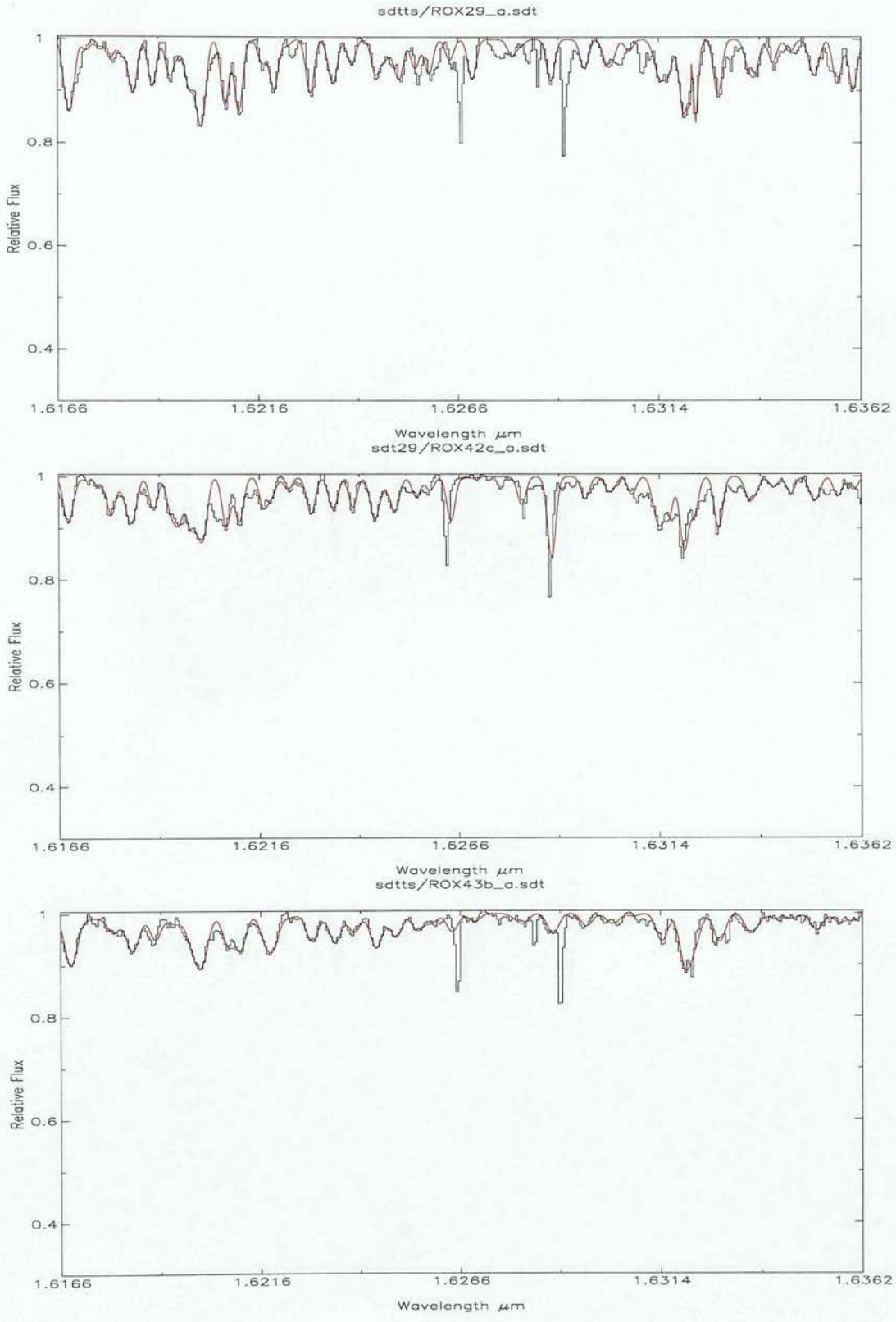

Figure A.9: ROXs 29 K4, ROXs 42c K6 and ROXs 43b K5

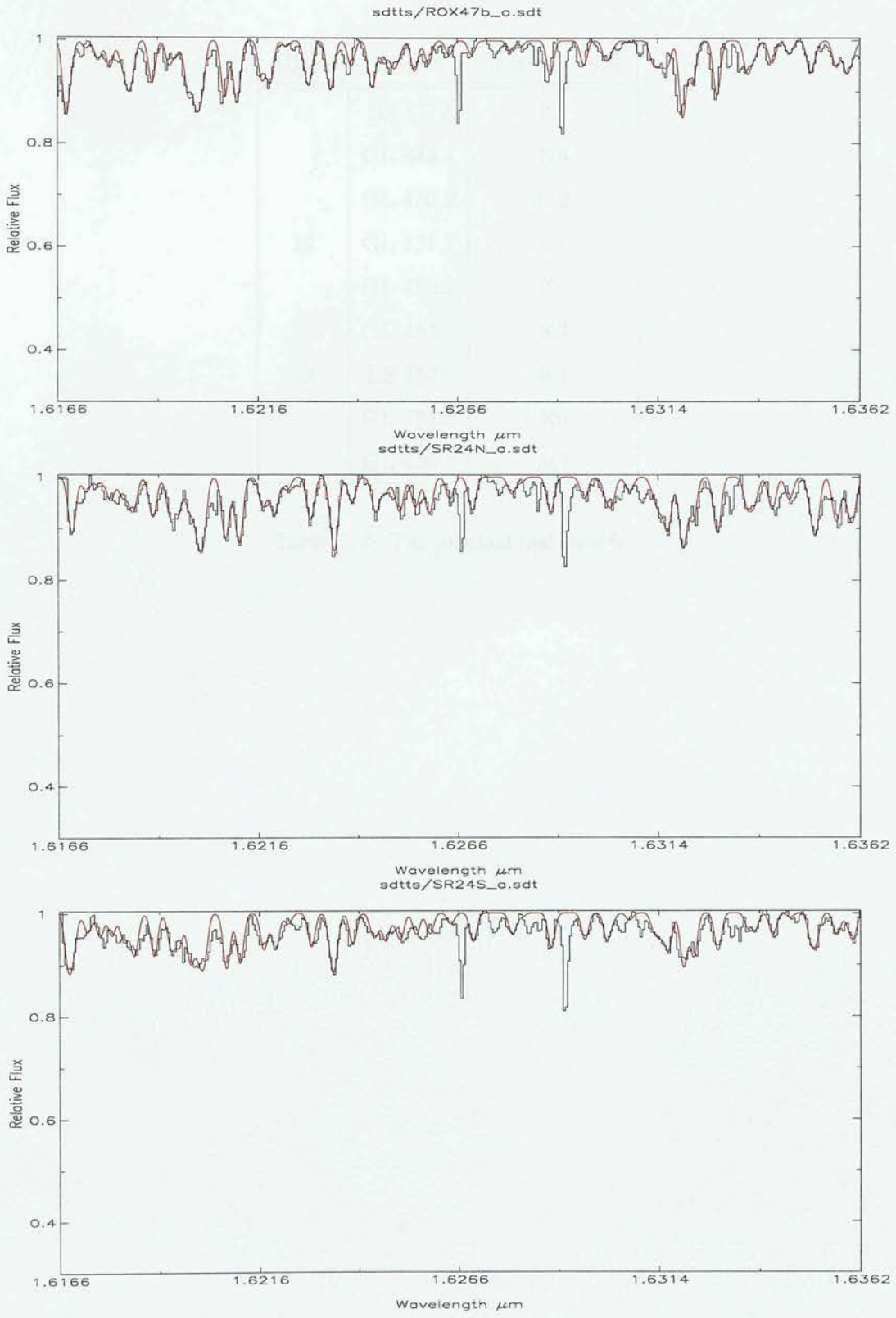

Figure A.10: ROXs 47b K3, SR 24n M0 and SR 24s K2

A.4 The misclassified dwarfs

Figure	Object	Spectral Type
11	BS 8372	K5
	GL 443.1	K3
	GL 459.2	M2
12	GL 471.1	K4
	GL 480.2	K4
	GL 484.1	K3
13	BS 7578	K3
	GL 454.3	K0
	GL 459.3	M2

Table A.4: The misclassified dwarfs

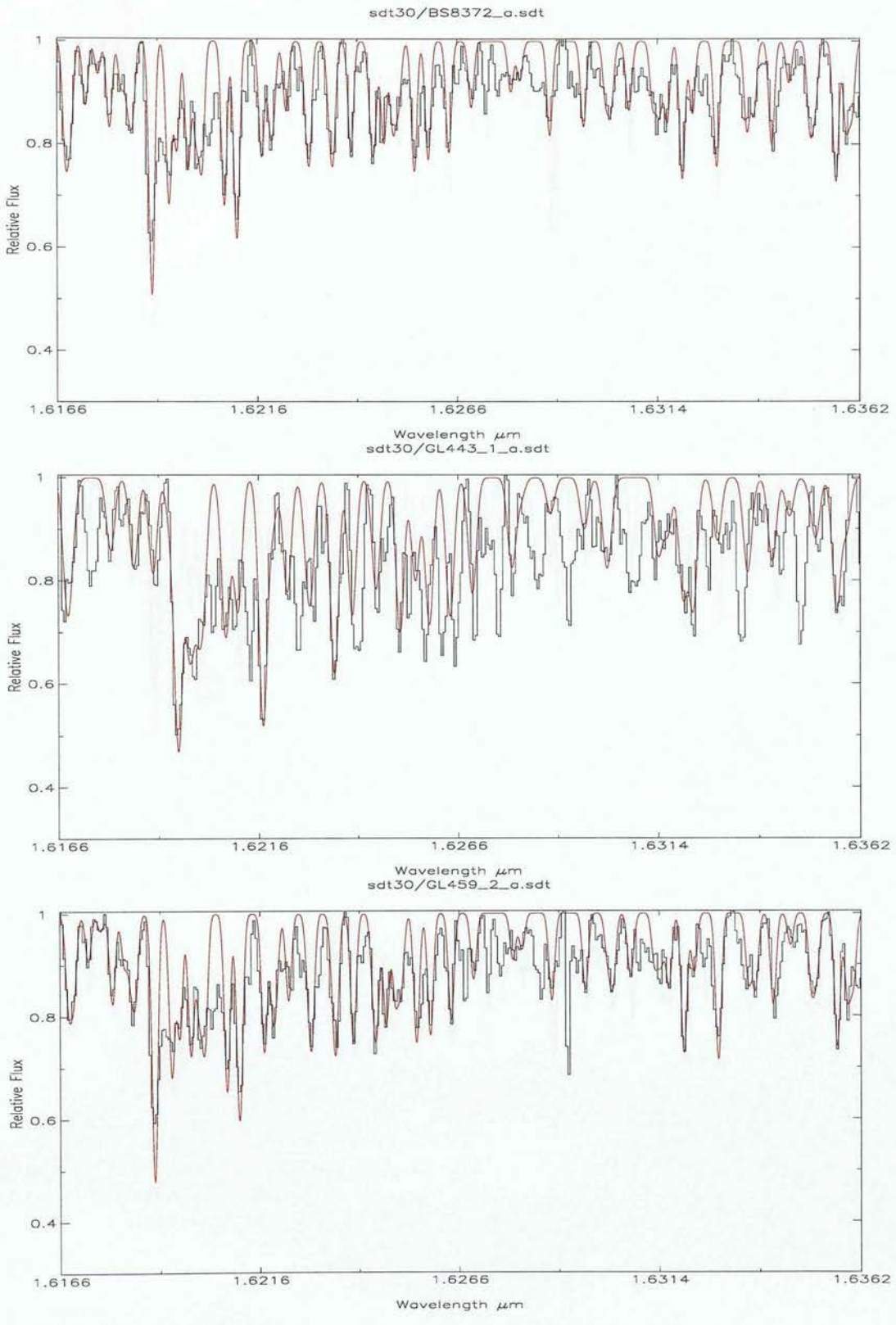

Figure A.11: BS8372 K5, GL443.1 K3 and GL459.2 M2

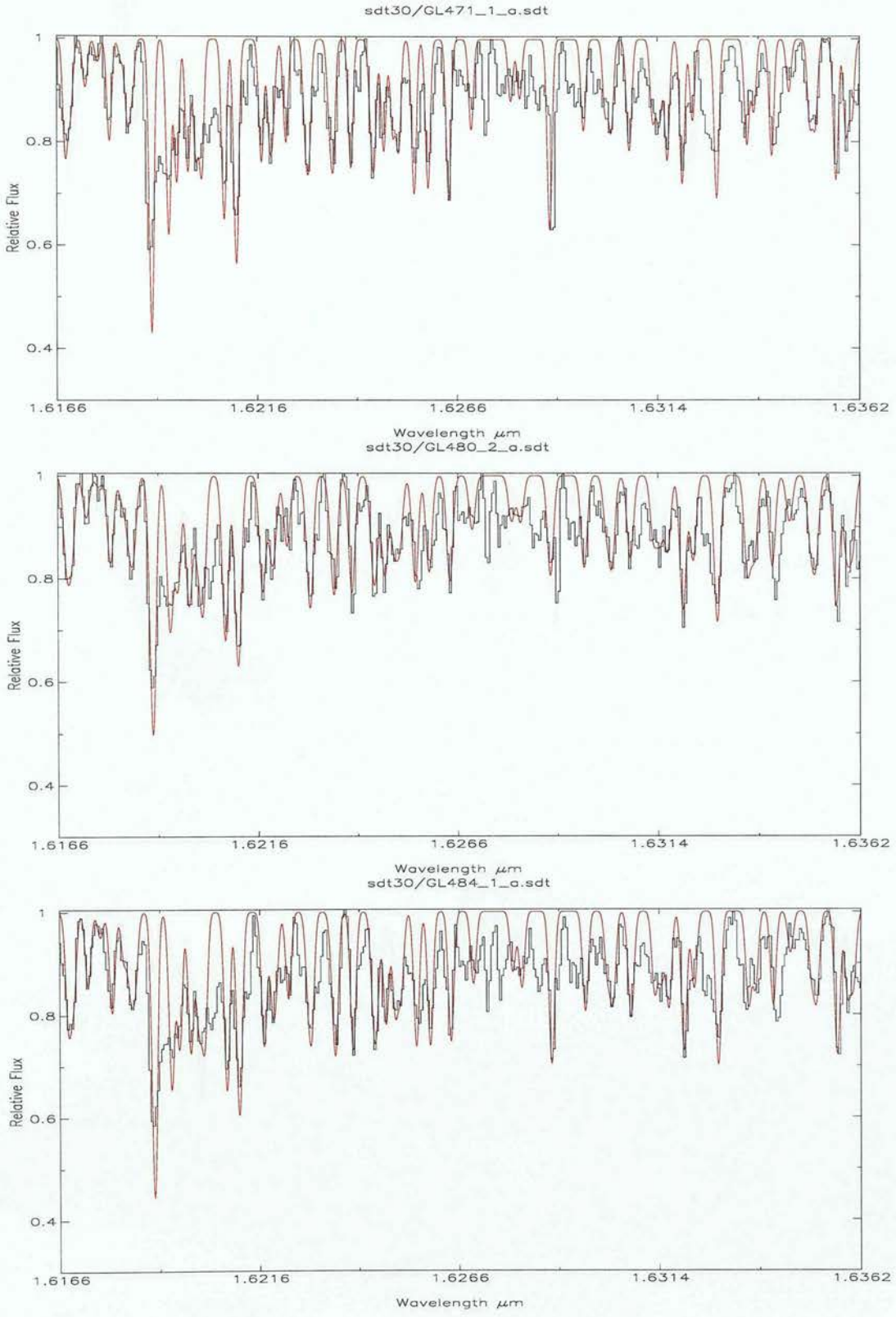

Figure A.12: GL471.1 K4, GL480.2 K4 and GL484.1 K3

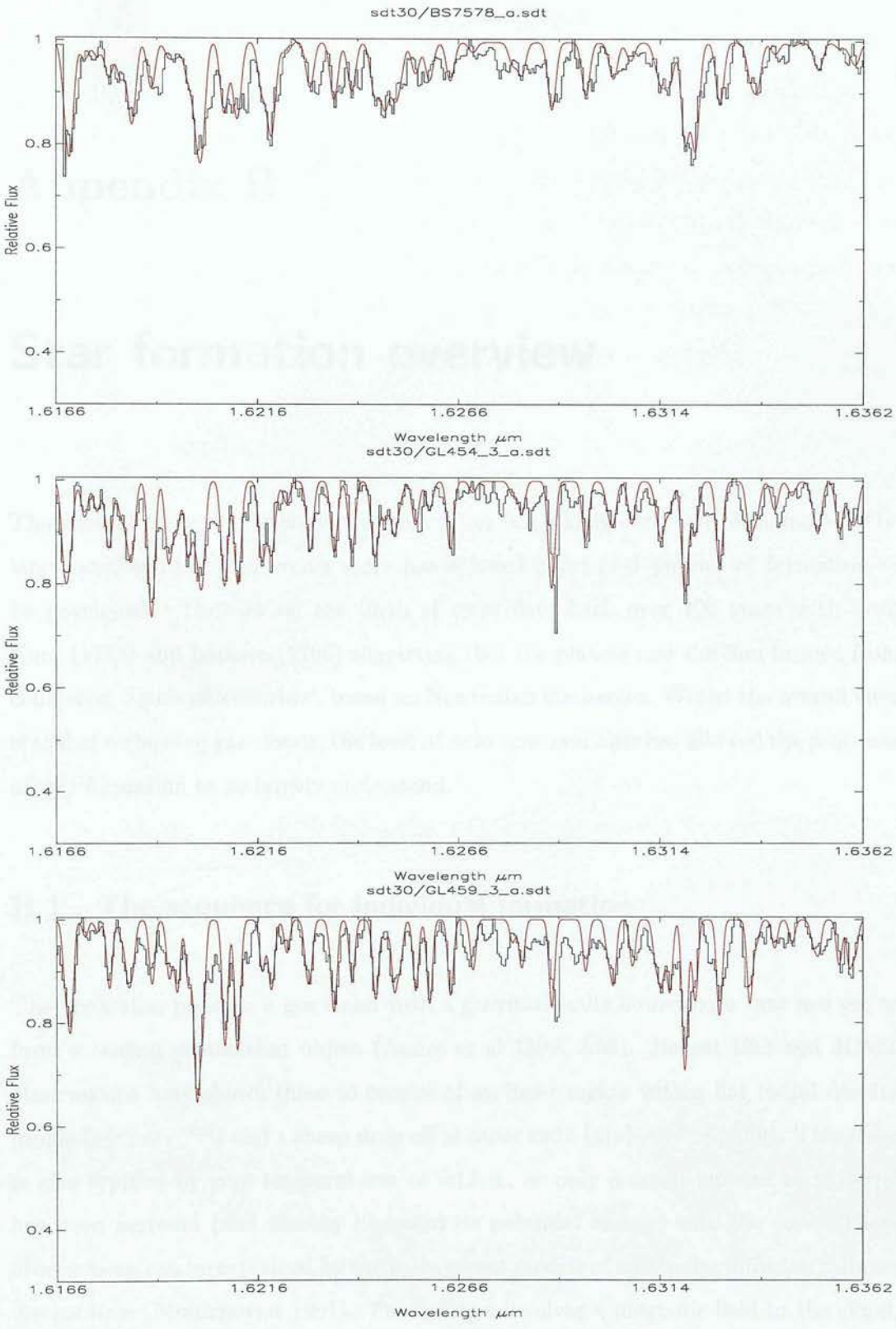

Figure A.13: BS7578 K3, GL454.3 K0 and GL459.3 M2

Appendix B

Star formation overview

The general process of galactic star formation is a widely observed phenomena. The large number of known young stars has allowed a detailed picture of formation to be developed. Theories on the birth of stars date back over 200 years with both Kant (1755) and Laplace (1796) suggesting that the planets and the Sun formed from collapsing clouds of 'elements', based on Newtonian mechanics. Whilst the overall view is still of collapsing gas clouds, the level of data now available has allowed the sequence of star formation to be largely understood.

B.1 The sequence for individual formation

The pre-stellar phase is a gas cloud with a gravitationally bound core that has yet to form a central protostellar object (André et al 1999, A99). Recent ISO and JCMT observations have shown these to consist of an inner region with a flat radial density profile ($\rho(r) \sim r^{-0.4}$) and a sharp drop off at outer radii ($\rho(r) \sim r^{-3}$) (A99). This stage is also typified by core temperatures of $\approx$13 K, as only a small amount of material has been accreted (and thereby liberated its potential energy) into the core. These observations can be explained by the more recent models of ambipolar diffusion collapse mechanisms (Mouschovias 1991). This process involves a magnetic field in the cloud, which partly prevents collapse, but allows slow infall of the neutral gas. Without the

magnetic support clouds, would collapse over a much shorter dynamical timescale, and would not be observed in the galaxy (Mouschovias 1991).

The next stage is the formation of a protostar itself, i.e. the core has a central object in near hydrostatic equilibrium. This is the "Class 0" stage, defined with the following observational properties: i) indirect evidence of a central young stellar object (YSO) e.g. a collimated CO outflow or an internal heating source, ii) centrally peaked but extended sub-mm continuum emission tracing the presence of a spheroidal circumstellar dust envelope (as opposed to just a disc), iii)High ratio of sub-mm to bolometric luminosity suggesting that the envelope mass exceeds the central stellar mass. This is equivalent to a spectral energy distribution (SED) resembling a black body of 15-30 K. (A99). Definition (iii) requires that most mass accretion will also occur during this stage, in conjunction with this the largest outflows (in terms of mass) are also seen from this stage of formation. Whilst these flows do not remove much material from the protostar it is believed that they are important in the extraction of angular momentum (Königl & Pudritz 1999), as otherwise the infalling material would spin up the star to rotational velocities that are not observed.

The viscosity in the circumstellar envelope causes the material surrounding the YSO to fall into a disc. This is due to friction within the cloud reducing velocities in all directions apart from that of the bulk angular momentum. Mass is then transferred from this disc to the protostar by the standard accretion process. In its simplest form this has a disc rotating in a near-Keplerian orbit, with friction between the orbits causing the material to slowly spiral inwards (Pringle 1981). Class 1 YSOs are evolved objects that still have some circumstellar shell material. The shell scatters and reprocesses the radiation from the disc and protostar into the infra red (I.R.), preventing direct optical observation.

By the time the shell has been depleted enough for the protostar to be visible in the optical, the protostar has accreted nearly all of its final mass. The definitions for Class 2 and Class 3 sources are normally applicable to low-mass protostars, also referred to as T Tauri stars (TTS). The accreted mass of these objects provides them with a large gravitational energy source, and they have photospheres, chromospheres and other

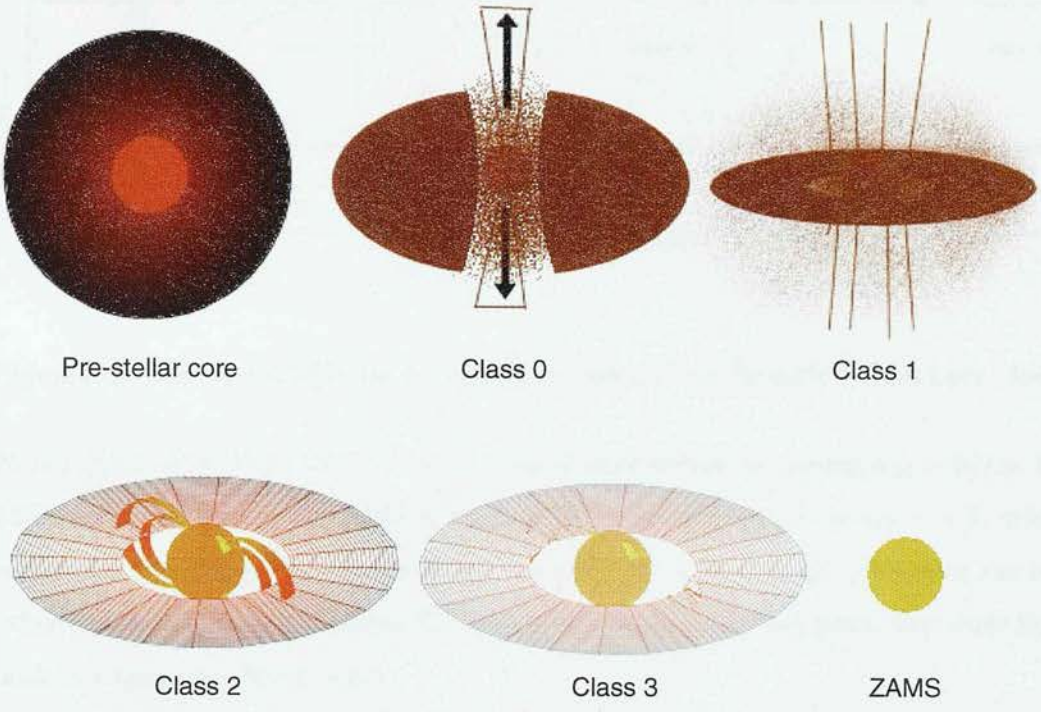

Figure B.1: The sequence of formation

stellar features similar to those seen in main sequence (MS) stars. Initially the observed protostars have radii 2 to 3 times the size of the equivalent MS stars (D'Antona & Mazzitelli, 1994), they contract in a near hydrostatic process, with radiation removing energy. As the stars contract the central temperature and pressure are high enough for Lithium and Deuterium burning to occur. Once Hydrogen burning has started, and supports the star is in hydrostatic equilibrium, the star is regarded as being Zero Age Main Sequence (ZAMS).

B.2 The spectral energy distribution (SED)

The first I.R. observations of star forming regions led to a classification system that was based on the spectral energy distribution (wavelength×flux vs. wavelength) of the stars.

This spectral index is defined as $\alpha_{\rm IR} = d\log(\lambda F_\lambda)/d\log\lambda$ between λ=2.2 and 10-

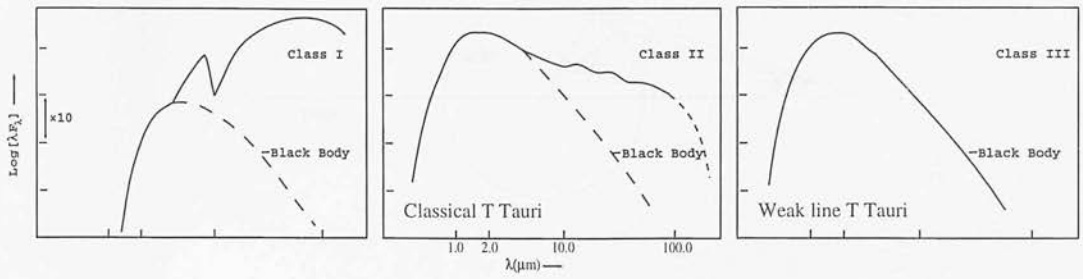

Figure B.2: The typical SEDs for the last three classes of star formation, from Lada (1988)

25 μm (Lada & Wilking 1984). Class 1 sources were defined as having $\alpha_{\rm IR} > 0$, i.e. the SED increases towards the mid-I.R.. Class 3 sources are defined as $\alpha_{\rm IR} < -2$, which represents a reddened black body. Class 2 sources are defined as lying between the two other classes, i.e. they have some I.R. excess compared to a black body, but their SED peak is $<1\mu$m (see figure B.2).

This excess in the I.R. is thought to be due to the circumstellar discs of the system, Lynden-Bell & Pringle (1974). The exact form of the SED provides information about the shape and temperature of the disc.

B.2.1 A passive disc.

If a star is surrounded by a sheet of optically thick black body material in Keplerian orbits, the temperature distribution of that disc will be governed by the amount of flux it receives from the star. The following is the maths for the temperature distribution. Figure B.3 shows the model of the system.

If a unit area is considered on one side of the disc at distance r, from a star of radius R, then the flux absorbed by that area is:

$$F(r) = \pi I \int_0^{\arcsin(\mathrm{R}/r)} \sin^2\phi d\phi = \frac{\pi I}{2}\left[\arcsin\frac{\mathrm{R}}{r} - \frac{1}{2}\sin\left(2\arcsin\frac{\mathrm{R}}{r}\right)\right] \qquad \text{(B.1)}$$

Where $\pi I = \sigma \mathrm{T}_*^4$ following Stefans' law. The $\arcsin(\mathrm{R}/r)$ term in the integral is from the increase in the area of the stellar surface observed as ϕ increases. The temperature

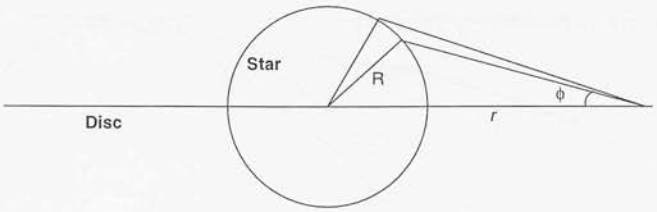

Figure B.3: The geometry of the modelled system

distribution of the disc is then calculated by using:

$$\mathrm{T}(r) = \left(\frac{\pi F(r)}{\sigma}\right)^{\frac{1}{4}} \tag{B.2}$$

So equation (B.1) and equation (B.2) can be combined to give:

$$\mathrm{T}(r) = \mathrm{T}_* \left(0.5 \arcsin\frac{\mathrm{R}}{r} - 0.25 \sin\left[2 \arcsin\frac{\mathrm{R}}{r}\right]\right)^{\frac{1}{4}} \tag{B.3}$$

The SED of this disc can then be calculated if each annulus is assumed to radiate as a black body, using:

$$\lambda \mathrm{F}(\lambda) = \frac{4\pi \mathrm{hc}^2}{\lambda^4} \int_{\mathrm{R_{in}}}^{\mathrm{R_{out}}} \frac{r}{e^{\frac{\mathrm{hc}}{\mathrm{kT}(r)\lambda}} - 1} dr \tag{B.4}$$

This equation is also used for calculating the SED of the accretion disc with equation (B.5).

The luminosity of this disc causes the SED to change as shown in figure B.4. Unfortunately there is a limit to the $\alpha_{\mathrm{I.R}}$ that this reheating can produce, but extra heating of the disc can be gained if it is presumed to be viscous.

B.2.2 An accretion disc

If the disc material is dense enough to be viscous, friction will cause it to fall towards the star (some of the potential energy lost is liberated as the extra luminosity), eventually adding to the mass of the star, this is an accretion disc. The equation governing the temperature distribution of an accretion disc, from Pringle (1981) is:

$$\mathrm{T}(r) = \left(\frac{3\mathrm{GM}\dot{m}}{8\pi\sigma r^3}\left[1 - \sqrt{\frac{\mathrm{R}}{r}}\right]\right)^{\frac{1}{4}} \tag{B.5}$$

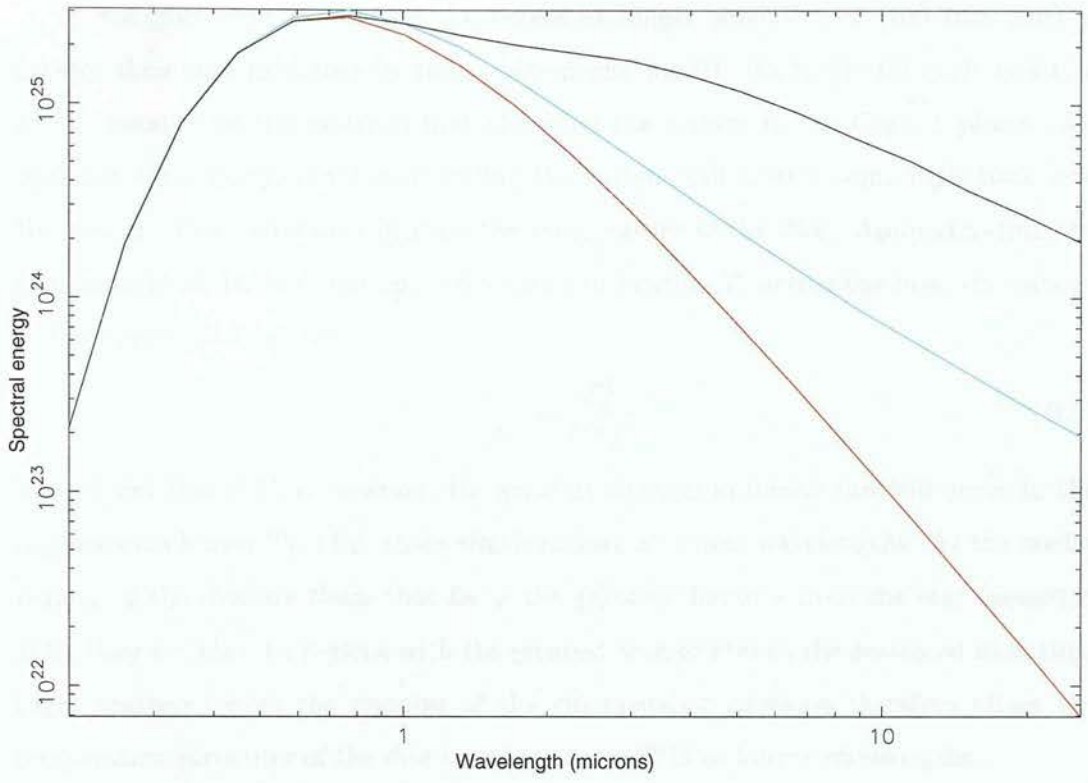

Figure B.4: The theoretical SEDs for a black-body (red), a passive disc with black-body (cyan) and active disc with black-body (black).

Where G and π are the usual constants, σ is the Stephan-Boltzman constant and $\dot{m}$ is the mass accretion rate.

Figure B.4 shows the SED of this when combined with equation (B.4). The SED produced has a variable $\alpha_{\text{I.R.}}$, dependent on M and $\dot{m}$, as seen in observations.

Subtle changes in the SED have also been interpreted as features in the circumstellar material. Meyer, Calvet & Hillenbrand (1997) showed that the near-I.R. excess predicted by accretion disc models is larger than that observed in Class 2 objects. This is explained with the inclusion of a gap between the star and the disc, of order a few stellar radii. As this would be the hottest part of the disc (equation B.5), it radiates at the shortest wavelengths. Such a gap is also invoked in the current models of mass transfer between the disc and the star (see next section).

It has also been found that the excess at longer wavelengths (100-1000 μm) is greater than that predicted by the accretion disc model. Natta (1993) explained this as the remains of the material that shrouded the system in the Class 1 phase. An optically thin, dusty, cloud surrounding the system will scatter some light back into the system, this radiation will raise the temperature of the disc. Approximating the system to black-body radiation, and a constant heating T_e across the disc, the change in luminosity, ΔL will be:

$$\frac{\Delta L}{L} = \frac{T_e^4}{T(r)^4} \tag{B.6}$$

This shows that if T_e is constant, the greatest changes in luminosity will occur in the regions with lowest $T(r)$ i.e. those which radiate at longer wavelengths. As the cooler regions of the disc are those that lie at the greatest distance from the star (equation B.5), they are also the regions with the greatest area to absorb the scattered radiation. Light scattered from the remains of the circumstellar envelope therefore alters the temperature structure of the disc to enhance the SED at longer wavelengths.

B.3 General features of Classical T Tauri Star accretion

Class 2 objects, with are often Classical T Tauri Stars (CTTSs), display many high-energy features. Large Hydrogen Balmer emission lines are seen in CTTSs along with a continuum emission in the optical region. Both of these indicate high temperature regions ($\approx$10000 K) on the stars. Detailed analysis of the lines (Muzzerolle, Calvet & Hartmann 1998) has shown that they are formed during infall of material. These observations are thought to be the fingerprints of the inner-most stage of accretion, where material from the disc is transferred onto the star.

One of the most complete models for the accretion process so far developed is that of Shu et al (1995 and previous), which has many similarities with other models, such as that of Königl (1991). The models have the following features:

1. the disc is modelled as a 'thin' accretion disc i.e. the vertical structure does not affect the accretion process.

2. the magnetic field of the star is strong enough to stop accretion of ionized material at the co-rotation radius (where the Keplerian orbit has the same period of rotation as the stellar surface) typically 3 R_*.

3. material is then channeled in the direction of the magnetic field, eventually free-falling onto the stellar surface in a column or ring (see figure B.5)

4. the strong magnetic fields result in strong stellar winds and flare activity

5. outflows (jets) result from material outside the co-rotation radius flowing in the direction of unbound magnetic fields.

6. the angular momentum of the infalling material is transfered to the disc, and is carried away from the star by normal accretion.

Whilst these models do not take account of all observed features, most notably the shape of the disc and variable accretion rates, they explain many observations (Chandler & Richer 1999).

- The accretion disc with gap will produce the I.R. SED as previously discussed.
- The channelled infalling gives the features seen in the shapes of the Hydrogen Balmer lines.
- The confining of accretion to free-fall rates over small areas of the stellar surface will produce shock-fronts resulting in the high temperature emission seen in the optical continuum (Hartigan et al. 1990).
- The stellar winds and flares are seen as short time scale variability in the optical emissions lines and X-ray data (Herbst, Herbst & Grossman, 1994, Smith et al. 1999).
- The jets are observed from many CTTSs, mainly as Herbig-Haro objects, bow shocks within the jets, Reipurth et al (1997) have shown that these are far more collimated than was previously thought.
- The transfer of angular momentum to the disc also accounts for the relatively slow rotation rates of CTTSs. It was originally thought that CTTSs must rotate at

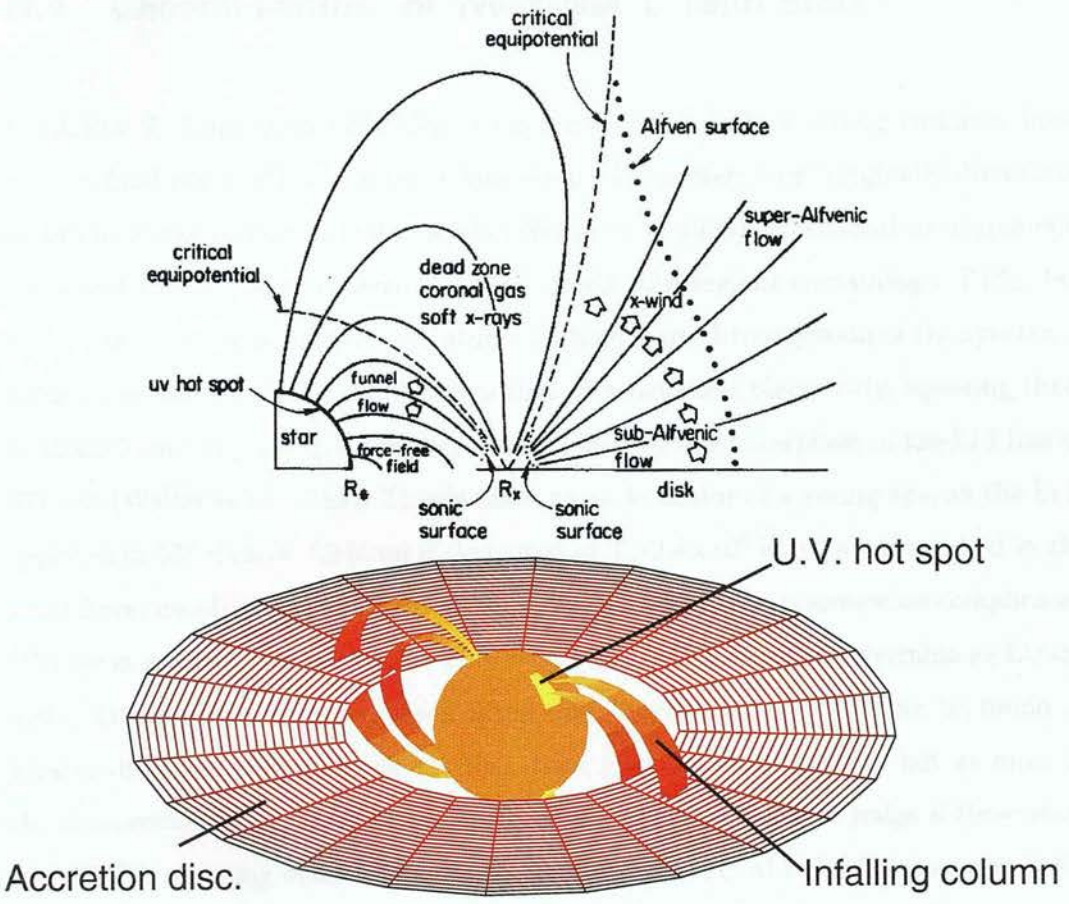

Figure B.5: Two schematic diagrams for the magnetospheric CTTSs model. The upper diagram is from Shu et al. 1994

their breakup-rate (where the kinetic energy of particles on the equator surface equals their potential energy), due to the angular momentum being added by infalling material. Observations have now shown it is in fact WTTSs that have high rotation rates, of order a few days, due to the contraction of the star as it approaches the main sequence, whereas CTTSs have rotation rates on the scale of a week (Shevchenko & Herbst 1998).

B.4 General features of Weak-line T Tauri Stars

Weak-line T Tauri stars (WTTSs), named after their lack of strong emission lines, are the final stage of low mass star formation. These stars were originally discovered as bright X-ray sources in dark clouds (Walter et al 1988). Positional measurements suggested that the sources were stars associated with regions containing CTTSs, but with none of the bizarre spectral features of those stars. Investigation of the spectra of these stars showed that their SED was that of a reddened black-body, equating them to Class 3 sources, and that the only unusual feature was absorption in the Li I line at 671 nm (Walter et al. 1988). This is taken as an indicator of a young age, as the Li is depleted in MS dwarfs. Lithium is destroyed at T>2.4×10^6 K, which is reached in the central regions of developed TTSs, although the actual process is somewhat complicated (Walter et al 1988, Duncan 1981). This means that it is difficult to determine an Li/age scale. Observations have now been made that suggest that WTTSs can be found at greater distances from dark clouds than their younger counter-parts, but as most of the measurements are based on X-ray observations it is difficult to judge if these stars are WTTSs or young main sequence objects (Terranegra et al 1999, Briceno et al 1997, Martín 1998). Combining the results of these papers suggests that WTTSs can be found in groups around dark clouds, and that they formed in an earlier phase of star formation than that which is currently observed. For further discussion see Chapter 1.

B.5 Post T Tauri stars

Many authors use the term 'Post T Tauri star' or PTTS to refer to evolved WTTSs. The main purpose of this (as described by Martín 1998) is to distinguish between comparatively young stars that are found within dark clouds and have just finished their CTTS phase, and the stars that can be found outside the dark clouds, and as such are older and more evolved. The suggested cut-off between WTTSs and PTTSs is the strength of the Li 671 nm line. In this thesis have referred to all low mass pre-main sequence stars either as CTTSs or WTTSs. This is because there is no detectable change in the physical processes within the star from the WTTS phase to ZAMS.

Deuterium burning does occur in stars before the ZAMS stage, but there is currently no way of detecting when this happens. The PTTS definition is a mass dependent factor that attempts to quantify when a young star is no longer thought of as being 'young' and is not related to an actual change within the star.

Appendix C

Variability and a vanishing YSO in the Serpens cloud core

(This work has been published as Horrobin, Casali & Eiroa 1997)

C.1 Abstract

This letter compares data from a recent near-IR study of the Serpens cloud core with data from previously published studies. It is found that one object, irs 81 has completely vanished, fading by more than 3.8 magnitudes at K, while a total of 10 of the observed objects have varied by over 0.5 magnitudes in H or K, with little change in colour. We have also discovered 13 new objects in the cloud core which were below the magnitude limit of previous studies.

C.2 Introduction

The small–amplitude photometric variability of T Tauri stars has been studied for some years, and appears to be caused by hot and cold starspots (e.g. Bouvier et al. 1988;

Fernandez & Eiroa, 1996), while larger amplitude variations might be attributable to the circumstellar environment, as in RY Lup (Gahm et al 1989). However, much less is known about the variability of embedded young stellar objects (YSO's) because these require studies to be made at infrared wavelengths, for which instrumentation is still relatively uncommon - at least on small telescopes. Yet evidence for quite strong variability in the near infrared has been found in NGC1333 SSV 13 (Aspin & Sandell 1994) and B5 irs1 (Moore & Emerson 1994) for example. Some variability appears to be in the form of outbursts, as in the companion to T Tauri (Kobayashi et al. 1994). Indeed embedded YSOs, with their larger quantities of circumstellar gas and dust, might be expected to show large photometric variations. Fortunately, with the development of infrared detector arrays, and given the compact nature of many embedded clusters, studies of infrared variability can now be conducted efficiently.

The Serpens molecular cloud core is a well studied star forming region, 310 pc distant (de Lara et al 1991), containing many YSO's at various evolutionary stages. In a recent study by Eiroa and Casali (1992, hereafter EC) over 160 objects were found in the near-IR, 51 of which were identified as being members of the cluster. Recently, Hodapp (1995) discovered a dramatic brightening of one of the young stars in the cluster, and associated it with an FU Ori type of event. In an attempt to search for variability in other YSO's we decided to re-image the area around the main nebulosity in the near-IR, and compare the results with EC (taken 6 years previously).

C.3 Observations and results.

The new observations were made on May 1, 1995 on the United Kingdom Infrared Telescope (UKIRT) using IRCAM3 which uses a 256×256 InSb array, at $0''.3$ per pixel resolution. The observations consisted of 5 frames in each of the H and K bands; 4 of which were overlapping. The results presented in EC were obtained with the same telescope, but using the first generation infrared camera (IRCAM), during April 1988 and May 1989. The new data cover roughly 7.5 arcmin^2, which corresponds to a subset of the field covered in EC. In total, 35 stellar objects were seen by both studies.

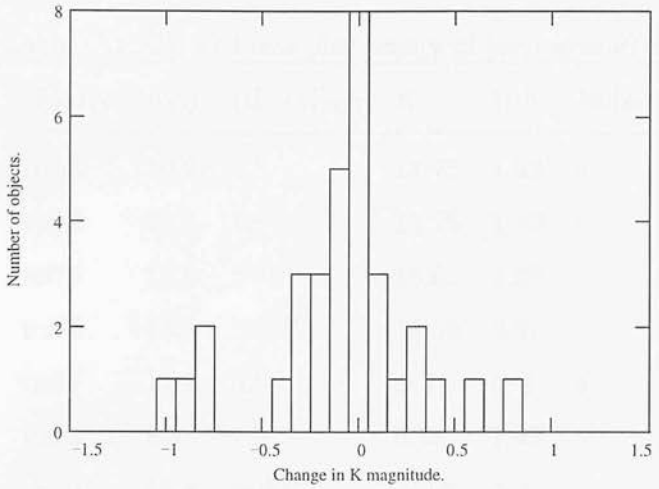

Figure C.1: The histogram of ΔK for the comparison between the new data and that from EC, for a sample of 35 stellar objects.

Data reduction proceeded in the normal way. Flat-fields were obtained on a nearby sky position. Since there was bright structured reflection nebulosity in the regions of overlap between frames, we were able to carry out both a zero-point and transparency correction for four of the frames. Final photometric reduction of point sources was achieved using the STARLINK package PHOTOM with a software aperture of 5″. Standard star observations were used to calculate apparent magnitudes. The magnitude limits of the new observations are 18.0 at J and 16.0 at K.

A histogram of the K magnitude differences between the old and new data set was calculated and showed that most sources had minimal variability. However, the median of the magnitude differences was not zero, but 0.1 magnitudes. Since it seems unlikely that any variability would be coordinated over the cluster, it was concluded that this probably represented a systematic error in the photometry. With this assumption, the magnitudes of the YSOs in the new data were calibrated by making their median magnitude the same as that for the photometry in EC. Use of the median (rather than a mean) ensures that a few strongly variable sources do not significantly effect the photometric calibration. The histogram of K data resulting from this calibration is shown in figure C.1.

The estimated random errors in the new photometry were 0.03 magnitudes for the

Table C.1: Old and new photometry of varying sources

Source	K_{EC}	$(H-K)_{EC}$	K	H-K	Notes
irs53	10.9	1.8	11.75	1.53	a
irs73	12.5	1.6	11.76	1.30	a
irs75	15.9	> 0.1	15.01	1.87	
irs76	15.3	> 0.7	14.50	2.87	
irs81	12.2	0.6	> 16	> 1	a
irs82	8.8	1.5	9.34	1.49	a
irs101	13.4	> 2.6	> 16	> 1	
irs102	15.4	> 0.6	> 16	> 1	
irs103	12.3	1.9	11.31	1.87	a
irs104	14.8	> 1.2	> 16	> 1	

Notes: a - objects associated with Serpens cloud core by EC.

fainter sources (given by PHOTOM), while EC quote an accuracy of 0.1 magnitudes. Unfortunately, most of the sources lie on fairly bright background nebulosity, and it is difficult to determine if the local background used for a source in this survey is the same as that used in EC due to centroiding differences and differences in pixel size. We therefore chose to be conservative and defined variable objects as those that showed a difference of greater than 0.5 magnitudes (5σ) between the old and new photometry. Table C.1 shows the list of varying objects under this criterion, where source numbers refer to the classification in EC. Tests using different sky and sources apertures allow us to be very confident that these are indeed variable sources.

14 previously uncatalogued objects were also discovered in the new data, all but one of which have magnitudes fainter than the survey limit of EC. Unfortunately, with only H and K data it is not possible to say with certainty whether or not they are connected with the cloud core. Most are not very red which, given the extinction through the core, may mean they are foreground objects. For the sake of future studies, including ongoing ISO observations, we give their positions and magnitudes in table C.2. Many of these objects are at the magnitude limit of this study, so their magnitudes will have random errors approaching 0.2 mags.

Table C.2: New sources

Source	R.A. 18^h27^m	Dec. 1°	H	K	
irs164	$21^s.6$	12′28″	16.8	16.8	
irs165	21.7	12′33″	16.5	15.8	
irs166	21.9	12′40″	16.4	15.6	
irs167	22.7	10′31″	17.5	16.3	
irs168	22.9	10′36″	17.8	16.6	
irs169	24.2	13′27″	17.9	16.5	
irs170	24.4	11′13″	> 18	16.4	possible
irs171	24.4	11′17″	> 18	16.5	binary
irs172	24.5	13′40″	17.3	16.4	
irs173	24.7	13′36″	17.1	15.7	
irs174	24.8	10′55″	> 18	16.7	
irs175	26.6	10′20″	> 18	15.6	
irs176	27.3	13′47″	17.2	15.8	
irs177	28.1	11′42″	> 18	16.6	

Irs81 is the most interesting object in this study. Despite being a bright source in the EC survey, it has completely disappeared in the new data - a dimming of at least 3.8 mags. in K. Figure C.2 shows an image of the surrounding field - irs81 is clearly absent in the new data. A further K frame was taken on March 11 1996 through the UKIRT service programme, and confirms the disappearence. All that is seen in the new image is an area of nebulosity no brighter than nearby parts of the main reflection nebula. Three other objects, listed as YSOs by EC (irs101, irs102 and irs104) also seem to have vanished as point sources although they are clearly associated with small areas of nebulosity in the new data, with no apparent bright central sources.

An interesting object seen in both the new data and in EC is irs88, one of the sources in the SVS4 Southern sub-cluster. Originally only K data was available, but the new data give K=11.9 and H-K=5.5, making it more than twice as red as anything

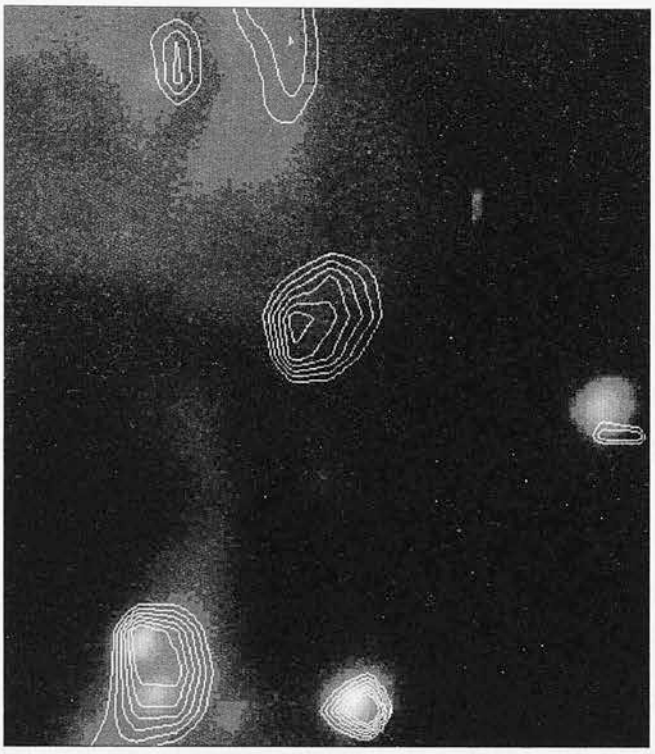

Figure C.2: The area centred on irs81. The greyscale image is from the service observations of this year and the contours are from the original data of EC. Irs81 has vanished in the recent greyscale image.

else in this study.

C.4 Discussion

If the photometric changes represent changes in circumstellar extinction, then a normal reddening law would also result in changes in H-K colour given by $\Delta(\mathrm{H}-\mathrm{K}) = 0.7A_{\mathrm{K}}$ where A_{K} is the K band extinction. But of the variable YSOs that have H and K photometry in both studies (irs53, 73, 82 and 103), the variability is consistent with being grey within the errors ($\Delta(\mathrm{H}-\mathrm{K}) \approx 0$). Thus the changes are not simply the result of changes in reddening. Grey variability has been observed before, with several different models being proposed to explain it. Voshchinnikov and Grinin (1991) have observed large grey variability in the Ae/Be star WW Vul; they suggested that this was

in the main part due to large opaque dust clouds (≈0.01 AU) obscuring the star. The variability seen in this study is on a smaller scale, corresponding to a 30% change in the flux from the object in the line of sight, so if clouds are to serve as an explanation they would have to be smaller than those suggested by Voshchinnikov and Grinin, while remaining optically thick in the H and K bands (to ensure greyness). Moore and Emerson (1994) have also observed grey variations from J to K, although there were colour changes in the L,L' and nbM bands. They explain their results as due to a depletion of small dust grains (compared to the interstellar medium), resulting from coagulation. Either of these models could explain the variability we observe in the four YSOs with H-K data from both studies.

The disappearance of irs81 is more difficult to explain. In the original EC survey it appears as an extended object $\approx 5''$ across, on the edge of the nebulosity associated with SVS20. It is also worth noting that irs81 lies only $18''$ from the sub-mm source SMM4 (Casali et al 1993), but we have no evidence that the two are physically associated. We know of no other example of a nebulous YSO in a star forming region fading as dramatically as this one, although other nebulae have been observed to vary. Hubble discovered that the fan nebula NGC 2261, now known to be associated with the young star R Monocerotis, varies significantly. Lightfoot (1989) suggests that this variability is due to clouds around the young star casting shadows on the nebulosity. If this model were to apply in the case of irs81, it would mean that the central source has now become completely obscured.

C.5 Conclusion

We have found that 28% of observed YSO's in Serpens have varied by >0.5 mags. in the near–IR over a timescale of six years. In those objects with both H and K data, the variations are consistent with being grey. In one object in particular, irs81, a fading by over 3.8 magnitudes has made it vanish altogether.

Appendix D

Glossary

Class 0,1,2,3 Classes of young stellar objects based on the slope of the SED between 2.2 and 10-25 μm (section B.2). Class 0 does not have such a strict definition (section B.1), but the name was given as it is thought to represent the stage before Class 1.

CSF The Companion Star Fraction, the number of companion stars divided by the number of systems in a region.

CTTS Classical T Tauri Star, a T Tauri star with E.W. H$\alpha > 5$ Å.

E.W. Equivalent Width, the width of the spectral continuum with the same area as a spectral line. Negative for absorption, positive for emission.

FWHM Full Width Half Maximum, the width of a distribution at half its peak value.

g, surface gravity Free fall acceleration at the surface of an object.

H-R Hertzsprung-Russell diagram, a graph of log (luminosity) against log (T_{eff}), or equivalent parameters. Distinguishes between stars with differing structures.

IMF Initial Mass Function, the initial distribution of stellar masses required to account for all the stellar objects in an observed region.

I.R. Infra-Red, the region of the electro-magnetic spectrum between 1-300 μm.

LDR Line Depth Ratio, a ratio of the depths of selected absorption lines in a spectrum. Independent of veiling and broadening.

MF Mass Function, the distribution of masses for an observed selection of stars.

MS Main Sequence (stars), stars which derive all their luminosity from hydrogen fusion in their cores. Seen as a diagonal strip in the H-R diagram.

MST Multiple Spectral Type (stars), stars which display various spectral types, depending on which spectral features are chosen for classification.

PSF Point Spread Function, the distribution of flux from a point source on telescope detectors.

r, veiling The ratio between the excess flux and photospheric continuum in CTTSs. The excess is formed by accretion activity, and results in absorption lines appearing shallower or veiled.

SED Spectral Energy Distribution, a graph of wavelength×flux vs. wavelength.

T_{eff} The temperature of a black-body which radiates with the same energy per unit area as an object.

τ, **optical depth** Given by $I_\lambda = I_\lambda^0 \mathrm{e}^{-\tau_\lambda}$, where I_λ is the intensity of light transmitted after I_λ^0 has passed through a partially transparent material, ignoring emission.

TTS T Tauri Star, a class of young, low mass, stars, covers G to M spectral types.

U.V. Ultra-Violet, the region of the electro-magnetic spectrum approximately between 91.2-350 nm.

WTTS Weak T Tauri Star, a T Tauri star with E.W. Hα < 5 Å.

YSO Young Stellar Object, any type of stellar or protostellar object which has yet to reach the main sequence.

ZAMS Zero Age Main Sequence (star), stars which have just begun to be supported by hydrogen fusion in their cores.

Appendix E

References

Alcalá, J.M. et al, 1995, A&AS 119, 7

Alcalá, J.M. et al, 1997, A&A 319, 184

Alexander, D., Augason, G. & Johnson, H., 1989, ApJ 345, 1014

André, P., Ward-Thompson, D. & Barsony, M. 1999, "Protostars & Planets IV" eds. V. Mannings, A.P. Boss & S.S. Russell, Univ. of Arizona Press

Aspin C, Sandell G., 1994, A&A 288, 803

Basri, G., Marcy, G. & Valenti, J., 1992, ApJ 390, 622

Basri, G., Wilcots, E. & Stout, N., 1989, PASP 101, 528

Bodenheimer, P., 1995, ARA&A 33, 199

Bouvier, J. & Appenzeller, I, 1992, A&AS, 92, 481 (BA)

Bouvier J., Bertout C., Bouchet P. 1988, A&AS, 75, 1

Bouvier J. et al, 1995, A&A, 299, 89

Bouvier J. et al, 1997, A&A, 318, 495

Brandner, W. & Zinnecker, H., 1997, A&A 321, 220

Briceño, C. et al, 1997, AJ 113, 740

Calvet, N. & Gullbring, E., 1998, ApJ 509, 802

Canuto, V. & Mazzitelli, I., 1992, ApJ 389, 724

Cardelli, J., Clayton, G. & Mathis, J., 1989, ApJ 345, 245

Carr, J., 1995, Ap&SS 224, 25

Casali, M., Eiroa, C., Duncan, W. 1993, A&A 275, 195

Chandler, C. & Richer, J., 1999, "Astrophysical Discs - An EC Summer School", ASP Conf. Series 160, Eds. Sellwood, J. & Goodman, J.

Cohen, M. & Kuhi, L., 1979, ApJS 41, 743

Comeron, F., Rieke, G. & Rieke, M., 1996, ApJ 473, 294

D'Antona, F., & Mazzitelli, I., 1994, ApJS, 90, 467

Daly, P.N., 1995, Starlink User Note 27.4

de Jager, C. & Nieuwenhuijzen, H., 1987, A&A 177, 217

de Lara E.,Chavarria-K C., López-Molina G., 1991, A&A 243, 139

Dorren, J. & Guinan, E., 1990, ApJ 348, 703

Doyle, J. et al., 1989, A&A 223, 219

Drinkwater, M & Holman, B., 1996, FLAIR Data Reduction with IRAF (AAO)

Duncan, D.K., 1981, ApJ 248, 651

Edwards, S., Hartigan, P., Ghandour, L. & Andrulis, C., 1994, AJ 108, 3

Eiroa C.,Casali M., 1992, A&A 262, 468

Favata, F., Micela, G., Sciortino, S. & D'Antona, F., 1998, A&A 335, 218

Fernandez, M., Eiroa, C. 1996, A&A 310, 143

Finkenzeller, U. & Basri, G., 1987, ApJ 318, 843

Foukal, P., 1998, ApJ 500, 958

Gahm, G.F., Fischerstrom, C., Liseau R., Lindroos, K.P. 1989, A&A, 211, 115

Ghes, A., McCarthy, D., Patience, J. & Beck, T., 1997, ApJ 481, 378

Ghez, A., White, R., & Simon, M., 1997, AJ , 490, 353

Gray, F., 1992, "The observation and analysis of stellar photspheres." Cambridge Astrophysics Series

Gray, F. & Johanson, H., 1991, PASP 103, 439

Greene, T.P. et al., 1994, ApJ 434, 614

Greene, T.P., Lada, J.L., 1996, AJ 112, 2184

Greene, T.P., Meyer, M.R. 1995, ApJ 450, 233

Guenther, E.W. et al., 1999, A&A 341, 768

Gullbring, E., Hartmann, L., Briceño, C. & Clavet, N., 1998, ApJ 492, 323 (GHBC)

Hauschildt, P., Allard, F. & Baron, E, 199, ApJ 512, 377

Hartigan et al., 1990, ApJ 354, L25

Hartigan, P., Hartmann, L., Kenyon, S. & Hewett, R., 1989, ApJ 70, 899

Hartigan, P., Strom, K. & Strom, S, 1994, ApJ 427, 961

Hartmann, L., Hewett, R. & Calvet, N., 1994, ApJ 426, 699

Hatzes, A., 1995, ApJ 451, 784

Herbig, G., 1962, ApJ 135, 736

Herbig, G. & Bell, K., 1998, Third Catalog of Emission-Line Stars of the Orion Population, Lick Observatory Bull. No. 1111

Herbst, W., Herbst, D, Grossman, E & Weinstein, D., 1994, ApJ 108, 1907 (HHGW)

Hodapp, K., 1995, IAU Circular no. 6186

Horrobin, M., Casali, M. & Eiroa, C., 1997, A&A 320, L41

Hughes, J., Hartigan, P., Krautter, J. & Kelemen, J., 1994, ApJ 108, 1071

Jaschek, C. & Jaschek, M, 1987, "The Classification of Stars", Cambridge Univ. Press

Johns-Krull, C. et al., 1999, ApJ 510, L41

Joncour, I., Bertout, C. & Bouvier, J., 1994, A&A 291, L19

Jones, H., Longmore, A., Allard, F & Haushildt P., 1996, MNRAS 280, 77

Kant, I., 1755, Universal Natural History and Theory of Heaven, translation by Ian C. Johnstone (www.mala.bc.ca/~johnstoi/kant1.htm)

Kenyon, S., Dobrzycka, D. & Hartmann, L., 1994, AJ 108, 1872

Knude, J. & Høg, E., 1998, A&A 338, 897

Koresko, C., 1995, ApJ 440, 764

Kobayashi, N., Nagata, T., Hodapp, K.W., Hora, J.L., 1994, PASJ, 46, L183

Königl, A., 1991, ApJ 370, L39

Königl, A. & Pudritz, 1999, "Protostars & Planets IV" eds. V. Mannings, A.P. Boss & S.S. Russell, Univ. of Arizona Press

Kurucz, R., 1991, in Stellar Atmospheres: Beyond the Classical Models, eds. L. Crivellari, I. Hubeny & D.G. Hummer (NATO ASI Ser; Dordrecht: Kluwer), 441

Kurucz, R., 1992, in The Stellar Populations of Galaxies, eds. B. Barbury & A. Renzini (IAU Symp 149, Dordrecht:Kluwer), 225

Lada, C.J., 1988, 'Formation and evolution of low mass stars', ASI conference series, eds. Dupree A. & Lago M., Kluwer Academic

Lada, C.J. & Adams F.C. 1992, ApJ 393, 273

Lada, C.J. & Wilking, B.A., 1984, ApJ 287, 610

Laplace P., 1796, Exposition du systeme du monde (Exposition of the system of the world)

Lightfoot, J.F. 1989, MNRAS 239, 665

Livingston, W. & Wallace L, 1991, "An atlas of solar spectrum in the infrared from 1850 to 9000 cm^{-1} (1.1 to 5.4 μm)", NSO Technical Report #91-001.

Lynden-Bell, D. & Pringle, J., 1974, MNRAS 168, 603

Luhman, K. & Rieke, G., 1998, ApJ, 497, 354

Martín, E.L., 1998, AJ 115, 351

Mekkaden, M.V., 1999, A&A 344, 111

Meyer, M., Calvet, N. & Hillenbrand, L., 1997, AJ 114, 1

Moore, T.J.T. & Emerson J.P., 1994, MNRAS 271, 243

Mouschovias, T.C, 1991, ApJ 373, 169

Muzerolle, J., Calvet, N. & Hartmann, L., 1998, ApJ 492, 743

Najita, J., Edwards, S., Basri, G. & Carr, J.,2000, in Protostars and Planets IV, ed. V. Mannings, A. P. Boss & S. S. Russell (Tucson: University of Arizona Press), in press

O'Neal, D., Neff, J. & Saar, S., 1998, ApJ 507, 919

Ostriker, E. & Shu, F., 1995, ApJ 447, 813

Padgett, D., 1996, ApJ 471, 847

Parker, Q. & Watson, F., 1995, FLAIR System User Guide, AAO UM:31.1

Pettersen, B., Hawley, S. & Fisher, G., 1992, Solar Physics 142, 197

Piorno Schiavon, R., Batalha, C. & Barbury, 1995, A&A 301,840

Pringle, J.E., 1981, ARA&A, 19 137

Reipurth, B., Bally, J. & Devine, D., 1997, AJ 114, 2708

Rice, J. & Strassmeier, K., 1996, A&A 316, 164

Radick, R., Lockwood, G. & Baliunas, S., 1990, Science 247, 39

Rogers, F. & Iglesias, C., 1992, ApJS, 79, 507

Safier, P., 1998, ApJ 494, 336

Scalo, J., 1986, Fundamentals of Cosmic Physics 11, 1

Siess, L., Forestini, M. & Bertout, C., 1999, A&A, 342, 480

Simon, M. et al. 1995, ApJ 443, 625

Shevchenko, V. & Herbst, W., 1998, AJ 116, 1419

Shu, F. at al., 1994, ApJ 429, 781

Shu, F. et al., 1995, ApJL 455, L155

Smith, K. et al., 1999, MNRAS 304, 367

Solanki, S. & Unruh, Y., 1998, A&A 329, 747

Strassmeier, K. & Rice, J., 1998, A&A 339, 497

Strom, K. et al., 1990, ApJ 362, 168

Strom, K., Kepner, J. & Strom, S., 1995, ApJ 438, 813

Terranegra, L. et al, 1999, A&A 341, L79

Thatcher, J. & Robinson, R., 1993, MNRAS 262, 1

Topka, K., Tarbell, T. & Title, A., 1997, ApJ 484, 479

Unruh, Y., Solanki, S. & Fligge, M., 1999, A&A 345, 313

Valenti, J., Basri, G. & Johns, C., 1993, AJ 106, 2024

Vrba, F., Coyne, G. & Tapia, S., 1993, AJ 105, 3

Voshchinnikov, N.V. & Grinin, V.P., 1991, Afz 34, 181

Wallace, L. & Livingston, W., 1992, "An atlas of a dark sunspot umbral spectrum from 1970 to 8640 cm^{-1} (1.16 to 5.1 μm)", NSO Technical Report #92-001.

Walter, F.M., Brown, A., Mathieu, R.D., Myers, P.C. & Vrba, F.J., 1988, A.J. 96, 297

Xu, Z, 1991, A&A 248, 367